1-1-2011

Fatigue Testing and Computational Analysis of a Spinal Implant

Timothy Helton
University of Denver

Fatigue Testing and Computational Analysis of a Spinal Implant

Abstract

The following study investigates the fatigue behavior of a spinal implant developed by Synthes, Inc. to provide stability and off load pressure from the discs in the lumbar region. The installation process for the StenoFix design utilizes plastic deformations to customize the device to each individual patient, but also has potential to degrade fatigue behavior. Physical testing of two titanium alloys, Ti-6Al-7Nb and Ti-15Mo, was conducted on hydraulic test frames and compared to computational simulations which were carried out for the following scenarios: cyclic excitation following plastic deformation; variation of material property definition; variation of loading location; and three modifications to initial geometry. From the physical testing it was found that Ti-6Al-7Nb had superior fatigue performance when compared to Ti-15Mo, and both materials showed characteristics of cyclic hardening. Computational results display improved predicted fatigue performance when the implant inner and outer wing surface was modified so the derivative of curvature was continuous. The Morrow Strain-Life model was used to predict design life using parameters found in literature and determined by the simulations. The model shows promising results and suggests longer design lives would occur by altering the direction of plastic deformation during installation.

Document Type

Thesis

Degree Name

M.S.

Department

Mechanical Engineering

First Advisor

Peter Laz, Ph.D.

Second Advisor

Paul Rullkoetter

Third Advisor

Ramakrishna Thurimella

Keywords

Cyclic hardening, Fatigue, Spinal implant, Titanium

Subject Categories

Engineering | Mechanical Engineering

FATIGUE TESTING AND COMPUTATIONAL ANALYSIS OF A SPINAL IMPLANT

_____

A Thesis

Presented to

the Faculty of Engineering and Computer Science

University of Denver

_____

In Partial Fulfillment

of the Requirements for the Degree

Master of Science in Mechanical Engineering

_____

by

Timothy J. Helton

March 2011

Advisor: Dr. Peter Laz

Author: Timothy J. Helton
Title: FATIGUE TESTING AND STRESS PREDICTION OF THE STENOFIX SPINAL IMPLANT
Advisor: Dr. Peter Laz
Degree Date: March 2011

Abstract

The following study investigates the fatigue behavior of a spinal implant developed by Synthes, Inc. to provide stability and off load pressure from the discs in the lumbar region. The installation process for the StenoFix design utilizes plastic deformations to customize the device to each individual patient, but also has potential to degrade fatigue behavior. Physical testing of two titanium alloys, Ti-6Al-7Nb and Ti-15Mo, was conducted on hydraulic test frames and compared to computational simulations which were carried out for the following scenarios: cyclic excitation following plastic deformation; variation of material property definition; variation of loading location; and three modifications to initial geometry. From the physical testing it was found that Ti-6Al-7Nb had superior fatigue performance when compared to Ti-15Mo, and both materials showed characteristics of cyclic hardening. Computational results display improved predicted fatigue performance when the implant inner and outer wing surface was modified so the derivative of curvature was continuous. The Morrow Strain-Life model was used to predict design life using parameters found in literature and determined by the simulations. The model shows promising results and suggests longer design lives would occur by altering the direction of plastic deformation during installation.

Keywords: Fatigue, Spinal Implant, Titanium, Cyclic Hardening

Acknowledgements

A number of events fell into place for this study to be completed and I would like to recognize some of the people and companies that helped make it possible.

Dr. Armentrout brought mechanical testing contracts from Skydex Technologies, Inc. to the University, which helped support this project. Dr. Peter Laz was willing to take on yet another graduate student when it would have been easy to say no. Jon Buckley taught me to use the machine shop tools, and did not become enraged after I broke a few. Dana Coombs of Synthes, Inc. freely supplied test fixtures, specimens, and documentation. Brian Burks played the role of mock advisor so well that I have no doubt he will be an outstanding professor someday. My wife Meredith was willing to let me return to school and take a chance at finding a career.

Thank you for the support that each of you sent my way over the last couple of years.

Table of Contents

List of Figures

List of Tables

Nomenclature

ds	Change in arc length
$d\phi$	Change in tangential angle
b	Fatigue strength exponent
c	Fatigue ductility exponent
E	Modulus of elasticity
e	Engineering strain
F	Applied force to a beam
f	Load
I	Moment of inertia
K	Strength coefficient
K_{arc}	Curvature
k	Stiffness
l	Final length of specimen
l_o	Initial length of specimen
M	Beam moment
M_1	Reaction moment for a beam
n	strain hardening exponent
q	Beam loading
R	Reaction force
s	Engineering stress
V	Beam shear
x	Distance along beam
y	Beam deflection
$\Delta\varepsilon$	Delta strain
$\Delta\varepsilon_e$	Delta elastic strain
$\Delta\varepsilon_p$	Delta plastic strain
δ	Deflection
ε	True strain
ε_e	Elastic strain
ε_f‘	Fatigue ductility coefficient
ε_p	Plastic strain
θ	Beam slope angle
σ	True stress
σ_f’	Fatigue strength coefficient
σ_m	Mean Stress

CHAPTER 1. INTRODUCTION

1.1. Motivation

Disc degeneration in humans can begin as early as age thirty due to a number of factors. Some of the known catalysts contributing to disc damage include aging, obesity, smoking, vibration due to transportation, and lifting of excessive loads (Zhang, et al. 2009). It has been shown that 70-85% of all people will suffer from back pain at some point over their lives. In the United States back pain is the second most common reason for medical appointments, the fifth highest cause for admission to a hospital, and the third most common aliment that results in surgical procedures. Other western countries have shown a similar statistics with respect to lower back pain (Andersson 1999).

One potential treatment that has shown promise in alleviating the symptoms of lower back pain is disc decompression (Apfel, et al. 2010). By reducing compressive loads from the spine each disc is allowed to lengthen and initial studies show signs of disc regeneration (Macario, et al. 2008). Therefore if devices can be developed that reduce the compression of spinal discs, the quality of life for multitudes of people will be increased.

1.2. StenoFix Concept of Design

The StenoFix implant developed by Synthes, Inc. has been designed to be plastically deformed onto two vertebrae in the lumber region with the purpose of providing an alternate load path for stress that would otherwise be directed through the

disc region. The device is comprised of a rectangular cross section that follows a sinusoidal path with four wings, two on either end, which are used to secure the implant to the spine as shown in Figure 1. 1 and Figure 1. 2. In addition to redirecting loads away from the disc, the sinusoidal section will provide stabilizing reactionary forces characteristic of spring like behavior. In theory, two devices could be used in series for patients that experience pain in adjacent discs.

Figure 1. 1 StenoFix spinal implant developed by Synthes, Inc.

Figure 1. 2 StenoFix implant mounted between spinous processes in the lumber region

1.3. Research Objectives and Organization

One major issue of concern facing the StenoFix design is the intentions to have this device exceed the elastic region of the material during installation. The benefits of this method of installation include reduced complexity during surgery, fewer foreign bodies placed in patients, and a smaller surface area of hardware in contact with the spine. These attributes will raise the probability of receiving a successful surgery by reducing the frequency of resorption, a condition where the bone deteriorates at the interfacial boundary resulting in implant loosening (Geetha, et al. 2009). The implant surface has also been anodized for improved fatigue life (Leinenbach and Eifler 2006). It has been shown that initial overloads in the proper orientation will extend fatigue life by imparting residual compressive stress (Mahmoud 2007). In the case of this design the initial presetting of the material will result in residual tensile stresses, which has a

negative effect on fatigue attributes. To realize the benefits of this implant, the fatigue properties must be understood to insure product longevity and the corresponding safety to patients after installation.

This body of work examined the fatigue behavior of the wing portion of the implant with the main objective of developing a model to predict design life. Physical testing was conducted to provide a means to verify the predictive model and identify the cause of nucleation. Computational simulations were used to estimate the parameters of mean stress and strain amplitude, which were utilized in the predictive model.

The physical test specimens were manufactured by Synthes, Inc. to have four individual wings per specimen as shown in Figure 1. 3. The specimens possess the attributes of the actual StenoFix implant wings, but have a solid center section in lieu of the spring like structure to allow ease of mounting to the test fixtures.

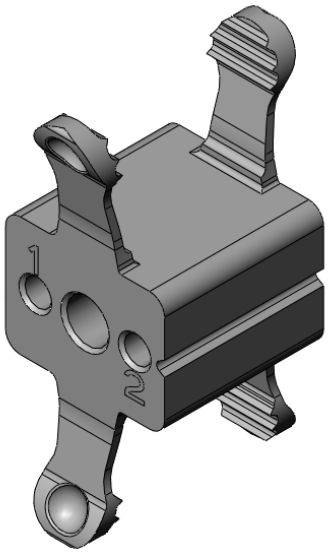

Figure 1. 3 StenoFix fatigue test specimen with four individual wings

This document has been organized in the following manner. The remainder of this chapter will describe general background concepts and mechanisms of fatigue failures. Chapter 2 will document the methods used during the physical testing followed by the computational methods. The results of the actions outlined in Chapter 2 will be presented in Chapter 3 with the physical testing results preceding the computational results. Chapter 4 will discuss points of interest observed by the study along with improvements that could be made and proposed future work. The conclusions from this study are recapped in Chapter 5. Appendix A contains the detail part drawings for the test fixtures that were fabricated. Appendix B lists the log of tests completed by Synthes, Inc., while Appendix C lists the log of tests completed by the University of Denver. Appendix D provides tables of calculated material stiffness values for all tests conducted by the University of Denver. The final entry in the document is Appendix E, which provides tables and figures documenting the stress and strain results for all of the computational simulations evaluated during this study.

1.4. General Fatigue Background

Fatigue failure of metals is due to repeated application and removal of stress, which became common place during the Industrial Revolution, in which rotating machinery was invented. The first known publication pertaining to fatigue of metal was written by 1837 (Albert 1837), where W. A. J. Albert described the testing of chains used in mining applications. In the decades that followed August Wohler investigated the failures of railway car axels, and developed the initial test fixtures dedicated to characterizing fatigue behavior (Schutz 1996). Wohler introduced the Stress–Life and endurance limit concepts, which are still used in practice today. The Stress–Life

approach predicts the number of cycles a specimen will withstand before failure at a given alternating stress. This method has been shown reliable for high cycle fatigue, which is valid for total life spans in excess of 10,000 cycles. For a few materials, there is a given stress amplitude that is low enough that a fatigue failure will never occur. This stress amplitude is known as the endurance limit of the material (Stephens, et al. 2001).

Slightly over 100 years after Wohler began his investigations, S. S. Manson and L. F. Coffin Jr. laid the foundation for the Strain-Life approach. This approach is more suited to systems that will experience a small number of extreme load cycles, which is known as low cycle fatigue. Their research was driven by the failure of high pressure vessels (Schijve 2003). Low cycle fatigue assumes plastic deformation occurs upon each cycle, while high cycle fatigue does not. The plastic deformation may occur macroscopically as show with the StenoFix design or more commonly only occur in a localized area. Evaluating a system using low cycle fatigue techniques requires increased effort when compared to applying the high cycle fatigue method due to the complication of accurately measuring strain. If the low cycle fatigue methods are used to evaluate a high cycle fatigue problem the results will be equivalent (Bannantine, Comer and Handrock 1990).

A design's fatigue behavior is influenced by the type of material, the manufacturing process, geometry, and applied loading. The first three of these factors are able to be varied during the design process, while the fourth is governed by the application. Even though the loading of a component cannot be dictated, understanding in this area will allow concessions to be made preventing premature failure (Sonsino 1990).

1.5. Fatigue Mechanisms

Modern day aircraft are prime examples of machines that experience both high and low cycle fatigue. During takeoff and landings the airframe is subjected to massive loads in the low cycle realm, while in flight multitudes of weaker amplitude loads due to turbulence occur in the high cycle regime. The spinal implant under investigation behaves similar to an aircraft in the fact that during installation, and sporadically throughout the device life, high loads will occur in the low cycle region, while everyday body movements occur in the high cycle region. Independent of the model used to analyze the fatigue failure for metals the mechanisms are always the same, crack nucleation and crack growth.

Once a crack forms in metallic structures the cyclic application of stress in tension will perpetuate the crack growth. The qualifier that the stress must be in tension is crucial due to the fact that compressive forces act to close cracks, thus tending to preventing fatigue failures and the propagation of fatigue cracks. Cracks found in metals typically are initiated at a notch or stress concentration, which is referred to as the nucleation site. These nucleation sites are highly dependent on the inherent microstructure of the material and are commonly found on the atomic level at part surface boundaries where initial damage caused by the manufacturing process or in-service use are compounded by the effects of corrosion.

Careful observation of a fractured surface, known as fractography, will yield details related to the fatigue failure. A nucleation site, or sites, can be determined by following the river patterns back to their origin. Surrounding the nucleation site will be a

fatigue region, characterized by a smooth surface with darker and lighter bands referred to as beachmarks or clam shell marks. These bands catalog the cyclic growth of the crack. For some materials, smaller contour lines known as striation formations may be seen inside the beachmark zone at high magnification, which represent the crack progression from individual cycles. At the boundary of the smooth fatigue region there will be a distinct ridge know as the shear lip. This ridge is the point at which the material reached a critical crack size resulting in a rough surface due to fast fracture (Norton 2006). The location of this lip within the failed surface is determined by a material property that defines the ability to resist the stress generated at a crack tip known as fracture toughness. The effect a crack tip has on the local stress can be calculated by the stress intensity factor, which is determined by the global stress, crack size, and the geometry of the failed surface. A crack will propagate due to fatigue until the stress intensity factor is equal to the fracture toughness and then fast fracture will occur. Figure 1. 4 displays a fractured surface from one of the spinal implants with the separate fatigue regions labeled and the shear lip designated by a dashed line.

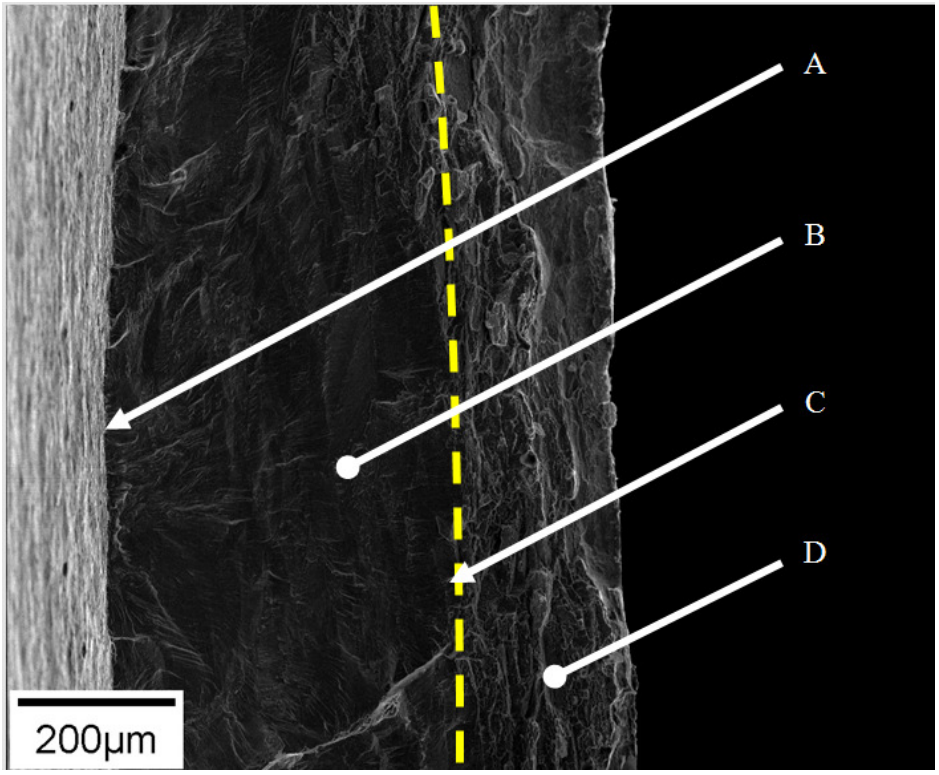

Figure 1. 4 Scanning Electron Microscope image of fractured spinal implant
A) nucleation site; B) beachmark region; C) shear lip (dashed line); D) fast fracture region

The application of repeated loading can affect the relationship between stress and strain for a given material. Once a cyclic load has been applied to a specimen it is possible for the monotonic properties to be increased or decreased depending on how the cyclic loading causes the atomic structure to be rearranged. If the rearrangement of grains results in a microstructure that is more capable of reducing dislocation movement and less prone to slip the material is said to cyclic harden. In this case the material properties of the cyclic specimen would be higher than the monotonic specimen. The opposite of this scenario would result in the rearrangement of grains allowing dislocations to bypass grain boundaries and slip would be increased. When this phenomenon occurs the material has cyclic softened. It is possible for materials to initially cyclic harden and then soften or cyclic soften and then harden if the repeated

loading is to continue. Most published material properties have been determined for a monotonic loading case and physical testing must be completed to determine the cyclic material properties.

CHAPTER 2. METHODS

2.1. Test Method Overview

Two types of physical tests were conducted during this study. The first procedure plastically deformed the samples from the as received condition to simulate installation of the device, while the second cyclically loaded the samples to model the effects of every day motion for a human spine. Figure 2. 1 is a photograph of a sample in the as received condition, while Figure 2. 2 displays the sample after the plastic deformation test has been completed on all four wings.

Figure 2. 1 StenoFix fatigue specimen as received condition

Figure 2. 2 StenoFix fatigue Specimen with all four wings plastically deformed

2.2. Physical Testing

While the end goal of this study is to develop a predictive model that is capable of determining the design life of the StenoFix wings physical testing must still be conducted. Any computational model that has no validation in experimental testing cannot be applied. Physical testing also allows the opportunity to witness the driving mechanics behind the implant, which should lead to a more accurate representation of these traits in the computational model.

2.2.1. Initial Inspection

Prior to plastic deformation on select samples, all wings were examined under magnification by an Olympus BX51M optical microscope equipped with a carriage of lenses ranging from 5X-100X, in addition to a 10X digital zoom to document potential nucleations sites.

2.2.2. Test Setup

The mechanical testing was performed on the MTS 858 Table Top test frame shown in Figure 2. 3. This machine is a hydraulic test frame which was routed to an MTS 521.14 high pressure unit. In this configuration, the actuator is located on the top of the figure on the post protruding from the crosshead. Careful inspection of the figure will show that two load cells are attached to the base of the frame, but only one was used to acquire data. The frame has a 25,000 Newton load cell mounted to the base, which was not used due to concerns of insufficient resolution. Instead, a 100 Newton load cell with a tolerance of 0.1 Newtons was mounted onto the existing load cell for convenience. It would have been possible to mount the 100 Newton load cell to the actuator, but this was

not done in order to reduce the noise transmitted by the hydraulic lines originating from the high pressure unit. Actuator displacement data was recorded by a MTS model 359 linear variable differential transformer (LVDT) calibrated to a maximum error of 0.37 percent.

Figure 2. 3 MTS 858 table top hydraulic test frame

Initial setup to run a fatigue test is as follows. First, the center t-slot fixture was fastened to the actuator arm by using 1/2-20 threaded rod. The 100 Newton load cell was joined to the 25,000 Newton load cell using a 1/2-20 to 1/8-28 adaptor. A section of 1/8-28 threaded rod was used to mate the anvil to the 100 Newton load cell. Next, two t-slot bolts were inserted into the center t-slot fixture. The stenofix test mount was fastened to the center t-slot fixture, but only secured hand tight. Then a specimen was inserted onto

guide pins located on the stenofix test mount and fastened down using two 4mm washers in conjunction with the 4mm socket head cap screw. With all the hardware installed on the frame, the stenofix test mount was translated along the center track of the t-slot fixture until the second serration notch was aligned with the apex of the anvil. At this point, the assembly was ready for fatigue testing to begin. Once testing was complete, a set of calipers were used to measure the offset distance from the base of specimen block to the apex of the anvil to determine the actual moment arm.

ITEM NO.	PART NUMBER	QTY.
1	CENTER T-SLOT FIXTURE	1
2	T-SLOT BOLT	2
3	STENOFIX TEST MOUNT	1
4	3/8 FLAT WASHER	2
5	3/8-16 HEX NUT	2
6	STENOFIX TEST SAMPLE	1
7	4MM FLAT WASHER	2
8	M4 X 0.7 X 25MM SOCKET HEAD SCREW	1
9	ANVIL	1
10	1/8 THREADED ROD	1
11	100N LOAD CELL	1
12	1/2-20 THREADED ROD	1
13	1/2-20 TO 1/8-28 ADAPTOR	1

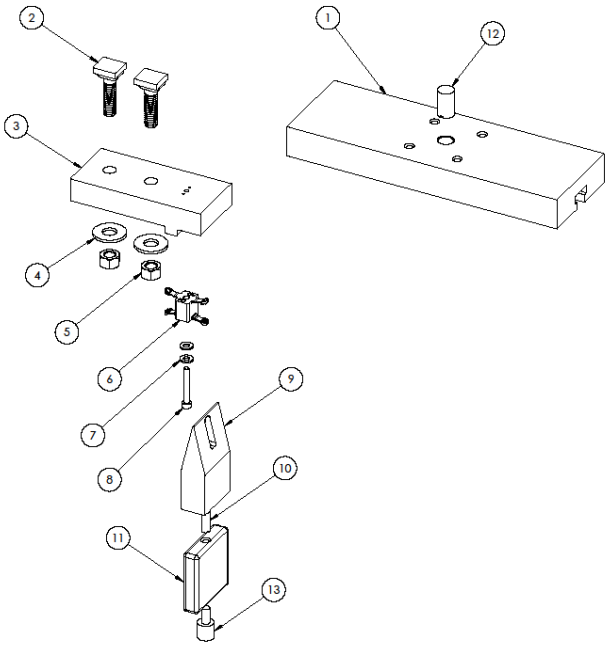

Figure 2. 4 StenoFix test fixture bill of materials

The procedure to load a specimen into the fixtures for the plastic deformation test is similar to the fatigue step up with one exception. Since the non-serrated surface of the wing was in contact with the anvil, a calibration block assembly shown in Figure 2. 5 was created to locate the stenofix test mount. This block hard locates the anvil to have a

moment arm equal to 10.4mm and utilizes the same mounting pins and 4mm socket head cap screw. Once the stenofix test mount was secured to the center t-slot fixture, the gauge block was removed and the test specimen was installed as described above. Using a gauge block assembly in the fatigue testing was unacceptable since there was variation in the spring back location after plastic deformation. This resulted in instances where the anvil was located at the proper 10.4mm but centered upon a serration tooth. Appendix A contains detail drawings of the unique test fixtures that were required for this testing.

ITEM NO.	PART NUMBER	QTY.
1	PLASTIC DEFORMATION BLOCK BASE	1
2	PLASTIC DEFORMATION BLOCK TOP	1
3	1/4 CAPTIVE SCREW	2

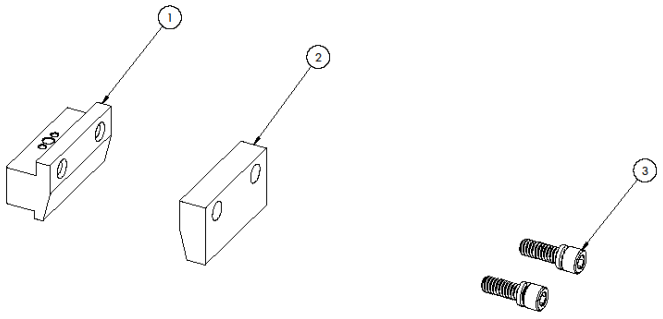

Figure 2. 5 Plastic deformation calibration block bill of materials

2.2.3. Plastic Deformation Test Procedure

Once a sample was loaded into the test frame as described in section 2.2.2, the following plastic deformation test sequence was conducted. The actuator was lowered until the test specimen just made contact with the anvil but did not exert any force on the specimen. This location was designated as the test starting point and the displacement sensor was offset to read zero. Next, the command was given to the actuator to descend

at a rate of one millimeter per second for a total distance of 5.95 mm. Once this destination had been reached, the actuator was left to dwell at this location for two seconds. The test was concluded by raising the actuator at a rate of one millimeter per second until zero force was recorded by the load cell and this final position was logged.

While the test was being conducted, data was acquired for the variables of force, displacement, and time. The sampling rate was chosen to be 512 Hertz to allow the calculation of a discrete Fourier transform to be calculated during the data processing phase if filtering was required. The output signal from the 100 Newton load cell did not generate large amounts of noise, so the filtering process was not required. Figure 2. 6 and Figure 2. 7 display the specimen orientation for the plastic deformation test.

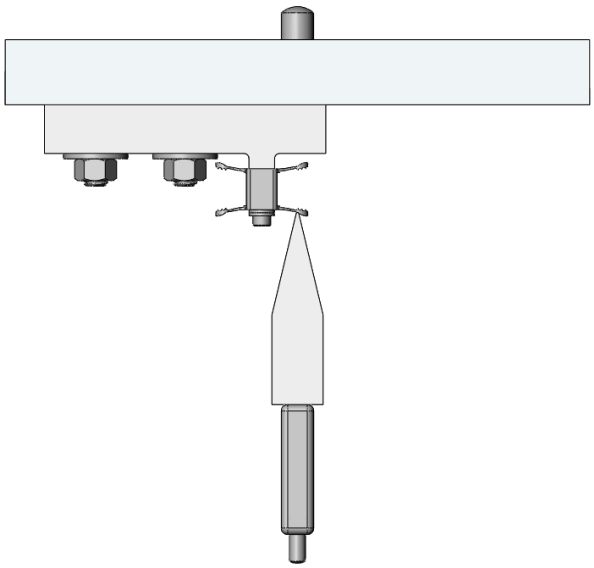

Figure 2. 6 Plastic deformation test setup front view

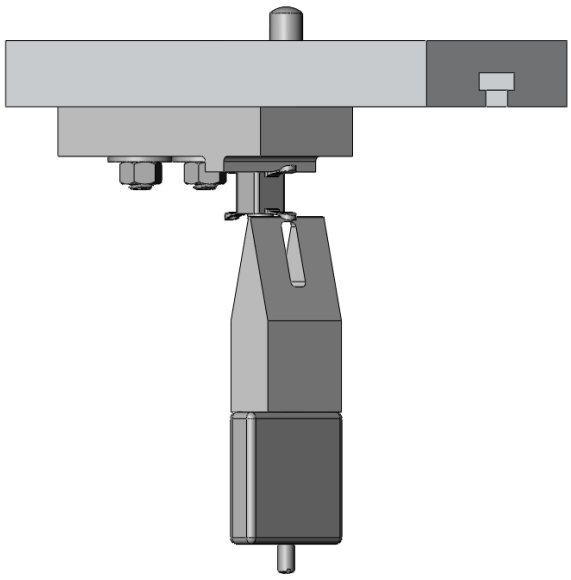

Figure 2. 7 Plastic Deformation test setup view rotated 45° clockwise

2.2.4. Fatigue Test Procedure

After the plastic deformation test had been completed, a sample was loaded into the test frame as described in section 2.2.2. During each fatigue test only one wing per sample experienced cyclic loading. The hole removed from the anvil allowed the adjacent wing on the same sample to not come in contact with any test apparatus. Figure 2. 8 and Figure 2. 9 display the specimen orientation for the fatigue test.

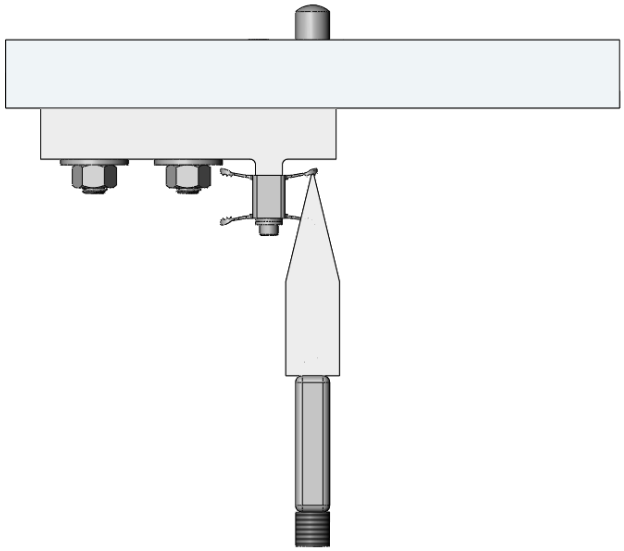

Figure 2. 8 Fatigue test setup front view

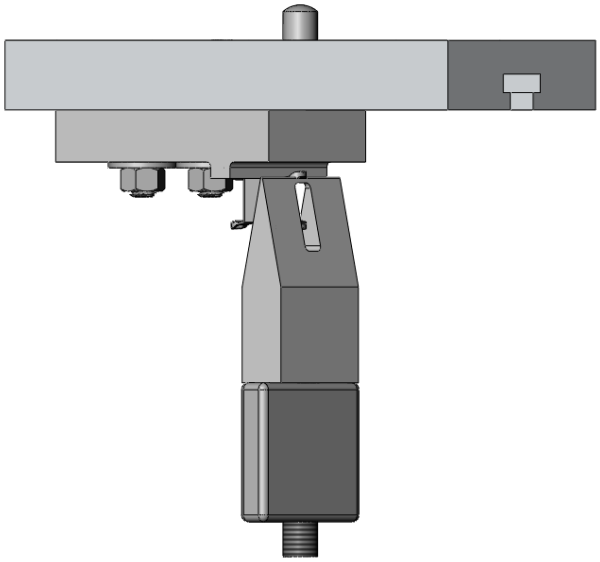

Figure 2. 9 Fatigue test setup view rotated 45° clockwise

Loading amplitude of 10:1, an R ratio of 0.1, was chosen to cyclically excite the specimen at a rate of five Hertz during a maximum of five-million cycles for each fatigue test run by the University of Denver. The number of cycles was chosen to comply with ASTM F 1717, which issues guidelines for testing of vertebrae constructs (ASTM F 1717

2004) . The peak loads were chosen to be between 35 and 55 Newtons at 5 Newton intervals. For example, a test run with a maximum load of 50 Newtons would have a minimum load of 5 Newtons. If a specimen was tested and achieved run out then the maximum load would be increased by 5 Newtons and tested again.

Data was written for force, displacement, and time for the following cycles throughout the test in one file: 1, 10, 100, 1000, 2000, 3000, 4000, 5000, 6000, 7000, 8000, 9000, 10000, 20000, 30000, 40000, 50000, 60000, 70000, 80000, 90000, 100000, 150000, 200000, 250000, 500000, 750000, 1000000, 1250000, 1500000, 1750000, 2000000, 2250000, 2500000, 2750000, 3000000, 3250000, 3500000, 3750000, 4000000, 4250000, 4500000, 4750000, 5000000. In a separate data file, the minimum and maximum displacement values for the prescribed cycles were recorded. For the same reasons stated in the plastic deformation procedure, a sampling rate of 512 hertz was again used during the fatigue tests. Failure detectors were installed in the controlling software to terminate the test if a distance of six millimeters was traversed by the actuator or the measured force exceeded eighty Newtons. If one of these detectors was triggered, the station pressure would remain constant, preventing the actuator from imparting increased force due to gravity to the load cell. In the event of a total failure of these protective measures, the load cell was capable of withstanding a one-thousand Newton load without adverse effects.

Two titanium alloys, Titanium-6 Aluminum-7 Niobium (Ti-6Al-7Nb), and Titanium-15 Molybdenum (Ti-15Mo), were under consideration to be used in this device, and conform to specifications developed by the American Society for Testing and

Materials ASTM F 1295 and ASTM F 2066 respectively. In the past, Titanium-6 Aluminum-4 Vanadium (Ti-6Al-4V) was the most widely used orthopedic implant material, but alternatives are now under consideration since Vanadium has been shown to be detrimental to the human body (Chen, et al. 2006).

Four wings of each test material were tested by Synthes, Inc.; using a slightly different test method designated MT10-105. The maximum load level for this procedure began all tests at 25 Newtons and a frequency of 5 hertz with run out defined as 500,000 cycles. The loading ratio of R=0.1 was consistent with the testing performed by the University of Denver. If run out occurred, the sample load was immediately increased by 5 Newtons and tested for another 500,000 cycles with the assumption that no prior damage had occurred. This process continued until failure.

2.2.5. Control Parameters

The MTS Flextest 60 controller was used in conjunction with the MTS 793.10 SE/IIs Multi-Purpose Testware software. Values for a closed loop control consisting of proportional (P) and integral (I) terms were combined with a minor input from an open loop control method of feed-forward (F) to provide acceptable means of driving the actuator at the correct load and frequency during the fatigue tests. This control method results in one term multiplying the calculated current error (P), one term multiplying the sum of the recent past error (I), and a final term (F) that supplies input for correcting the error seen between the set point value and the actual value (Dorf and Bishop 2008).

To determine the parameters to be used, the auto calibration feature of the Multi-Purpose Testware was utilized to gain a base point and then adjusted manually to tune the

system. The auto tuning feature is heavily reliant on an accurate initial input for the feedback values to reach a stable method of control. Due to this fact and the limited number of samples available, an aluminum plate was machined to approximately the same cross section as one of the implant wings and used with the intent of achieving quality initial input controller values. In the end this precaution concluded in failure and an actual test specimen was sacrificed to develop the controller parameters. Table 2. 1 displays the values found acceptable for the sacrificial aluminum plate and the titanium test samples.

Table 2. 1 MTS Flextest 60 control parameters for physical testing

Sample	Proportional (P)	Integral (I)	Derivative (D)	Feed Forward (F)
Aluminum	110	6.85	0.1551	0
Ti-6Al-7Nb	375	39	0	0.1
Ti-15Mo	375	39	0	0.1

2.2.6. Fractography

The study of failure surfaces is known as fractography and was undertaken to determine the root cause of a failed structure. Areas of interest that can be gained from this investigation include the initiation site location, mechanism of failure, and material composition. Surfaces of wings that were removed from the main specimen during fatigue testing were imaged using a JOEL 5800LV Scanning Electron Microscope (SEM). Care was taken to store the specimens so the fractured surfaces were not damaged prior to scanning, and images were obtained up to a magnification of 2,000 power.

While under vacuum in the SEM, multiple scans were conducted with an Oxford Pentafet X-ray detector for energy dispersive spectroscopy (EDS). This device is capable of converting the energy of incoming x-rays released from a specimen into voltage. The voltage is proportional to the energy of the x-rays and corresponds to known values of common elements, which in turn yields the chemical makeup of a specimen.

2.3. Computational Methods

The main objective of this study was to develop a model to predict the design life of the StenoFix spinal implant wings. In an ideal situation all elements concerning the final product life of the implant would be known prior to a single chip of metal being cut. While this is never achievable with the assistance of computational methods the quantity of prototype designs may be reduced and the overall performance has potential to be improved.

2.3.1. Beam Mechanics

Prior to adopting any numerical methods to determine loads and stresses imparted to the implant wing, the problem was analyzed using beam mechanics. The wing was simplified to a cantilever beam of constant cross section with a point load applied at the free end as shown in Figure 2. 10. By using singularity functions, the loading, shear, moment, slope, and deflection equations were calculated as function of length and are displayed below.

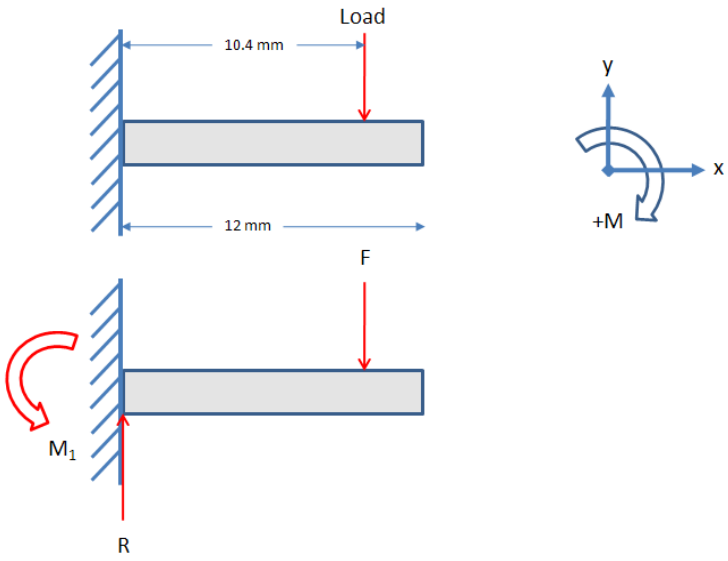

Figure 2. 10 Simplified beam mechanics free body diagram

$$q = -M_1 < x - 0 >^{-2} + R < x - 0 >^{-1} - F < x - 10.4 >^{-1} \quad (2.1)$$

$$V = -M_1 < x - 0 >^{-1} + R < x - 0 >^{0} - F < x - 10.4 >^{0} \quad (2.2)$$

$$M = -M_1 < x - 0 >^{0} + R < x - 0 >^{1} - F < x - 10.4 >^{1} \quad (2.3)$$

$$\theta = \frac{1}{E * I}\left(-M_1 < x - 0 >^{1} + \frac{R}{2} < x - 0 >^{2} - \frac{F}{2} < x - 10.4 >^{2}\right) \quad (2.4)$$

$$y = \frac{1}{E * I}\left(-\frac{M_1}{2} < x - 0 >^{2} + \frac{R}{6} < x - 0 >^{3} - \frac{F}{6} < x - 10.4 >^{3}\right) \quad (2.5)$$

2.3.2. Material Definition

Unfortunately, neither of the material specifications for Ti-6Al-7Nb or Ti-15Mo included information regarding the stress strain behavior of the respective materials. The properties for Ti-6Al-4V were available and were used to develop the elastic plastic true stress and true strain values (MMPDS 2003). Since the plastic portion of the stress strain curve is of importance in this design, the true values were used in the Abaqus material definition card to more accurately model the material. This was done by extracting

values from the engineering stress vs. engineering strain curve and then calculating the true stress vs. true strain. Equations (2.6) and (2.7) display the formulas for engineering stress and engineering strain respectively. Equations (2.8) and (2.9) display the formulas used to convert engineering stress strain values to true stress strain values (Ashby and Jones 2005). Table 2. 2 lists material properties for the titanium alloys under investigation with corresponding Ti-6Al-4V values for comparison.

$$s = \frac{P}{A_o} \tag{2.6}$$

$$e = \frac{l - l_o}{l_o} \tag{2.7}$$

$$\sigma = s\,(e + 1) \tag{2.8}$$

$$\varepsilon = ln(e + 1) \tag{2.9}$$

Table 2. 2 Material properties

Material	Modulus of Elasticity	Density	Ultimate Strength	Yield Strength	Elongation
	[GPa]	[1000 kg / mm3]	[MPa]	[MPa]	[%]
Ti-6Al-7Nb[a]	105	4.52E-09	900	800	10
Ti-15Mo[b]	78	4.96E-09	724	552	12
Ti-6Al-4V[c]	110	4.42E-09	896	813	10

Reference: a. (ASTM F 1295 2005) b. (ASTM F 2066 2007) c. (MMPDS 2003)

A simplified model to validate the material properties was created consisting of a single cylinder with a distributive pressure load equal to the maximum true stress stated in the elastic plastic definition applied to one surface, while the other surface was held fixed. This model was analyzed in Abaqus/Standard 6.9 (Simulia, Providence, RI) and comprised of reduced integration hexahedrons, C3D8R, Figure 2. 11 and Figure 2. 12 depict the geometry and loading conditions for the simulation.

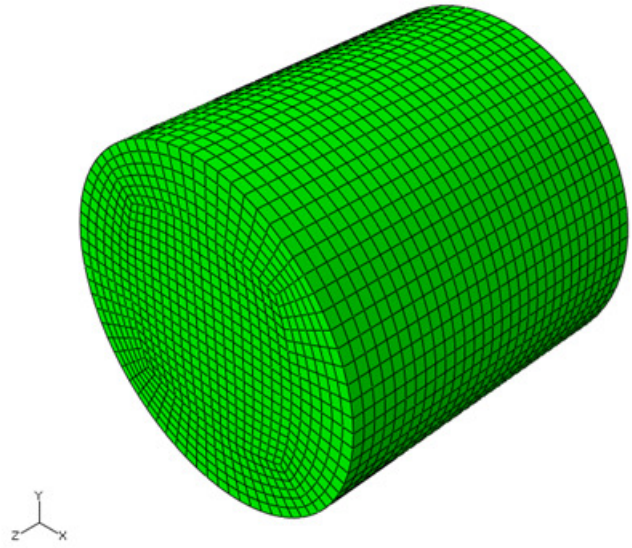

Figure 2. 11 Material validation simulation geometry

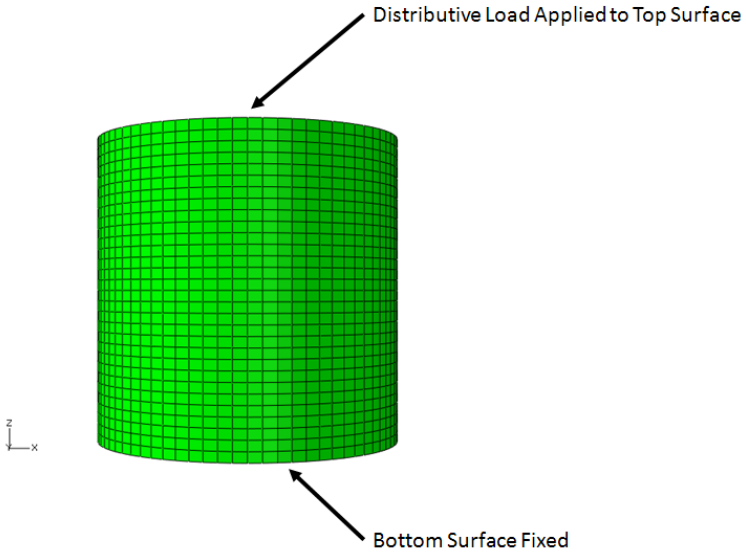

Figure 2. 12 Material validation simulation boundary conditions

2.3.3. Mesh Generation and Convergence

The process to mesh the implant wing began by segmenting the wing volume into multiple bodies in the Computer Aided Drafting (CAD) software package SolidWorks

and saving the geometry as an Initial Graphics Exchange Specification (IGES) file. It was then possible to import the IGES file into HyperMesh for mesh generation with each CAD body being assigned to individual layers for convenience. By dividing the implant volume in the CAD software prior to importing into HyperMesh, geometry manipulation was greatly improved. Once the initial file was loaded into HyperMesh, it was possible to return to the CAD software to alter the body division locations and then only export the relevant updated geometry. Once a satisfactory mesh was achieved, the nodes and elements were exported to an input text file for the Abaqus finite element software.

Initially, the volume was divided into tetrahedral elements with very little refinement resulting in a coarse mesh. This was done to reduce computational time during the debugging process of developing an Abaqus simulation. The mesh was refined progressively to have a higher density of elements to insure convergence of the model. The actual elements chosen were C3D10M due to the fact that these elements are more suited to large deformations and less susceptible to volumetric locking compared to the C3D10 elements (ABAQUS 2010). Volumetric locking is common in studies of metallic structures that undergo plastic deformation due to the incompressible nature of this motion. To account for the plasticity, additional restrictions are placed on each integration point to insure the volume at these locations shall remain constant. These restraints produce an over constrained element that has near infinite resistance to displacement and in essence behaves to stiff (Cook, et al. 2002). Figure 2. 13, Figure 2. 14, and Figure 2. 15 display the original tetrahedral mesh, intermediary mesh, and final refined mesh, respectively. After these simulations were completed the identical

geometries were analyzed with C3D10 elements for comparison. The results showed the field variables for the two element types to be within one percent and computational time was for the modified elements to be somewhat longer.

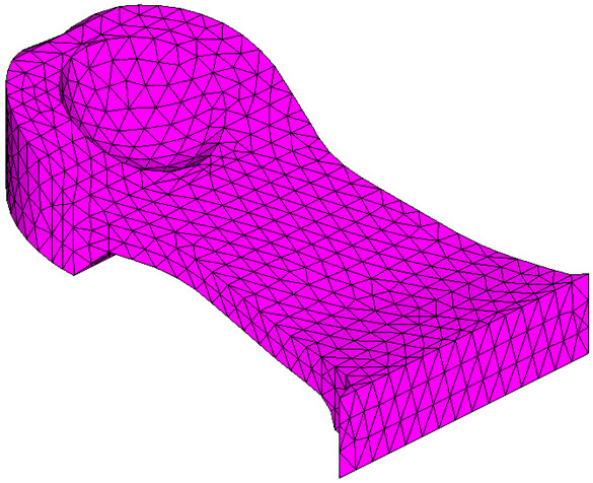

Figure 2. 13 Coarse tetrahedral mesh of StenoFix implant wing

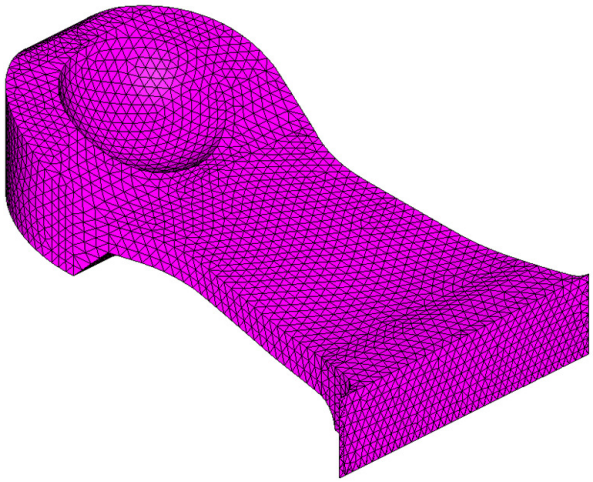

Figure 2. 14 Intermediary tetrahedral mesh of StenoFix implant wing

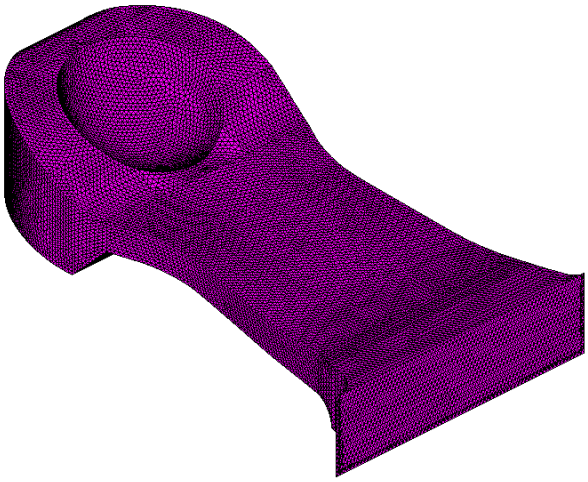

Figure 2. 15 Fine tetrahedral mesh of StenoFix implant wing

After producing simulations with the tetrahedral elements, a new series of meshes were generated using reduced integration hexahedral elements. These brick elements will provide equivalent results with less computational effort, have a better convergence rate, and are not as dependent on mesh orientation as tetrahedral elements (Taylor, et al. 1986). The final refinement of this improved mesh is shown in Figure 2. 16. These first order reduced integration elements, C3D8R, evaluate the element integration with a single Gauss point, and will converge to an equivalent result in less time when compared to the fully integrated versions (Bicanic and Hinton 1979). To confirm, this simulation was conducted with C3D8 fully integrated hexahedron elements, which required 68% longer computational times to arrive at a converged solution. In this case where no contact was present and the loading was mainly in bending the two element types arrived at similar values for all field variables in question.

One shortcoming of the reduced integration elements is the phenomenon of hourglassing. This event occurs when there is deformation at an element's boundary, but

there is zero strain at the integration point. To reduce the probability of invoking these zero strain modes, significant mesh refinement was employed in conjunction with distributing point loads over multiple nodes. The chosen element also possesses inherent stabilization parameters to reduce the effects of hourglassing (Liu, Hu and Belytschko 1994). Since the wing predominately experienced a bending motion, fully integrated elements would undergo shear and volumetric locking culminating in large underpredictions of displacement values. Shear locking has a similar end result as volume locking in that the elements behave too stiff, and is common in fully integrated elements dominated by a bending load. Fully integrated first order elements only allow the edges perpendicular to the bending axis to deform in a linear fashion, which drives strain energy to be converted into shear stress instead of correctly contributing to increased motion and is known as shear locking.

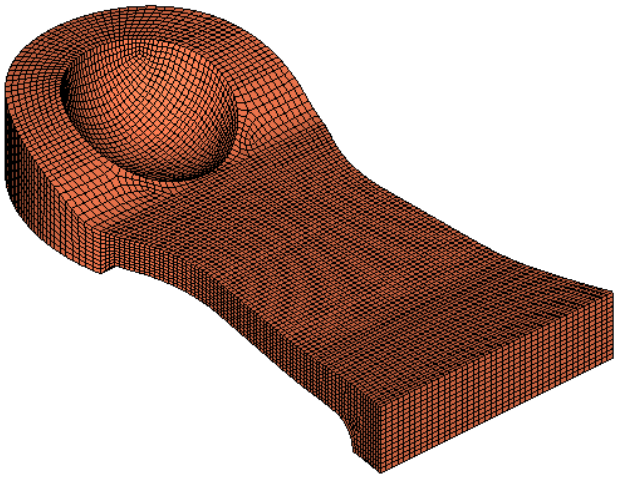

Figure 2. 16 Brick mesh of StenoFix implant wing

Additional hexahedral meshes were generated for each of the four simulations, which evaluated the effect of varying the load line. One model consisting of a single

cylinder was meshed in a similar manner to verify the material behavior and three proposed geometry modifications were also discretized in the same fashion.

2.3.4. Finite Element Analysis

The analysis and post processing for the implant were completed using the software package Abaqus/Standard version 6.9 (Simulia, Providence, RI). The simulation was designed to occur in three distinct steps, which included plastic deformation (Step 1), spring back (Step 2), and cyclic motion (Step 3). Node sets were created for the base of the wing, static loading points, and cyclic loading points as shown in Figure 2. 17 and Figure 2. 18. For all three steps, boundary conditions were imposed on the base node set constraining all degrees of freedom. The total displacement that took place over one simulation is shown in Figure 2. 19 and Figure 2. 20. Throughout the remainder of this document Step 1 will refer to the end point of the plastic deformation, Step 2 will reference the end point of the spring back motion, Step 3a will refer to the deformation that occurred at the cyclic maximum and Step 3b will correspond to the deformation location at the cyclic minimum.

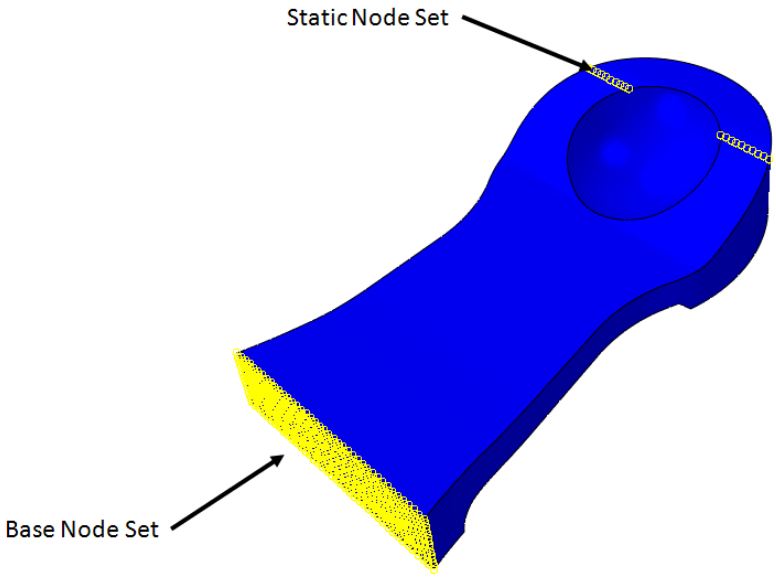

Figure 2. 17 Static and base node sets of StenoFix implant wing

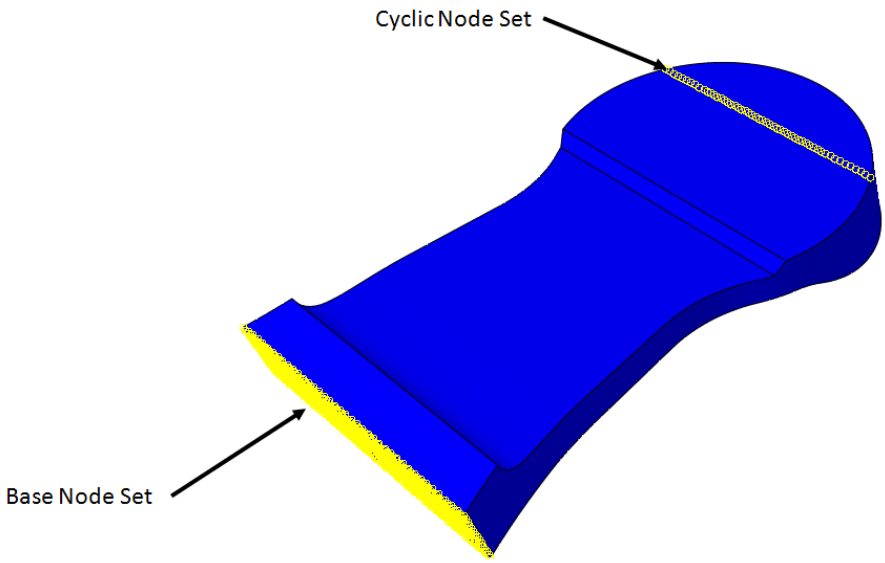

Figure 2. 18 Cyclic and base node sets of StenoFix implant wing

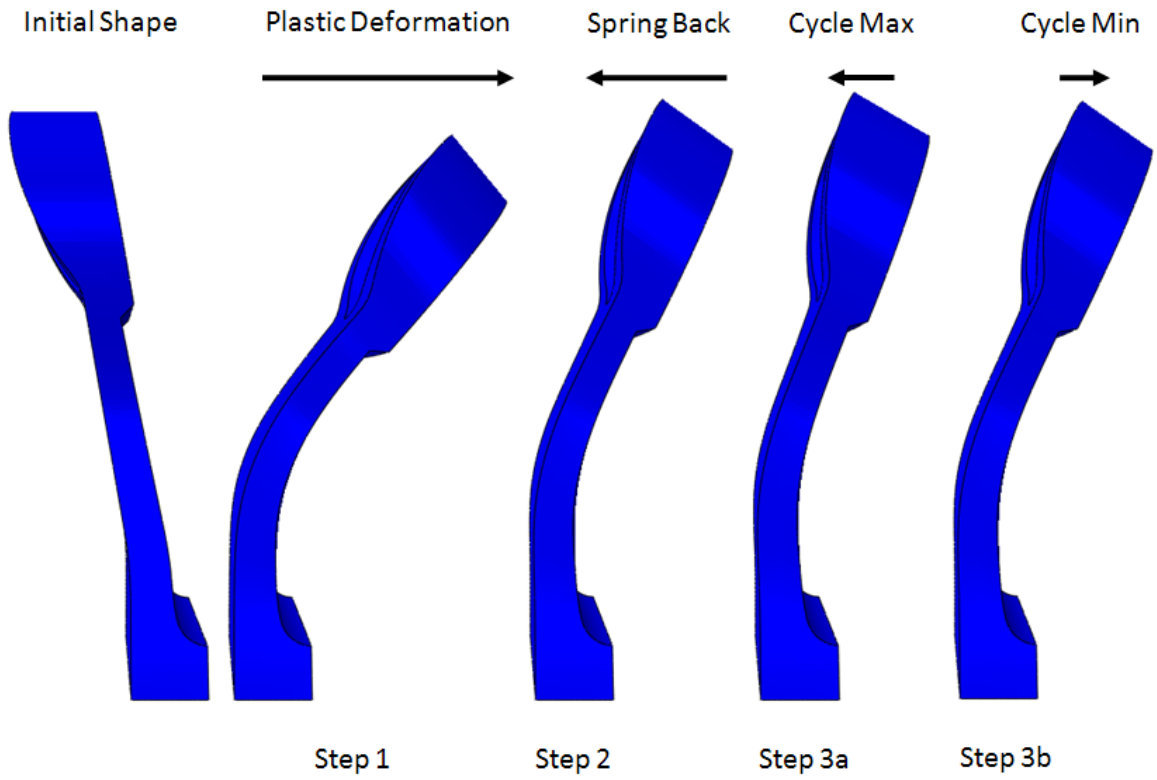

Figure 2. 19 Simulated motion of StenoFix implant wing
Arrows display the motion occurring during each step

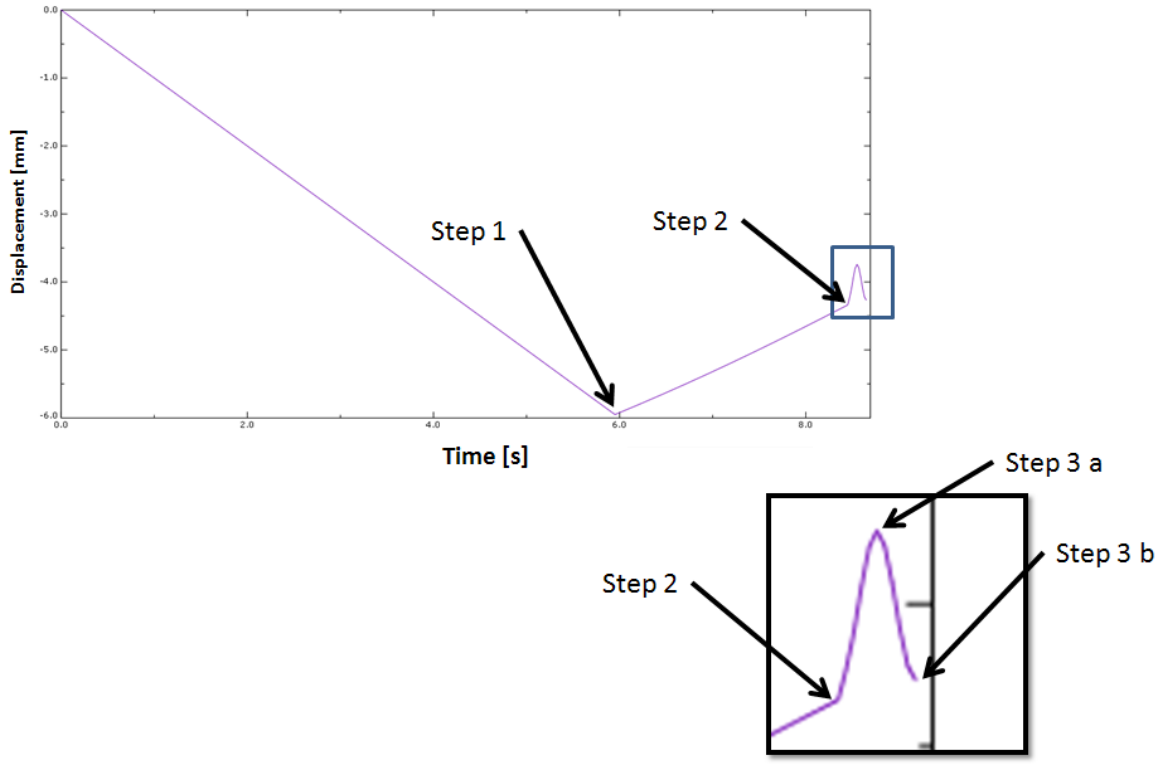

Figure 2. 20 Simulated motion of StenoFix implant with respect to time

During the plastic deformation step, the static node set was driven in displacement control to an offset location of -5.95 mm over a time of 5.95 seconds, matching the inputs given to the physical test specimens. The spring back step removed the displacement constraint applied in step one and allowed the reaction force to equilibrate over a time span of 2.5 seconds in a force control manner. The actual test specimens experienced slight variations in the time required to reach static equilibrium, so a standard time aligning with tests completed by Synthes, Inc was chosen. The final step of the simulation was again run in a force control manner by issuing a prescribed point load with a sinusoidal magnitude to all the nodes in the cyclic loading node set. This allowed the load to be distributed over multiple nodes and helped prevent hourglassing in the

mesh. The maximum amplitude of the sinusoidal load varied between 25 and 70 Newtons for the following simulation scenarios.

To determine the design's sensitivity to loading location the original wing's geometry's delivered by Synthes, Inc. was evaluated with the load line applied at a moment arm of 10.4 mm (nominal), 9.4 mm (-1 mm), 9.9 mm (-0.5 mm), 10.3 (-0.1 mm), and 10.5mm (+0.1 mm). The intent of these simulations was to understand what impact mislocating the loading location would have on the internal stresses and strains generated in the wing.

The standard geometry was evaluated using varying material properties and the load line held at a nominal 10.4mm. The yield strength and ultimate tensile strength were used to define the elastic plastic behavior of the material with three options comprised of nominal, nominal values plus 10 percent, and nominal values minus 10 percent. The intent of these simulations was to characterize the effect of material properties.

A series of simulations was conducted applying the cyclic loading of Step 3 to the original geometry without administering Steps 1 or 2. The intent of these models was to determine quantitatively the stress impact that occurred during plastic deformation.

Additionally, three geometric changes were made to the standard geometry in an attempt to reduce the predicted stress witnessed at a location common to physical specimen failure as shown in Figure 2. 21. Ten load cases ranging from 25-70 Newton maximum cyclic load were evaluated.

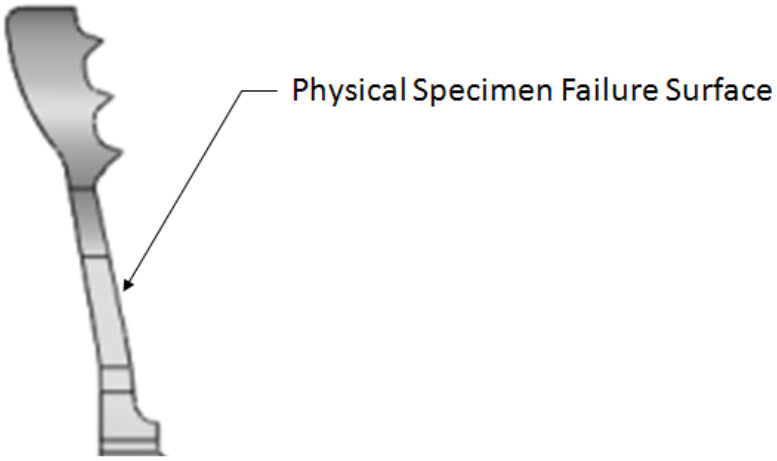

Figure 2. 21 Implant fatigue failure surface

The initial variation increased the overall thickness of the wing by altering the failure surface profile only. The rate of change of curvature with respect to arc length was not continuous on the original geometry or the initial variation. Curvature is defined as the tangential angle rate of change with respect to arc length as shown in equation (2.10).

$$K_{arc} \stackrel{\text{def}}{=} \frac{d\phi}{ds} \tag{2.10}$$

The discontinuity of the second derivative of the tangential angle with respect to arc length was identified as a potential stress concentration that led to the final two modifications in geometry. The second variant created a profile of the failure surface that provided a continuous derivative of curvature with respect to arc length. The third variant kept the modified failure surface from the second variant and also modified the loft of the surface opposing the failure surface with the same requirement of maintaining a constant derivative of curvature. Contour combs are used to graphically represent the

curvature magnitude along an arc. Figure 2. 22 depicts the three wing variants in comparison to the initial wing geometry.

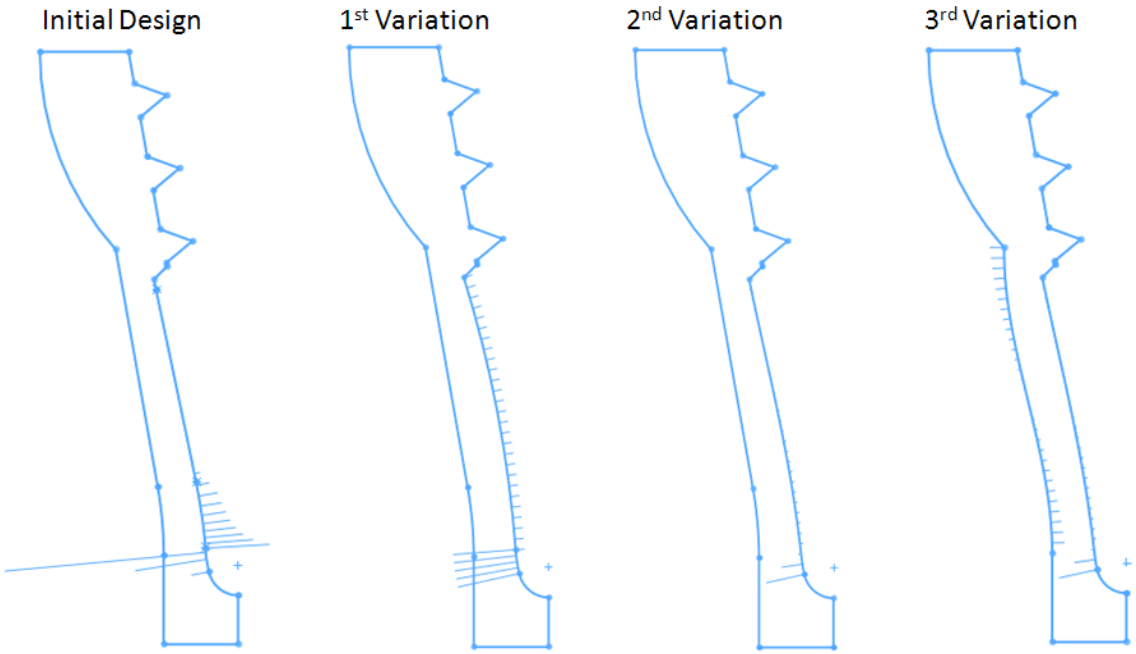

Figure 2. 22 Geometry variations for StenoFix implant with contour combs
Initial design as received from Synthes, Inc.; 1st Variation altered the failure surface to reduce curvature discontinuity; 2nd Variation altered the failure surface to eliminate the curvature discontinuity; 3rd Variation altered the failure surface and the opposing surface to eliminate the curvature discontinuity

The von Mises stress and logarithmic strain for an element located on the center line of the fatigue failure surface were used to compare the different variations of the wing loading parameters. The element was chosen to be 3.5mm from the cantilevered base since the actual test specimens were found to fail in this general location. It has been shown that extracting elemental field values from an integration point on initial geometry or post deformation geometry will reduce the amount of error observed when compared with measurements taken from nodal locations (Barlow 1977)(Barlow 1989). This effect is the result of multiple integration points being employed to interpolate the

field behavior, and then the average of the interpolations being used as the nodal value (Tenchev 1994). For these reasons, the field values for the element in question were obtained from the integration point. By modifying the geometry the failure point may have been altered, so for these simulations the volume of elements that exceeded the yield stress were also determined for the entire wing in addition to the portion of the wing in tension during the cyclic motion of Step 3.

One simulation was run completely in force control by prescribing a distributed point load to the static node set with a maximum value equal to the reaction force in the vertical direction from the displacement controlled simulation. Then in step two, this force was gradually removed and step three was run as stated above. The purpose of this simulation was to compare the results generated by the two methods of control.

CHAPTER 3. RESULTS

3.1. Physical Results

Per the methods described in Chapter 2, 24 wings were subjected to the plastic deformation test, and total of 22 fatigue tests were completed on 18 different wings. The discrepancy in fatigue tests compared to number of wings tested is explained by wings that experienced run out were tested multiple times.

3.1.1. Initial Inspection

Reviewing samples in the as received condition resulted in the discovery of consistent surface flaws located along the wing profile as displayed in Figure 3. 1. These pitted areas are possibility due to tooling utilized to manufacture the specimens or oversized media used during the bead blasting process. These defects were constantly found on multiple wings, and initially thought to be prime areas for crack nucleation. But after repeated failures originating from the wing center section and not these flawed locations the process of documenting these flaws was discontinued.

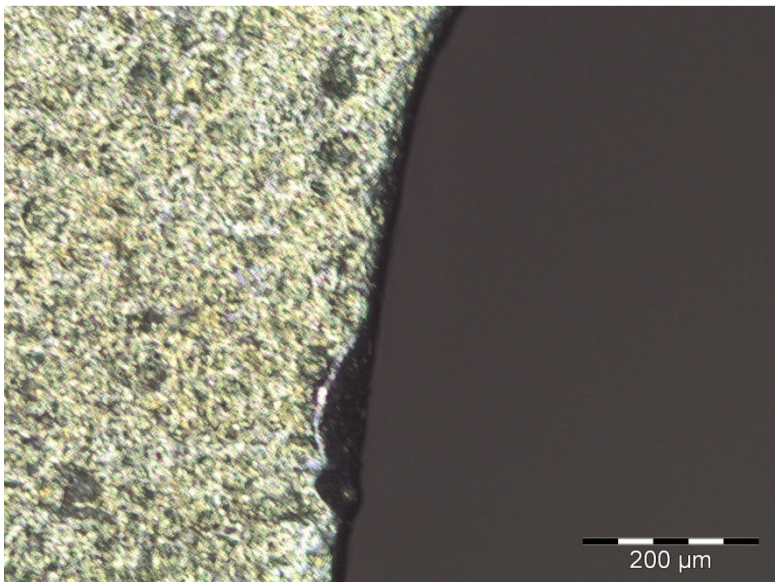

Figure 3. 1 Typical initial inspection flaw found in wing 2-Ti-15Mo-1

3.1.2. Plastic Deformation Testing

The plastic deformation tests for all 24 wings were conducted by Synthes, Inc. Twelve wings of each material were subjected to the procedure described in section 2.2.3. Force and displacement measurements for each individual wing are found in Appendix B. The mean and standard deviation values of maximum force and spring back location that were recorded are displayed in Table 3. 1 and will be used for comparison to the computational results.

Table 3. 1 Plastic deformation force and spring back location values

Material	**Mean Maximum Force**	**Maximum Force Standard Deviation**	**Mean Spring Back Location**	**Spring Back Location Standard Deviation**
	[N]	**[N]**	**[mm]**	**[mm]**
Ti-6Al-7Nb	108.60	3.14	3.536	0.025
Ti-15Mo	115.71	4.20	3.240	0.102

3.1.3. Fatigue Testing

A total of 22 fatigue tests were conducted on 18 wings between Synthes, Inc. and the University of Denver. Eight of the wings were completed by Synthes, Inc. and 14 specimens were completed by the University of Denver per the procedure stated in section 2.2.4. Figure 3. 2 and Figure 3. 3 display the maximum cyclic loading experienced by each sample and the number of cycles to failure. Data points with horizontal arrows indicate the wing experienced run out, while arrows at 45° indicate wings that failed after completing run out on at least one previous test. The wings that were tested by Synthes, Inc. had multiple run outs occur at 500,000 cycles and were offset on the plots for graphical reasons. Appendices B and C contain the test logs for all fatigue test specimens examined by Synthes, Inc and the University of Denver respectively.

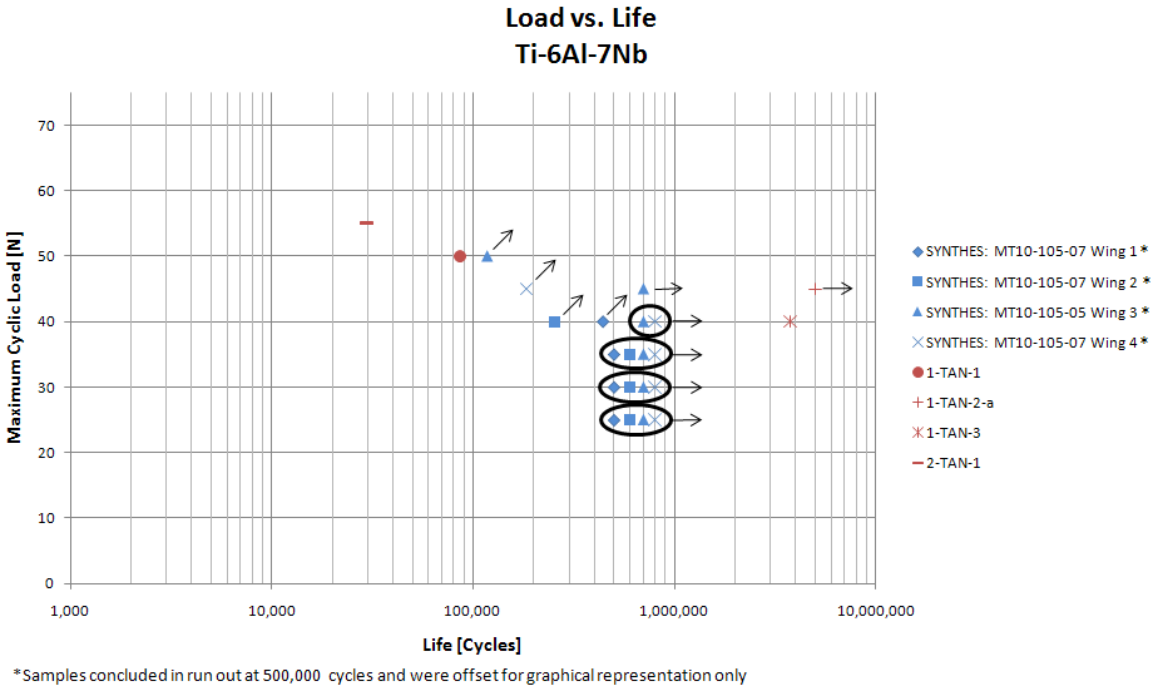

Figure 3. 2 Ti-6Al-7Nb load vs. fatigue life test results

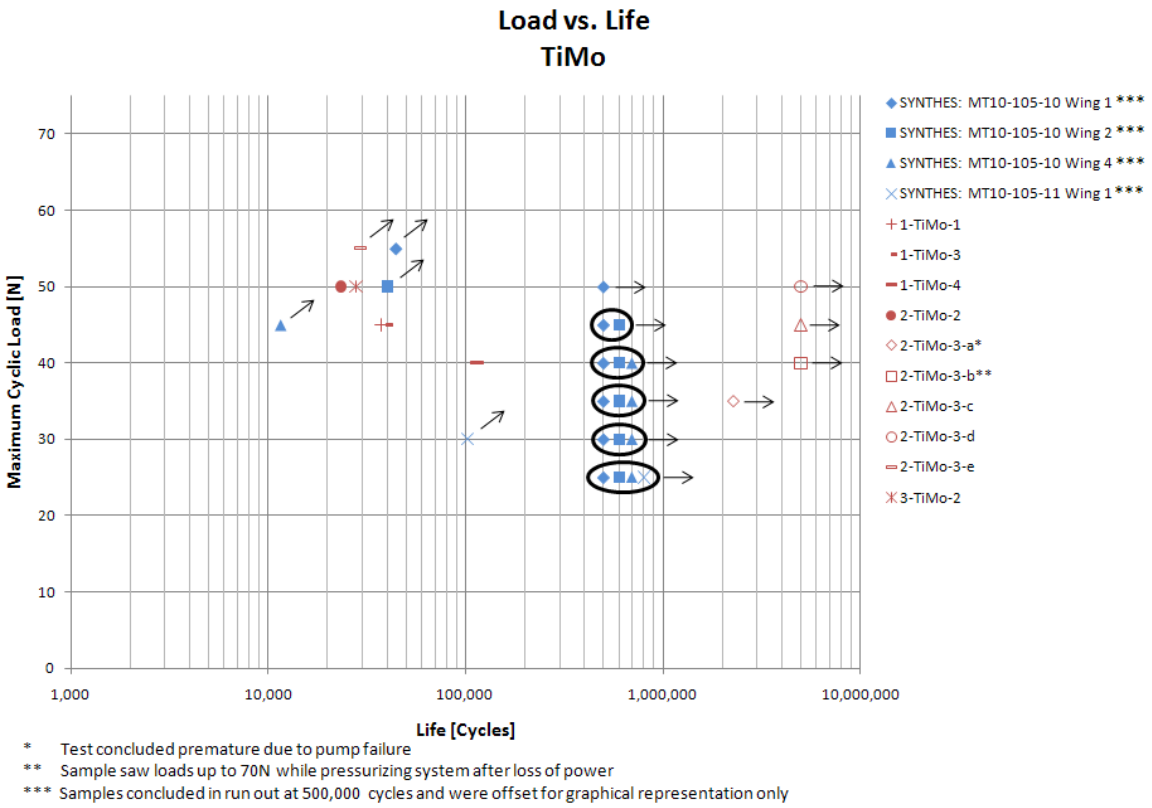

Figure 3. 3 Ti-15Mo load vs. fatigue life test results

During the fatigue test of wing 2-TiMo-3 at the 35 Newton there was loss of pressure to the hydraulic system due to the high pressure unit overheating. This resulted in an early culmination of the test. Once the high pressure unit was operational again testing on the affected sample was resumed. The data gathered from this wing is significant due to the fact that it lead to the connection between the wings tested by the University of Denver and those tested by Synthes, Inc. By choosing to begin fatigue cycling at a low load level the wing will experience cyclic hardening. This rearrangement of the microstructure equated to the specimens achieving longer design lives. After this discovery the data collected for each fatigue test was processed to determine the stiffness by calculating the slope of the force vs. displacement plot for each

completed cycle. A sample of one such plot is displayed in Figure 3. 4. To reduce the quantity of graphs the stiffness values were extracted and placed into tables found in Appendix D.

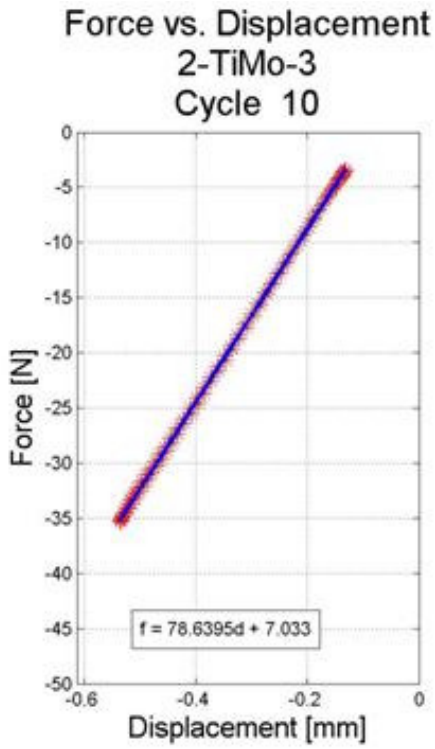

Figure 3. 4 Force vs. Displacement for wing 2-Ti-15Mo-3 for the tenth cycle

3.1.4. Fractography

Two wings of each material tested were chosen to be imaged on the SEM to examine the fractured surfaces. The intent of this failure surface analysis was to verify the material composition at the nucleation site, determine the failure mechanism, and identify the critical flaw that began the fatigue process.

Ti-6Al-7Nb

The first images were taken of wing 2-Ti-6Al-7Nb-1 that failed after 59,232 reversals with a maximum cyclic load of 55 Newtons. From Figure 3. 5 and Figure 3. 6 it is apparent that there was minuscule crack propagation on this wing by the dashed line representing the shear lip. The majority of the implant wing displays characteristic features of micro void coalescence failure. This is a common failure mechanism in ductile materials, where microvoids found at boundaries between the alloying elements and the matrix material unite during plastic deformation, resulting in a rough dull appearance.

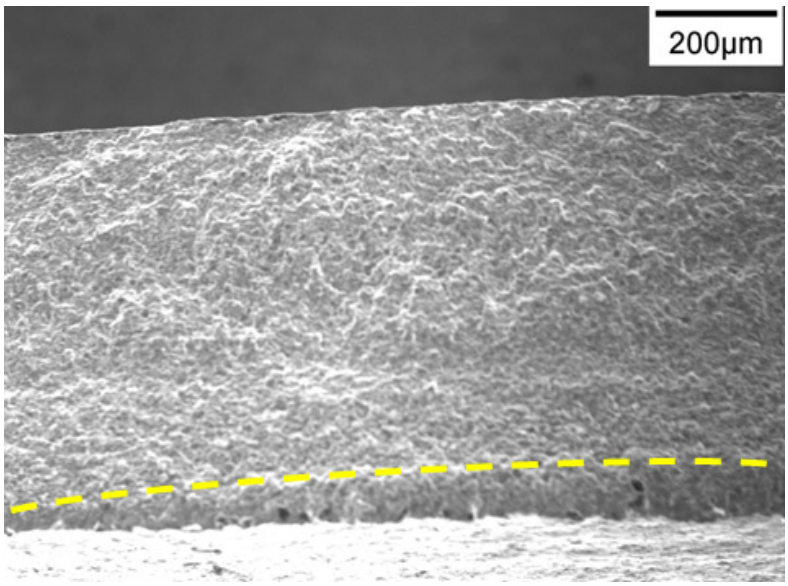

Figure 3. 5 Wing 2-Ti-6Al-7Nb-1 wing fractured surface 100X
Small area of fatigue growth shown below the dashed line followed by large areas of microvoid coalescence

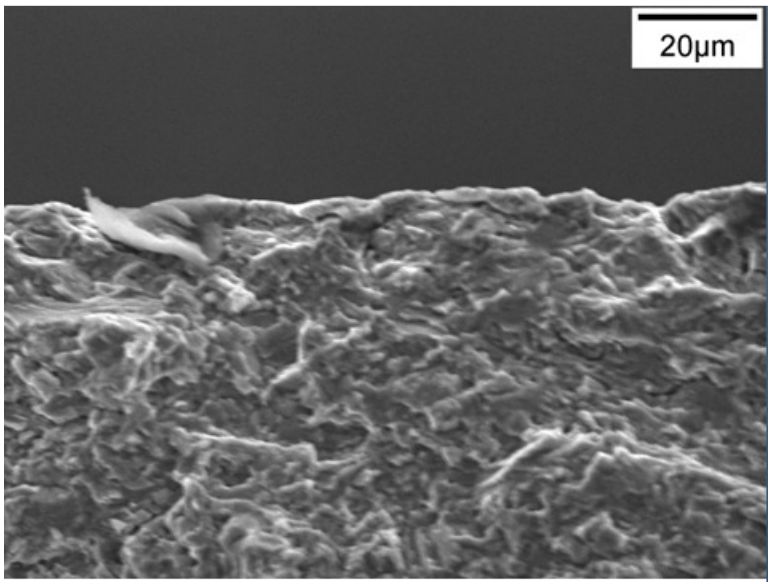

Figure 3. 6 Wing 2-Ti-6Al-7Nb-1 fractured surface 1000X
Characteristic microvoid pattern caused due to ductile tearing

By reducing the loading levels the appearance of fatigue crack growth became more apparent. The following figures were taken on wing 1-Ti-6Al-7Nb-3, which was subjected to a maximum load of 40 Newtons, resulting in a life exceeding 7.5 million reversals. The area circled on each of the SEM images is the location of the nucleation site for this sample. Figure 3. 7 displays the entire cross section of the wing fracture surface where the smooth beachmark zone, characteristic of a fatigue crack behavior, is visible for more than three quarters of the thickness. The repeated reversals in this zone allowed high stress regions directly preceding the crack tip to experience localized plastic deformation, which resulted in the crack becoming blunted, and in turn, arrested the crack propagation. The remaining quarter of the thickness is similar to the previous sample showing markings of ductile tearing as shown in Figure 3. 7. The image displays the torturous nature of ductile tearing and portrays why this mechanism consumes large amounts of energy. The remaining three images for this sample clearly show the river

marks originating from the nucleation site at various magnification levels. In the last image the ratchet lines portray the first initial micro cracks.

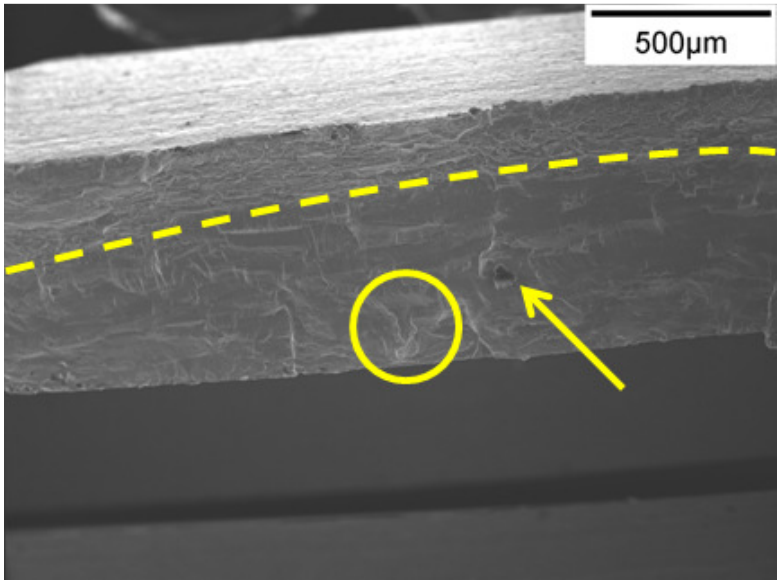

Figure 3. 7 Wing 1-Ti-6Al-7Nb-3 fractured surface 50X

The nucleation site circled was found in the fatigue region. The transition between the fatigue region and the fast fracture region is separated by the dashed line. The dark spot designated by the arrow was an area rich in Niobium.

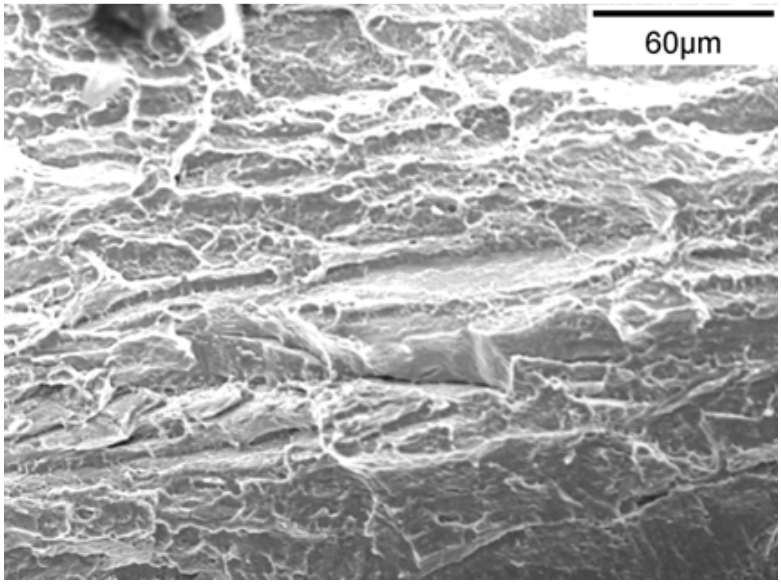

Figure 3. 8 Wing 1-Ti-6Al-7Nb-3 fractured surface 500X

Magnified area above the dashed line in Figure 3. 8 where fast fracture occurred displaying characteristic mirovoid coalescence.

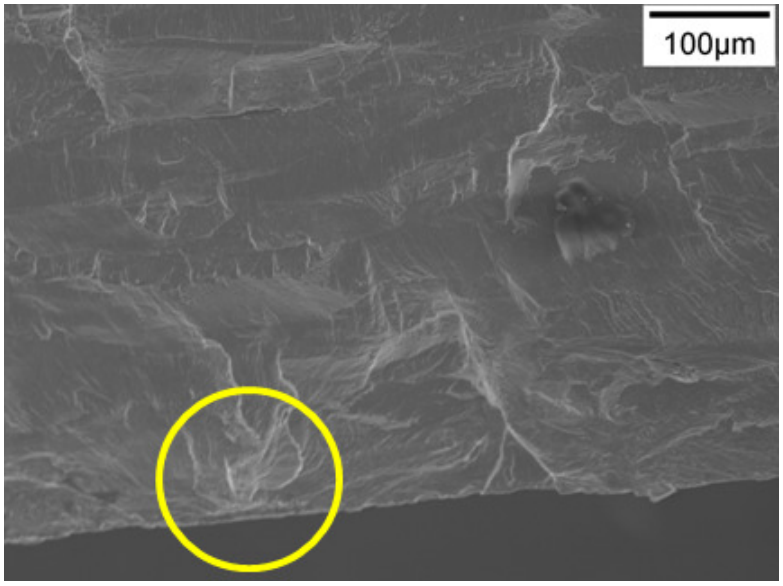

Figure 3. 9 Wing 1-Ti-6Al-7Nb-3 fractured surface 250X

Visible river marks lead back to the circled nucleation site.

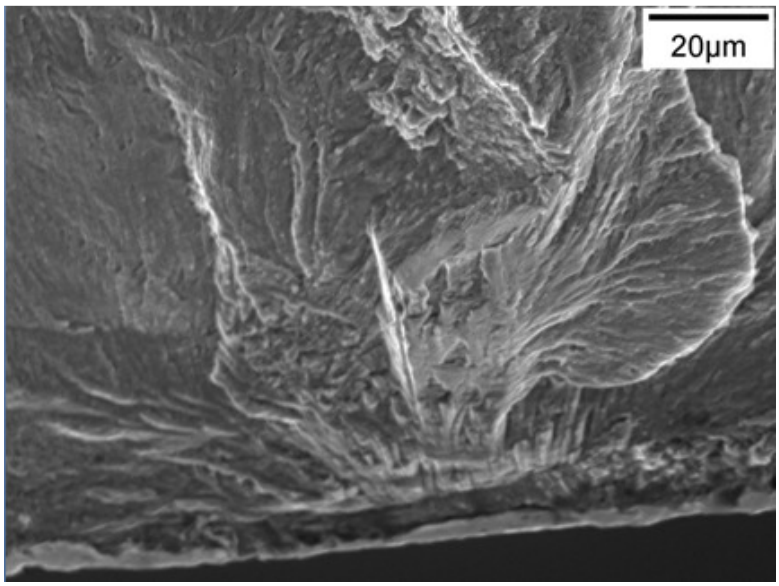

Figure 3. 10 Wing 1-Ti-6Al-7Nb-3 fractured surface 1000X
Magnified area of nucleation site

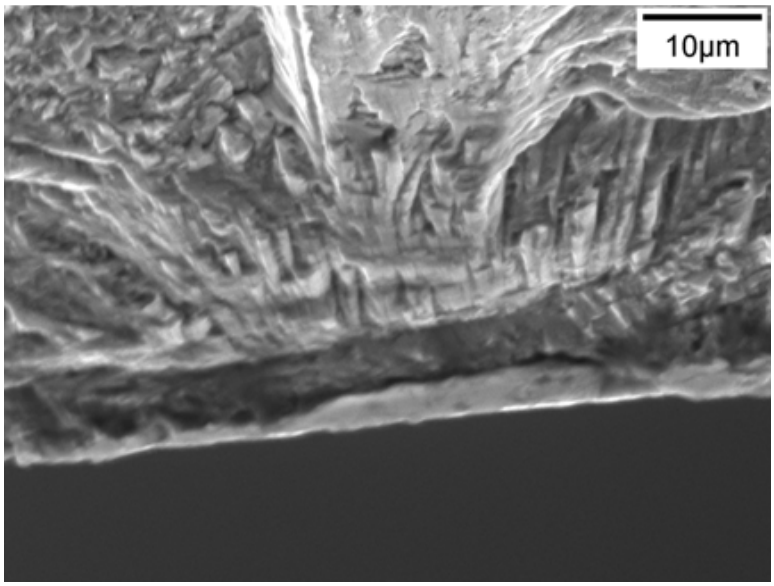

Figure 3. 11 Wing 1-Ti-6Al-7Nb-3 fractured surface 2000X
Ratchet marks potentially depicting lamellar microstructure between the α and β phases

After examining the nucleation site under higher magnification the microstructure of the titanium alloy appears to be the catalyst for fatigue failure. The titanium alloys in question possess both α and β phases, which each have different microstructures. The α

phase possesses the hexagonal closed pack form, while the β phase is body centered cubic. These varying phases are formed during the smelting process by controlling the temperature and pressure of the melt where the transition to β from α occurs at 890°C. In titanium alloys there is a potential for these phases to exist in a lamellar or microlaminated form. This would allow colonies comprised of thin strips of α phase material to be separated by thin strips of β phase to exist (Arata, et al. 2001).

From Figure 3. 11 the ratchet marks appear to be the boundaries between the phases in the material. Assuming this is true the driving failure mechanism for this material would be the bonding properties between the α and β phases.

Ti-15Mo

The Ti-15Mo samples provided similar results of images that displayed fatigue failures. The first wing chosen to be documented was 2-Ti-15Mo-3, which obtained the longest cycle times of any sample with run outs occurring at 40N, 45N, and 50N. The sample originally began testing with a maximum load of 35N, but was stopped short of run out after completing an excess of 5 million reversals. The test interruption was due to the high pressure unit overheating, which triggered an automatic shut down. It is not apparent that detrimental impacts resulted from the interruption. The wing eventually did fail while at a maximum load of 55 Newtons after 58,586 reversals. In total this sample endured 34.5 million reversals. Figure 3. 12 depicts the wing fracture surface with the circles noting two distinct nucleation sites resulting in two separate cracks. The ridge angled at approximately -45° from the horizontal axis displays the ridge that separated each independent crack. The sequential images focus on the nucleation site designated

by the solid circle. Figure 3. 14 was taken in the identical location and magnification as Figure 3. 13 but the sample was rotated along the horizontal axis in the direction out of the page. From this view it can be seen that the depth of the cracks is quite small. In the rectangle found on Figure 3. 15 there are visible striation marks. These lines running parallel to the crack front have been shown to represent the crack growth from individual cycles in numerous studies.

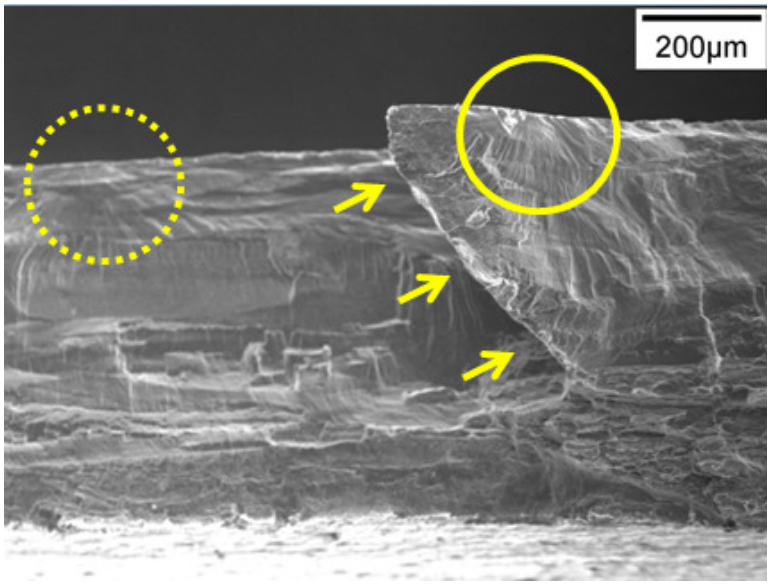

Figure 3. 12 Wing 2-Ti-15Mo-3 100X
Circles denote two distinct nucleation sites resulting in two separate crack fronts. The arrows highlight the fracture surface where the cracks combined.

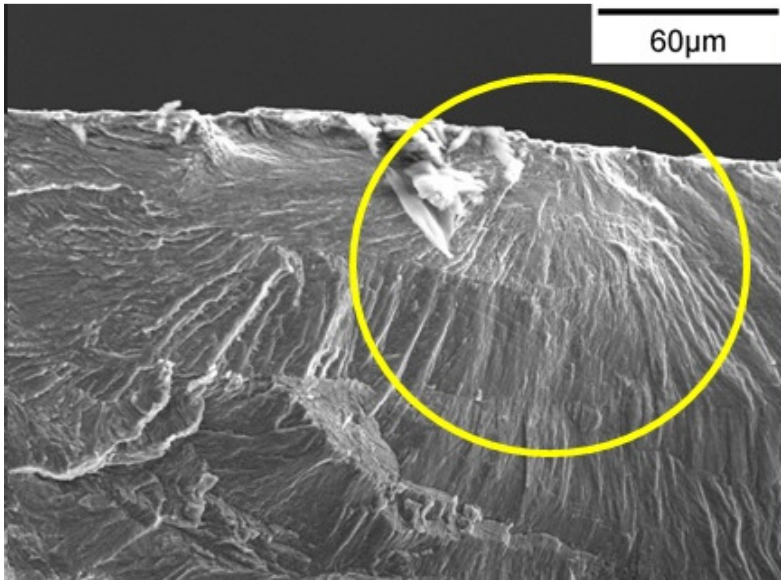

Figure 3. 13 Wing 2-Ti-15Mo-3 500X

River marks flowing back to the nucleation site of the solid circle

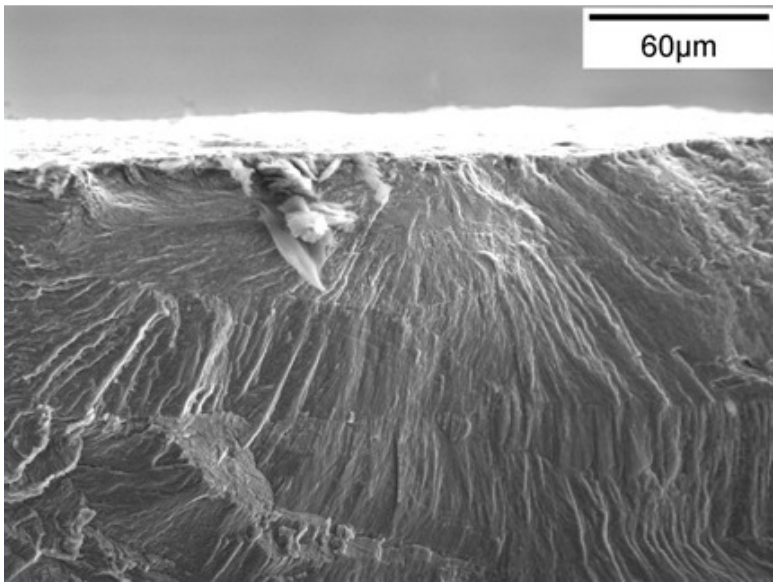

Figure 3. 14 Wing 2-Ti-15Mo-3 500X rotated

Non-uniform bead blasted outer surface is displayed in the lighter region towards the top the image.

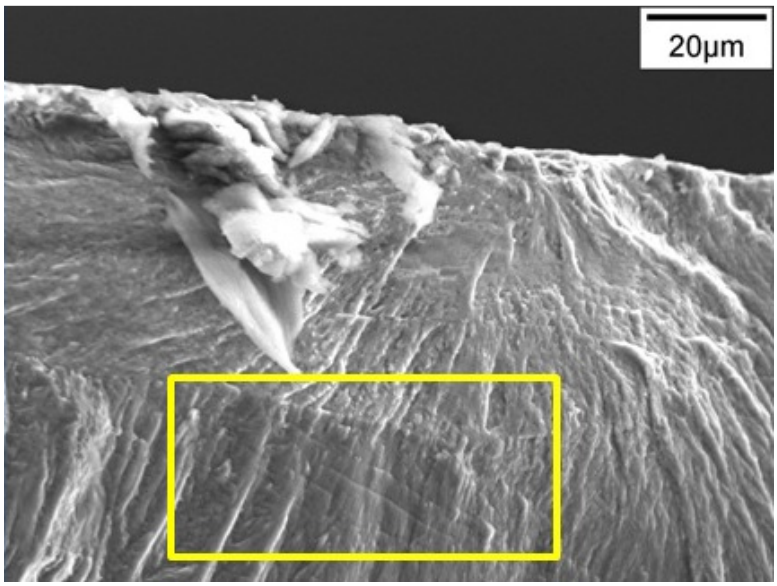

Figure 3. 15 Wing 2-Ti-15Mo-3 1000X
Serration marks are visible inside the noted rectangle

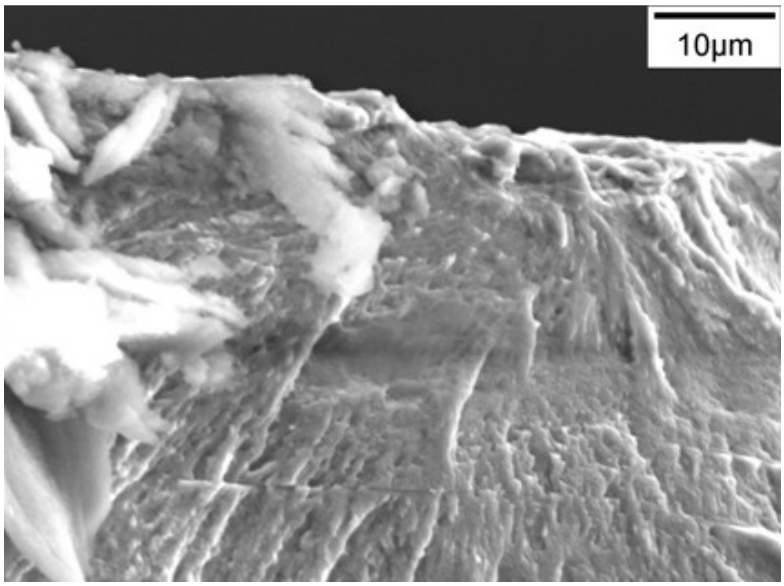

Figure 3. 16 Wing 2-Ti-15Mo-3 2000X
Magnified nucleation site of the solid circle displays no foreign or abnormal particles.

The final wing 3-Ti-15Mo-2 was imaged with the goal to acquire photographs depicting the height of a crack. This was done by rotating the sample within the SEM to view the edge of the fracture surface. The chosen sample was exposed to a maximum

load of 50 Newtons for 55,820 reversals. The darker spots seen on this sample were found to be pockets of Molybdenum by EDS, and were not uncommon along the failure surface. The depth of initial flaws found along the edge was less than five microns, with the maximum gap occurring at the transition where two independent cracks collided.

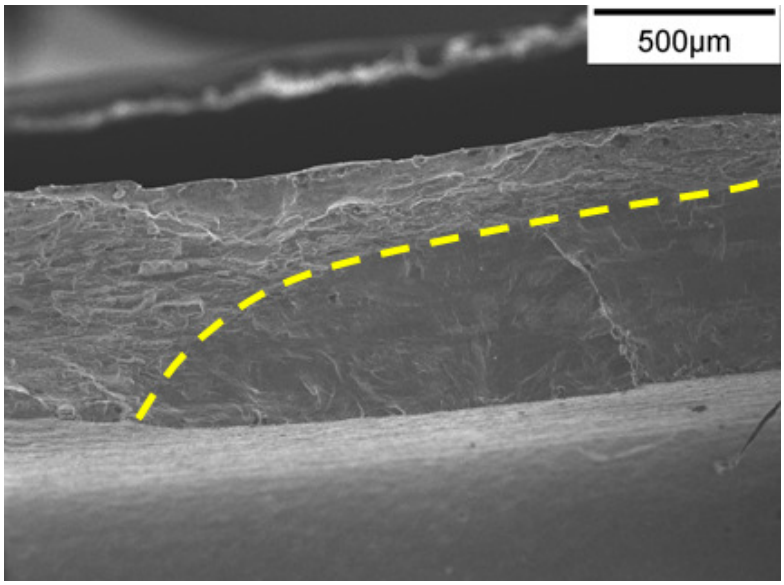

Figure 3. 17 Wing 3-Ti-15Mo-2 50X
Smooth fatigue region and ruff fast fracture region separated by dashed line

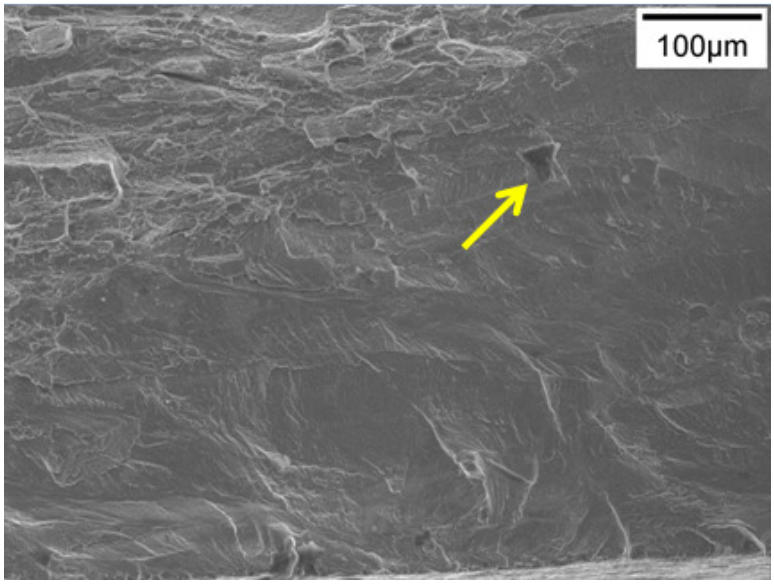

Figure 3. 18 Wing 3-Ti-15Mo-2 250X

Dark region noted by arrow was shown by EDS to be Molybdenum rich

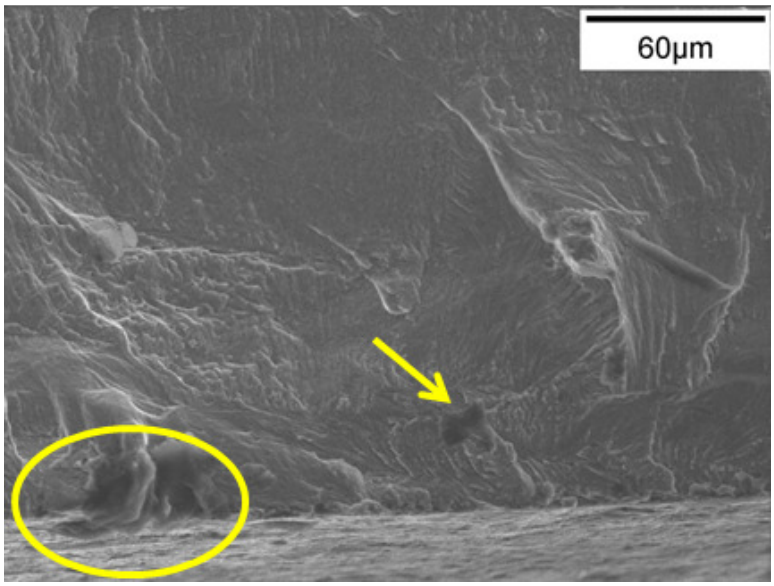

Figure 3. 19 Wing 3-Ti-15Mo-2 500X

Arrow highlights a Molybdenum rich region. Ellipse encloses a crack out of plane of the failure surface.

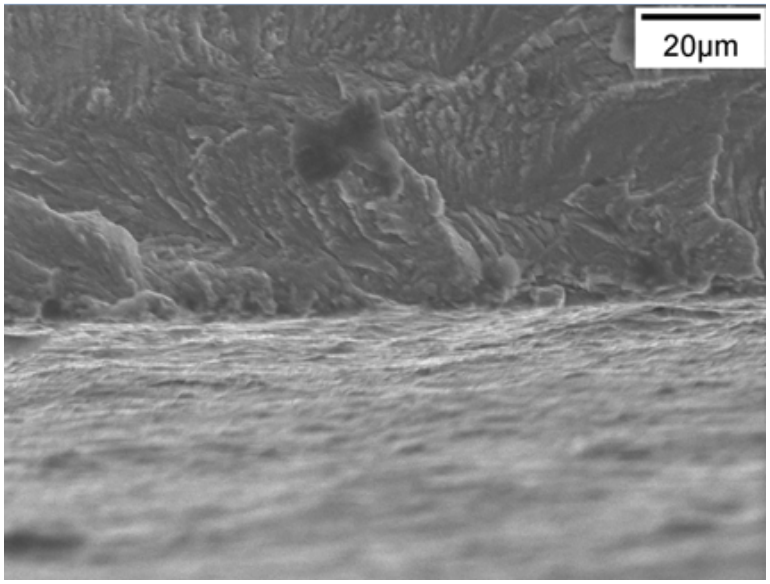

Figure 3. 20 Wing 3-Ti-15Mo-2 1000X

Typical view of interface between the failure surface and outer wing surface.

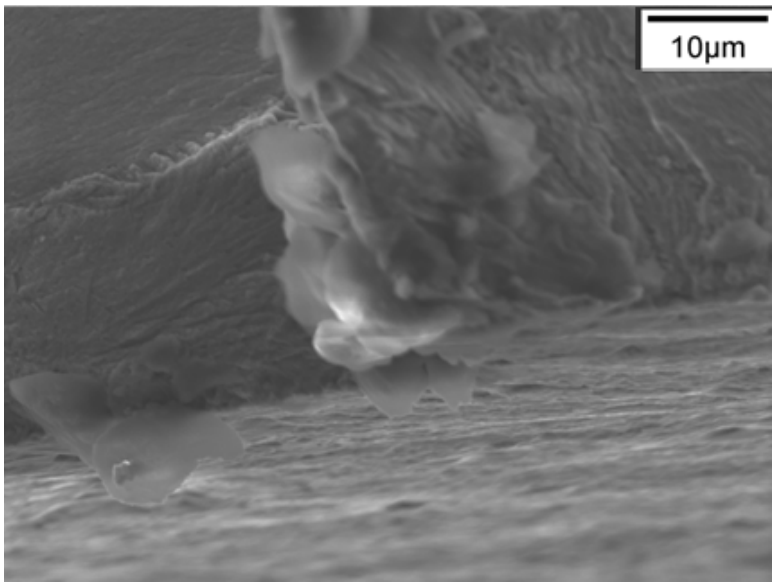

Figure 3. 21 Wing 3-Ti-15Mo-2 2000X

Depth of crack perpendicular to failure surface is approximately 5µm.

The EDS scans verified the material content for Ti-6Al-7Nb and Ti-15Mo finding no abnormalities even when small areas were examined under high magnification. The

detected energy signatures for each material at a nucleation site are displayed in Figure 3. 22 and Figure 3. 23 and are representative of the base materials.

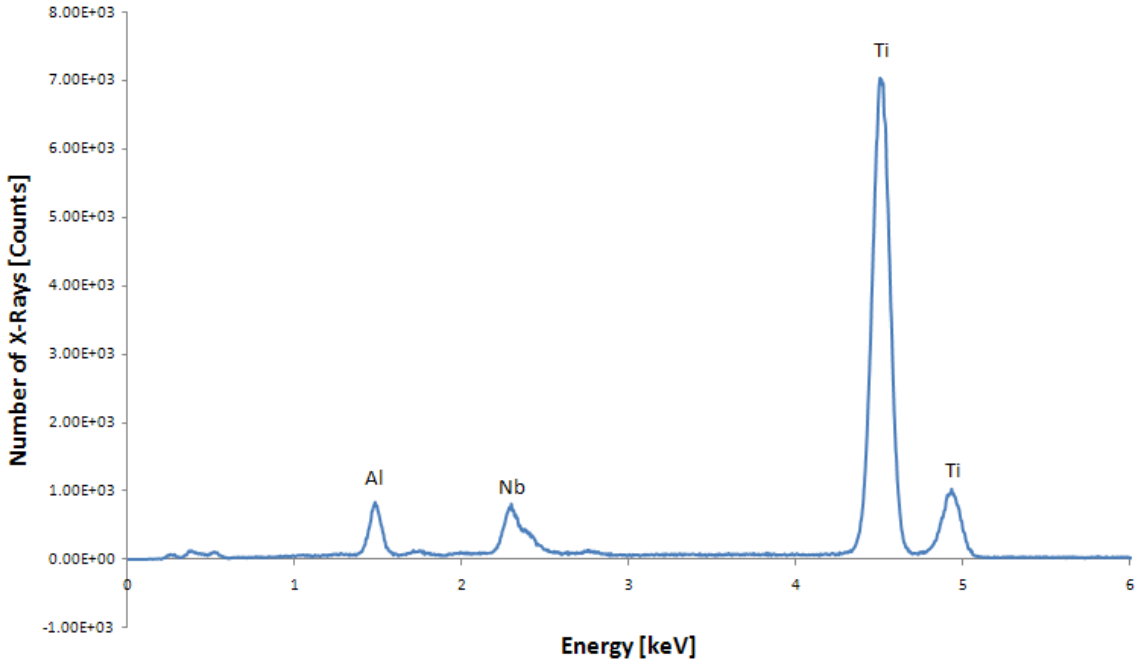

Figure 3. 22 Energy dispersive spectroscopy scan for Ti-6Al-7Nb at nucleation site

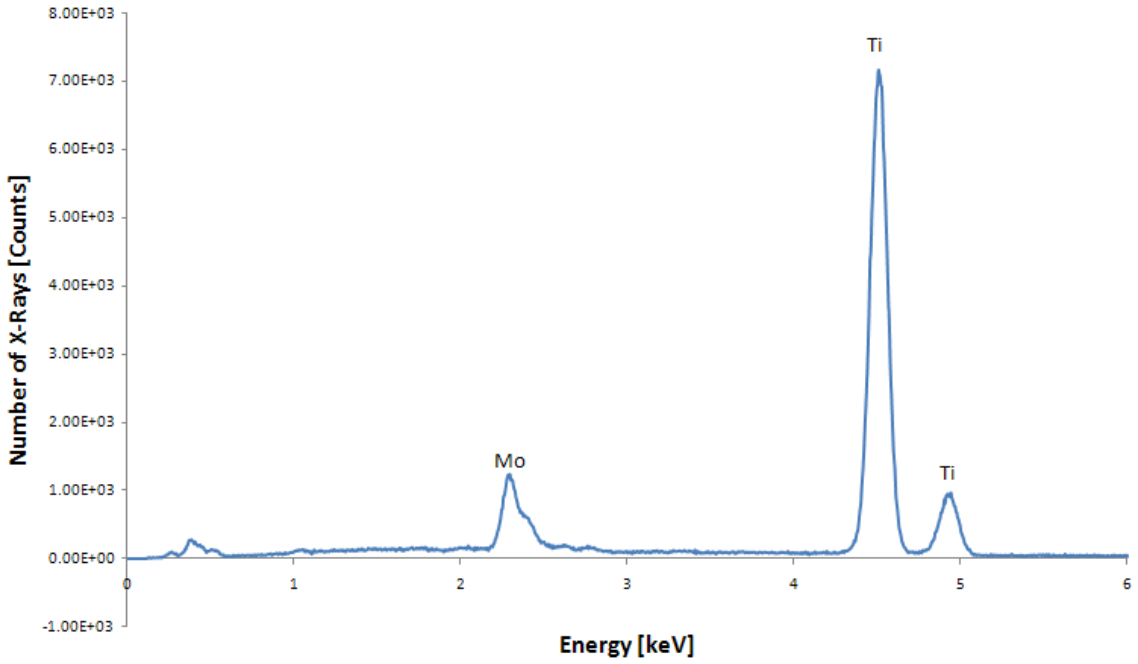

Figure 3. 23 Energy dispersive spectroscopy scan for Ti-15Mo at nucleation site

3.2. Computational Results

3.2.1. Beam Mechanics Results

The moment of inertia was determined for three different cross sections from the wing, and the force calculation was carried out for each using equation (2.5). By this method the most accurate forces found to deflect the beam to a prescribed -5.9mm in the y-direction resulted in an over prediction of force between 1.6 and 2.3 times, depending on the modulus of elasticity used. This displays that the assumptions made to simplify the wing bending problem are not valid for the geometry and loading conditions. More accurate results may be gained by integrating the wing volume by parts to determine the moment of inertia, but due to the tedious nature of this calculation finite element methods were chosen to be employed instead. An additional benefit of choosing to solve using

finite elements will be the ability to alter geometries and loading cases once a simulation is functioning properly.

3.2.2. Material Validation

Table 3. 2 displays the actual values for Ti-6Al-4V that were calculated by the methods described in section 2.3.1 and used to define the elastic plastic material behavior in this study. In accordance with accepted practice only the portion prior to ultimate tensile strength of the engineering stress vs. engineering strain curve was used to calculate the true stress and true strain to reduce the effects of necking (ASTM E 646 1998). The true strain is comprised of the addition of the elastic and plastic components as described by the Ramberg-Osgood relationship shown in equation 3.1 (Ramberg and Osgood 1943). Figure 3. 24 displays the true stress vs. true strain for Ti-6Al-4V.

$$\varepsilon = \varepsilon_e + \varepsilon_p = \frac{\sigma}{E} + \left(\frac{\sigma}{K}\right)^{\frac{1}{n}} \tag{3.1}$$

Table 3. 2 Ti-6Al-4V elastic plastic property definition

Engineering Stress [ksi]	Engineering Stress [MPa]	Engineering Strain [ ]	True Stress [MPa]	True Strain [ ]	Elastic Strain [ ]	Plastic Strain [ ]
0	0.000	0.000	0.000	0.0000	0.0000	0.0000
118	813.000	0.000	813.000	0.0000	7.3909	0.0000
137	944.582	0.010	954.028	0.0100	0.0087	0.0013
142	979.056	0.020	998.637	0.0198	0.0091	0.0107
144	992.845	0.030	1022.631	0.0296	0.0093	0.0203
145	999.740	0.040	1039.730	0.0392	0.0095	0.0298
146	1006.635	0.050	1056.967	0.0488	0.0096	0.0392
147	1013.530	0.060	1074.342	0.0583	0.0098	0.0485

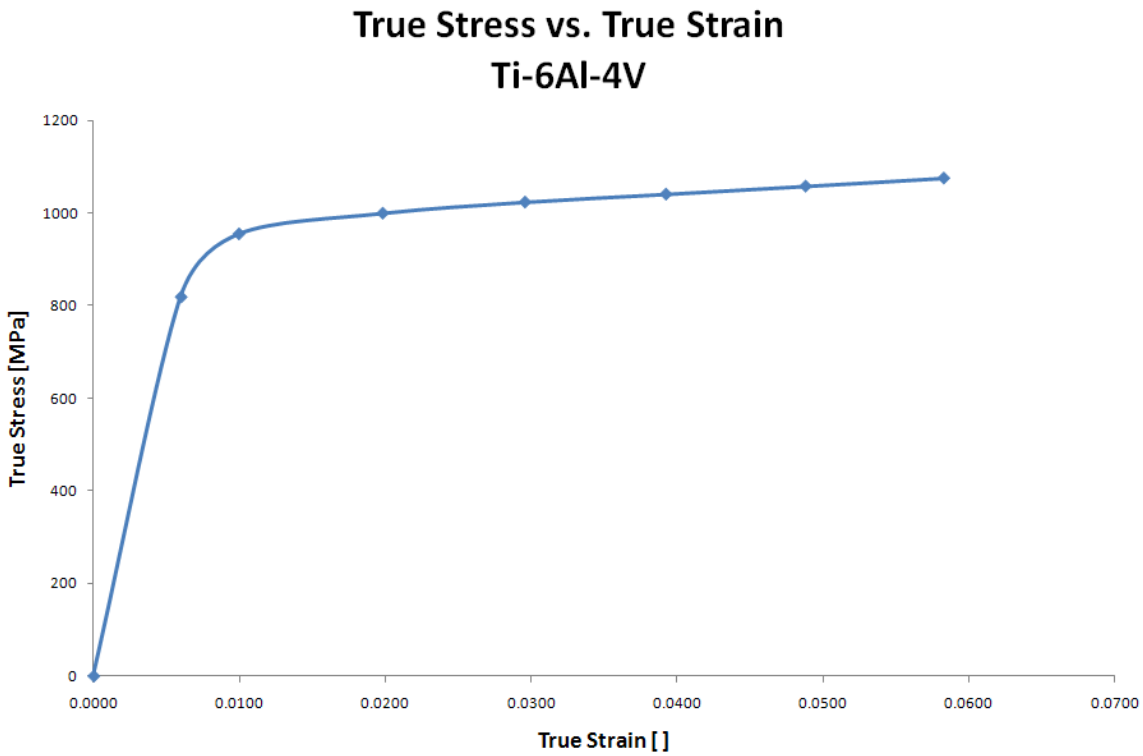

Figure 3. 24 Ti-6Al-4V true stress vs. true strain curve

By applying a power regression curve fit to the true stress vs. true plastic strain plot shown in Figure 3. 25 the Ramberg-Osgood relationship parameters of strength coefficient, K, and the strain hardening exponent, n, were determined. Note that the plot axes are logarithmic and therefore the power law regression is a straight line.

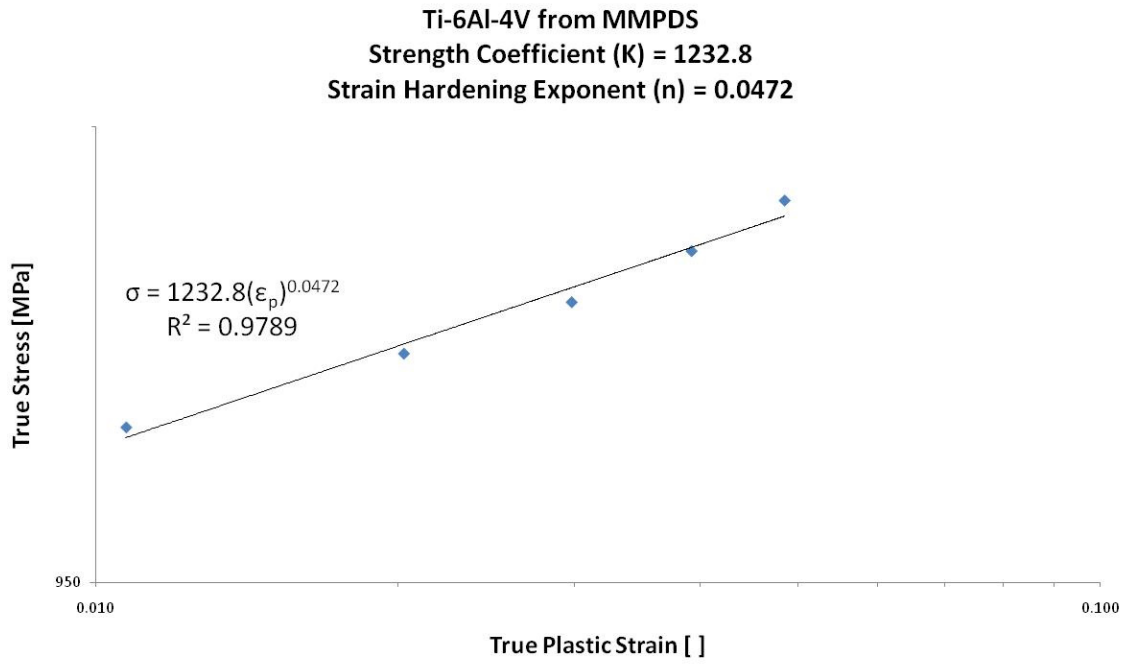

Figure 3. 25 MMPDS Ti-6Al-4V true stress vs. true plastic strain

After the simulation of the cylinder described in section 2.3.1 had converged to a solution the true stress vs. true strain values were plotted on a log-log scale to determine the predicted Ramberg-Osgood parameters. Analysis confirmed the relationship shown in Figure 3. 25 with calculated parameters falling within 3% of the actual values.

3.2.3. Finite Element Analysis

Processor run times for all reduced integration simulations that were evaluated were normally less than thirty minutes when eight 2.8 gigahertz processors were used in parallel to determine a solution. To reduce repetitive calculations simulation steps one and two were typically run only once with the restart option activated. Then simulation step three would be processed for the individual load cases building on the results of the restart file. This allowed most load case simulations to be accomplished in less than ten minutes.

3.2.4. Predicted Motion

For each of the finite element simulations the location after spring back motion (Step 2) was completed and the amplitude of a single cycle was determined (Step 3 minus Step2). These values were compared to mean displacements from data acquired during experimental testing in Table 3. 3 and Table 3. 4. While the percentage differences are significant it is worth noting that the maximum predicted location at Step 2 was mislocated by no more than 1.5 mm, and the experimental setup was designed to measure the displacement of the entire load column. To compare results of cyclic motion the load case of 50 Newtons was chosen as a baseline due to the fact that this was the highest loading level that failed predominately due to fatigue crack growth.

Table 3. 3 Predicted spring back position compared to experimental values

Simulation	Position @ Step 2	Position Δ WRT Ti-15Mo	Position Δ WRT Ti-6Al-7Nb	Error Ti-15Mo	Error Ti-6Al-7Nb
	[mm]	[mm]	[mm]	[%]	[%]
Ti-15Mo Test	-3.2400				
Ti-6Al-7Nb Test	-3.5360				
Original Geometry (baseline)	-4.3757	1.1357	0.8397	35.1%	23.7%
Load Line -1 [mm]	-4.6870	1.4470	1.1510	44.7%	32.6%
Load Line -0.5 [mm]	-4.5257	1.2870	0.9910	39.7%	28.0%
Load Line -0.1 [mm]	-4.4048	1.1648	0.8688	36.0%	24.6%
Load Line +0.1 [mm]	-4.3478	1.1078	0.8118	34.2%	23.0%
Material Properties -10%	-4.6122	1.3722	1.0762	42.4%	30.4%
Material Properties Nominal	-4.4858	1.2458	0.9498	38.5%	26.9%
Material Properties +10%	-4.3655	1.1255	0.8295	34.7%	23.5%
Force Control	-4.2876	1.0476	0.7516	32.3%	21.3%

Table 3. 4 Predicted cyclic displacement values compared to experimental values

Simulation	DISP. @ Step 3 a	DISP. @ Step 3 b	Cyclic DISP. Amplitude	Ti-6Al-7Nb DISP. Amplitude Error	Ti-15Mo DISP. Amplitude Error
	[mm]	[mm]	[mm]	[%]	[%]
Ti-15Mo Test			0.2955		
Ti-6Al-7Nb Test			0.2732		
Load Line -1 [mm] 5 - 50 [N]	-4.6456	-4.2775	0.1841	32.6%	37.7%
Load Line -0.5 [mm] 5 - 50 [N]	-4.4821	-4.0069	0.2376	13.0%	19.6%
Load Line -0.1 [mm] 5 - 50 [N]	-4.3615	-3.7922	0.2847	4.2%	3.7%
Load Line +0.1 [mm] 5 - 50 [N]	-4.3042	-3.6847	0.3097	13.4%	4.8%
Material Prop. -10% 5 - 50 [N]	-4.5757	-3.9967	0.2895	6.0%	2.0%
Material Prop. Nominal 5 - 50 [N]	-4.4464	-3.8648	0.2908	6.4%	1.6%
Material Prop. +10% 5 - 50 [N]	-4.3232	-3.7894	0.2669	2.3%	9.7%
Displacement Control 5 - 50 [N]	-4.3326	-3.7385	0.2971	8.7%	0.5%
Force Control 5 - 50 [N]	-4.2636	-3.6663	0.2986	9.3%	1.0%

3.2.5. Predicted Deformation Force

For each simulation performed, the combined reaction forces for the fixed boundary surface, comprised of the base node set, in the z-direction were summed to determine the force induced by plastic deformation. Reference Figure 2. 17 and Figure 2. 18 for clarification of the fixed boundary surface definition. The summed forces are directly comparable to the force measured by the load cell during physical plastic deformation and are presented in Table 3. 5.

Table 3. 5 Predicted reaction forces compared to actual values

Simulation	Reaction Force	TAN Reaction Force Error	TiMo Reaction Force Error
	[N]	[%]	[%]
Ti-15Mo Test	108.60		
Ti-6Al-7Nb Test	115.71		
Load Line -1 [mm] 5 - 50 [N]	165.66	43.2%	52.5%
Load Line -0.5 [mm] 5 - 50 [N]	146.67	26.8%	35.1%
Load Line -0.1 [mm] 5 - 50 [N]	132.80	14.8%	22.3%
Load Line +0.1 [mm] 5 - 50 [N]	129.65	12.0%	19.4%
Material Prop. -10% 5 - 50 [N]	113.28	-2.1%	4.3%
Material Prop. Nominal 5 - 50 [N]	123.57	6.8%	13.8%
Material Prop. +10% 5 - 50 [N]	133.27	15.2%	22.7%
Displacement Control 5 - 50 [N]	132.17	14.2%	21.7%
Force Control 5 - 50 [N]	131.66	13.8%	21.2%

3.2.6. Predicted Stress and Strain

For each of the simulations conducted in this study, the von Mises stress and logarithmic strain were obtained at the element of interest described in section 2.3.4 at four points in time. These values were used to calculate the mean stress level imparted to the wing and the strain amplitude during cyclic motion. The first time of interest was after the plastic deformation was complete, Step 1. The second time of interest was after the spring back motion was complete, Step 2. The third time of interest was when the cyclic force was at a maximum, Step 3a. The fourth time of interest occurred when the cyclic force was at a minimum, Step 3b. Figure 3. 26 and Figure 3. 27 display the stress

and strain contour plots at various evaluation points in time for a maximum loading of 50 Newtons with the location of the element of interest marked by a star. The strain contour plots have the color scale adjust to show variation only along the failure surface. The predicted stress and strain data for the original geometry covering all load cases evaluated is displayed in Table 3. 6 and Table 3. 7 below and data from all simulations can be found in Appendix E along with stress contour plots for the various implant geometries.

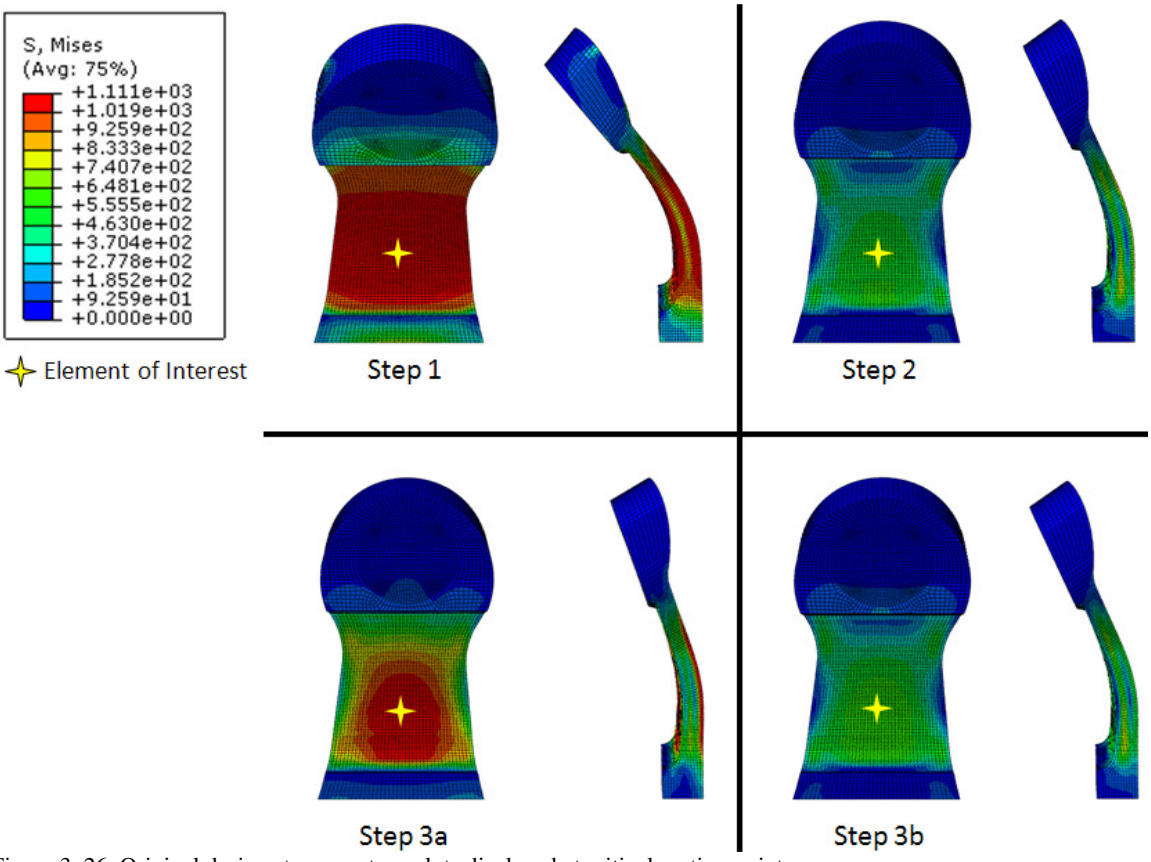

Figure 3. 26 Original design stress contour plots displayed at critical motion points
Step 1: after plastic deformation; Step 2: spring back; Step 3a: maximum cyclic load; Step 3b: minimum cyclic load

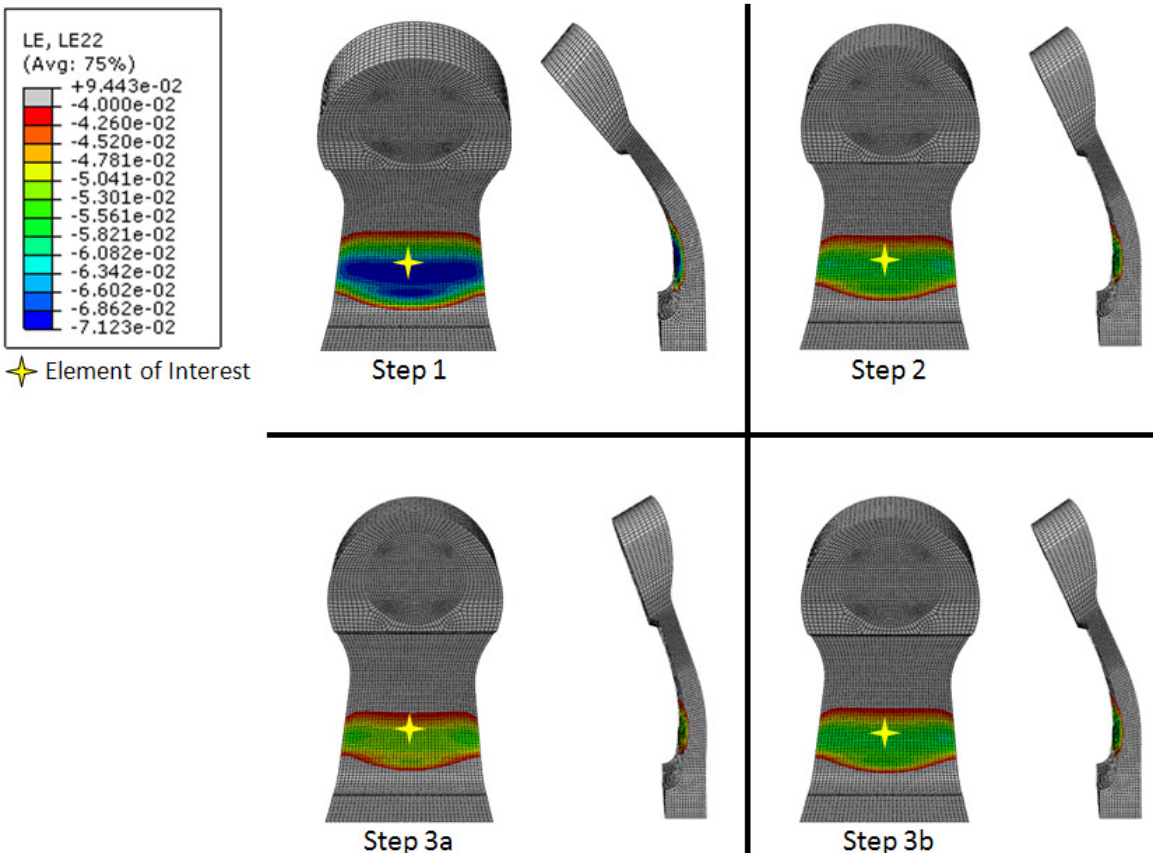

Figure 3. 27 Original design strain contour plots displayed at critical motion points
Step 1: plastic deformation; Step 2: spring back; Step 3a: maximum cyclic load; Step 3b: minimum cyclic load

Table 3. 6 Predicted stress values during cyclic motion for failure surface element

Simulation ORIGINAL GEOMETRY	Min Stress σ_{min} @ Step 3b [MPa]	Max Stress σ_{max} @ Step 3a [MPa]	Mean Stress [MPa]
Sinusoidal 2.5 - 25 [N]	601.10	847.3	724.2
Sinusoidal 3.0 - 30 [N]	606.80	904.1	755.5
Sinusoidal 3.5 - 35 [N]	613.20	962.1	787.7
Sinusoidal 4.0 - 40 [N]	620.50	1022.0	821.3
Sinusoidal 4.5 - 45 [N]	628.50	1083.0	855.8
Sinusoidal 5.0 - 50 [N]	582.10	1091.0	836.6
Sinusoidal 5.5 - 55 [N]	527.30	1091.0	809.2
Sinusoidal 6.0 - 60 [N]	472.50	1092.0	782.3
Sinusoidal 6.5 - 65 [N]	417.10	1093.0	755.1
Sinusoidal 7.0 - 70 [N]	360.80	1094.0	727.4

Table 3. 7 Predicted strain values during cyclic motion for failure surface element

Simulation ORIGINAL GEOMETRY	Minimum Strain ε_{min} @ Step 3b [ ]	Maximum Strain ε_{max} @ Step 3a [ ]	Strain Amplitude ε_a [ ]
Sinusoidal 2.5 - 25 [N]	-5.5921E-02	-5.3547E-02	1.1870E-03
Sinusoidal 3.0 - 30 [N]	-5.5866E-02	-5.3007E-02	1.4295E-03
Sinusoidal 3.5 - 35 [N]	-5.5804E-02	-5.2458E-02	1.6730E-03
Sinusoidal 4.0 - 40 [N]	-5.5735E-02	-5.1892E-02	1.9215E-03
Sinusoidal 4.5 - 45 [N]	-5.5661E-02	-5.1322E-02	2.1695E-03
Sinusoidal 5.0 - 50 [N]	-5.5422E-02	-5.0584E-02	2.4190E-03
Sinusoidal 5.5 - 55 [N]	-5.5185E-02	-4.9838E-02	2.6735E-03
Sinusoidal 6.0 - 60 [N]	-5.4890E-02	-4.9036E-02	2.9270E-03
Sinusoidal 6.5 - 65 [N]	-5.4530E-02	-4.8164E-02	3.1830E-03
Sinusoidal 7.0 - 70 [N]	-5.4109E-02	-4.7227E-02	3.4410E-03

For the simulations where no plastic deformation was imposed on the wing and where the geometry was modified the highly stressed volumes were also determined.

The following figures display values for the highly stressed volume (stress exceeding 815 MPa) with the original geometry listed for reference.

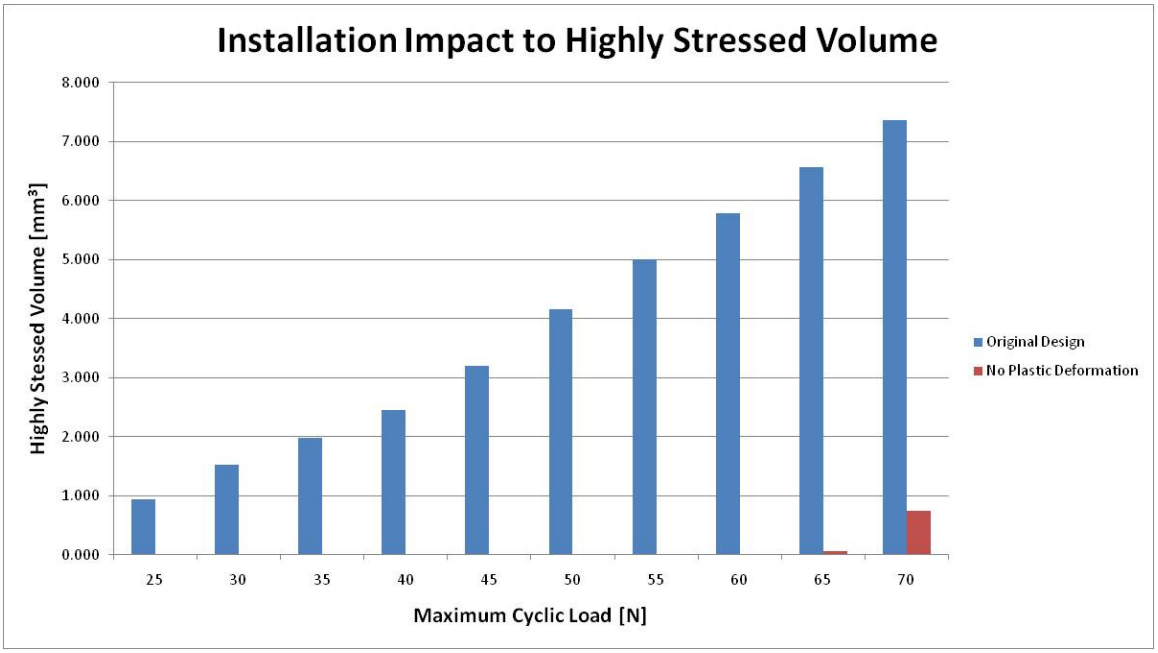

Figure 3. 28 Highly stressed volume of the total wing with no plastic deformation

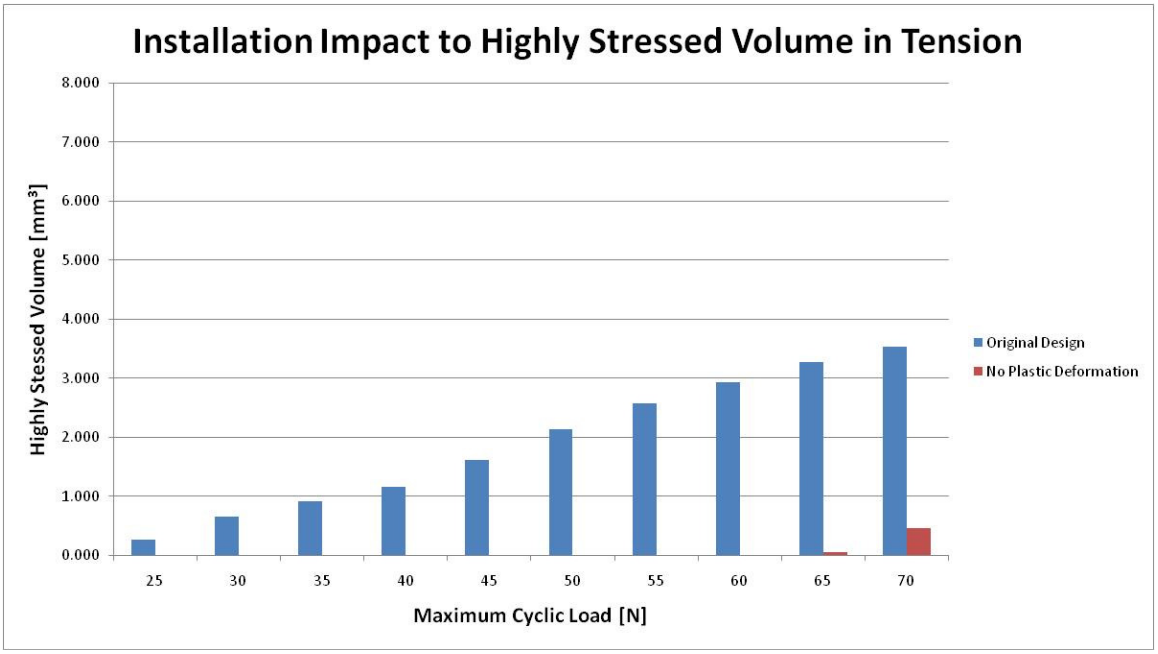

Figure 3. 29 Highly stressed volume in tension for a wing with no plastic deformation

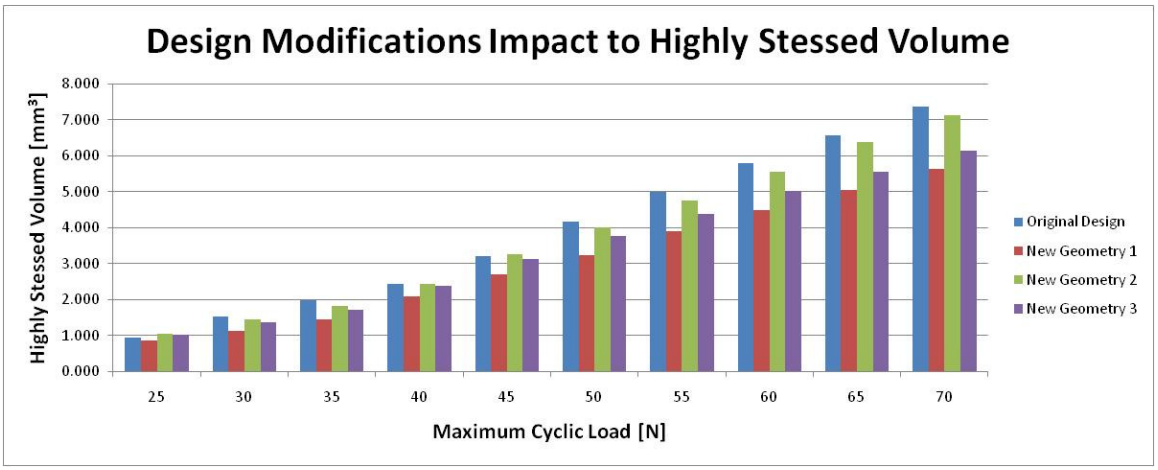

Figure 3. 30 Highly stressed volume for various geometry modifications

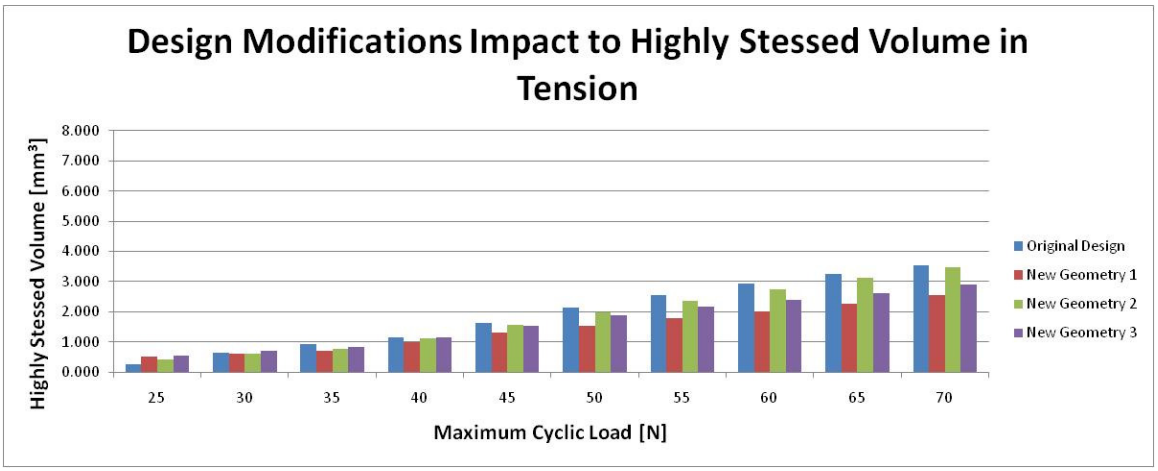

Figure 3. 31 Highly stressed volume in tension for the various geometry modifications

CHAPTER 4. DISCUSSION

4.1. Mesh Convergence

The three tetrahedral mesh densities provided a means to verify that the simulation was converging to a solution. Comparing the sum of the reaction forces in the vertical direction on the fixed cantilever surface will show that the refinement in mesh density yields a converging solution as displayed in Figure 4. 1. Figure 4. 2 and Figure 4. 3 show the stress and strain field convergence respectively. The brick meshes produce a solution slightly larger than the most dense tetrahedron mesh with one twentieth the computational time. The hexahedron values for each converging variable are also displayed in the figures.

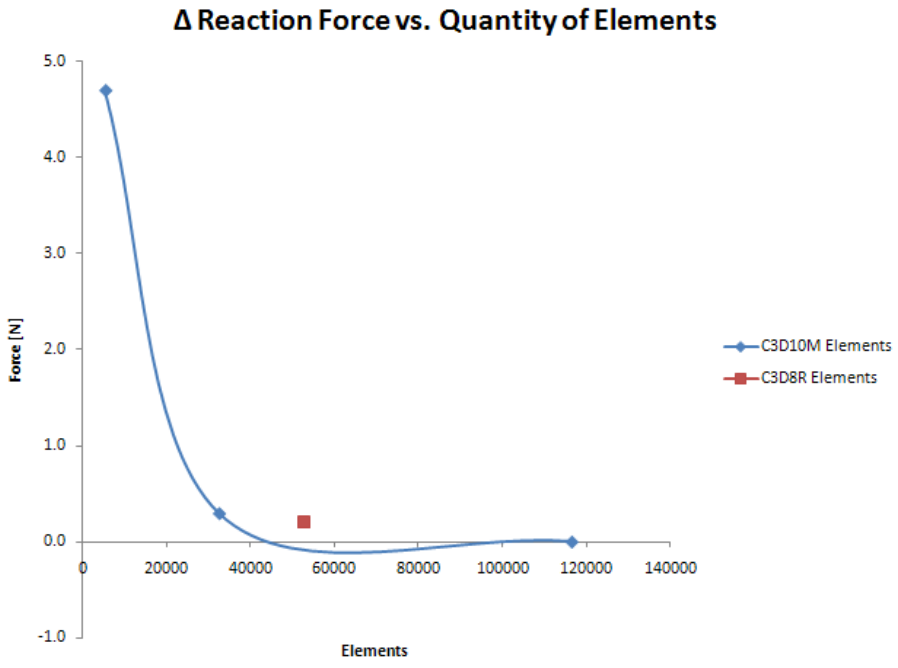

Figure 4. 1 Reaction force mesh convergence

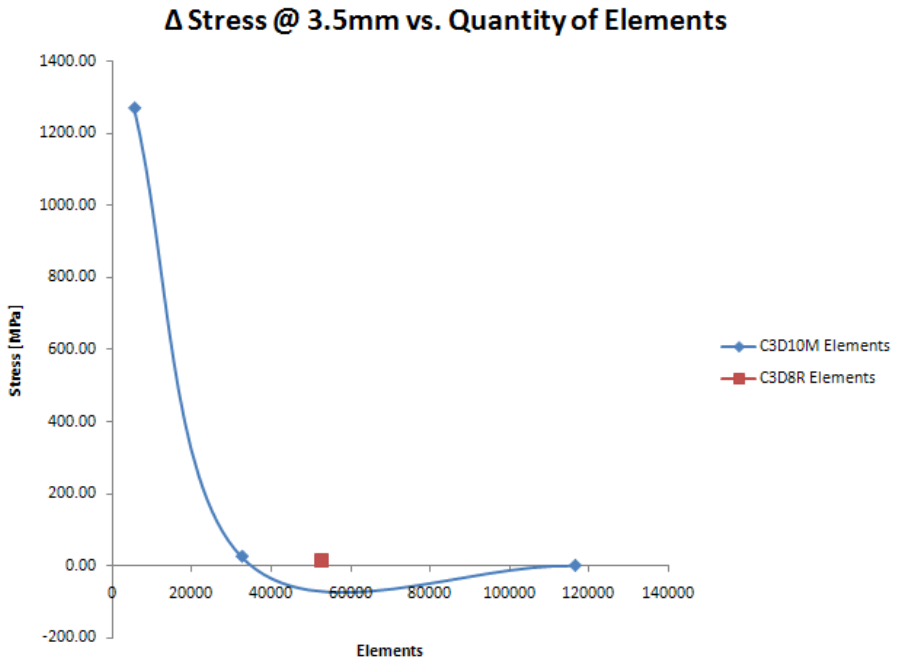

Figure 4. 2 Stress field mesh convergence

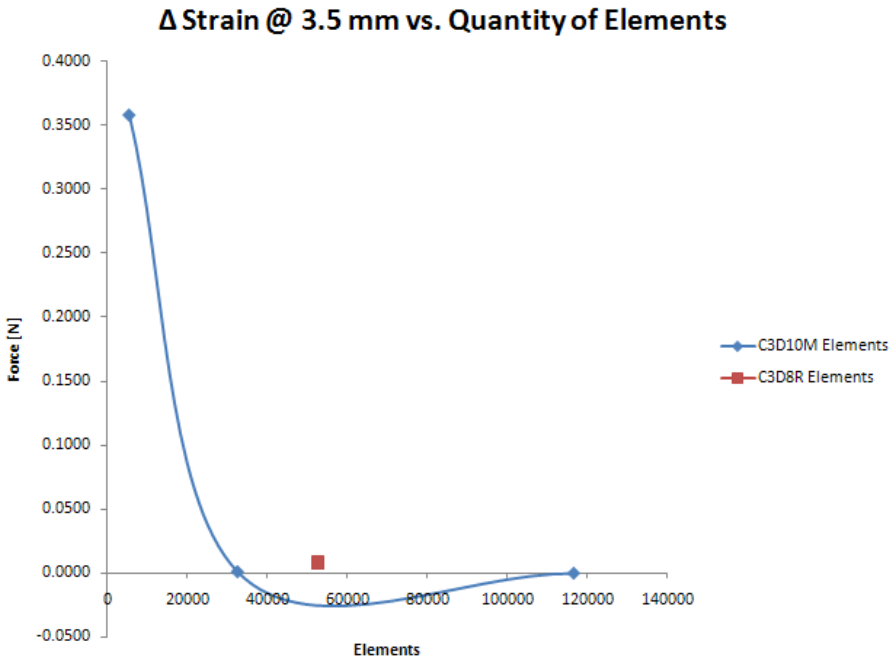

Figure 4. 3 Strain field mesh convergence

4.2. Installation Method Impacts

By comparing the different maximum stress levels between the simulations without plastic deformation, where only Step 3 was utilized, and the full simulation; the elevated stress effect for the StenoFix method of installation becomes evident. Depending on the cyclic load level applied to the specimen the stress component due only to plastic deformation accounts for 43% to 78% of the overall stress in the implant as evaluated by the element of interest. This is a significant portion of the overall stress and would suggest that developing multiple wing spacing widths would allow for shorter deformation spans, which in turn, would lead to reduced stress fields within the implant. The magnitudes of the volume that experience stress levels in excess of yield also indicate the large influence the chosen method of installation has with respect to elevating local stresses.

4.3. Fatigue Behavior Differences Between Materials

Bone has a modulus of elasticity of approximately 30 MPa. The higher modulus of elasticity found in Ti-6Al-7Nb (105 MPa) may incur adverse affect to the surrounding skeletal structure and be deemed unacceptable for reasons other than fatigue performance resulting in Ti-15Mo (78 MPa) being the material of choice for this application. When evaluating on a purely a fatigue standpoint the Ti-6Al-7Nb delivered longer life cycles at equivalent loads when compared to the Ti-15Mo.

4.4. Cyclic Hardening

Stiffness is equal to the force applied to a body divided by the displacement incurred by the force.

$$k = \frac{f}{\delta} \tag{4.1}$$

Stiffness can be shown graphically by calculating the slope of the force vs. displacement plots generated from test data. The figures shown below display the Force vs. Displacement data for the 2-Ti-15Mo-3 specimen through the 50,000 cycle. The equations within each graph represent the linear least squares regression line which models the data. The linear equation models appropriately portray the data with the coefficient of determination values ranging from 0.9958 to 0.9998. From these models it can be seen that the slope gradually increases until approximately 30,000 cycles have been administered to the specimen. Since this is a force controlled test this means that smaller displacements were needed to achieve the equivalent force measurement and the stiffness of the specimen was increasing during initial cycling. The collected data for specimens of both materials show a direct correlation between samples that were given the opportunity to stiffen and an increased number of cycles to failure. The measurable effect of material stiffening is a byproduct of the sample undergoing cyclic hardening, which in turn leads to improvements in fatigue behavior. The tables in Appendix D present the stiffness values for each sample at corresponding cycles.

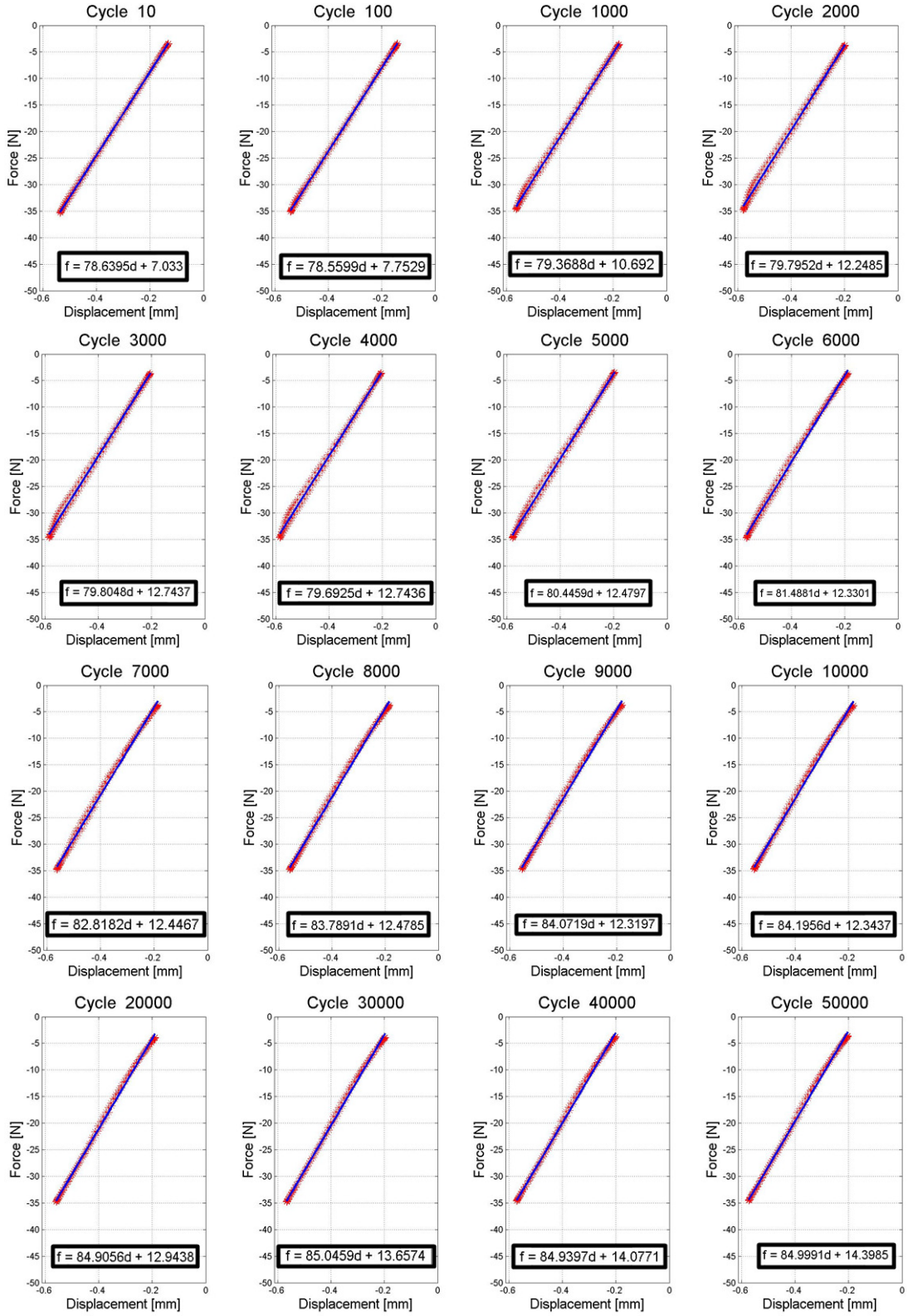

Figure 4. 4 2-Ti-15Mo-3 force vs. displacement – Cycles 10 to 50000 as indicated

4.5. Computational Motion

Section 3.2.4 lists the predicted motion compared to the actual measured displacement at select locations of interest over the implant path of travel. The computational results for the location after spring back motion had errors of 24% for Ti-6Al-7Nb and 35% for Ti-15Mo. These values are dependent on the calculated internal reaction forces that are generated during the displacement step of the simulation, which in turn are dependent on the material definition. It should be noted that the experimental measurements were taken with and LVDT which was measuring the entire load frame as a system and not just the motion of the wing. While the spring back motion predictions are not impressive, the cyclic motion yields much more accurate results with the Ti-6Al-7Nb falling within 1% of the measured values and the Ti-15Mo slightly higher at 9%. This is due to the fact that most of the cyclic motion is being conducted in the elastic region of the material definition, which will be controlled by the modulus of elasticity and the yield strength. For Ti-6Al-7Nb the accurate results can be correlated to the similar elastic behavior found in Ti-6Al-4V.

4.6. Material Definition Computational Effects

4.6.1. Material Validity

From section 3.2.1 it was found that the computational model over predicted the Ramberg-Osgood strength coefficient, K, by 0.25%, and the strain hardening exponent, n, by 2.97%. These values are well within acceptable limits and justify that the material definition is adequately portrayed in the finite element software. These results confirm

that the software is accurately applying the material properties which were supplied. It is of importance to note that the properties used during computational efforts were for Ti-6Al-4V and not the actual specimen materials of Ti-6Al-7Nb and Ti-15Mo.

4.6.2. Material Variation Simulations

By varying the definition of Ti-6Al-4V over a range of 20% centered about nominal the predicted required force to deform the specimen -5.95mm covered a span of 18.4%. With an impact of near one-to-one between changes in material definition to generated internal forces it may be concluded that the material definition carries a fair amount of weight in the prediction of the internal stress field. The effect of altering the material properties was less of a driving factor on the spring back location with the predicted results only accounting for a maximum of 8% of the error when compared to experimental test specimens.

4.7. Load Line Location Sensitivity

From the four simulations that evaluated varying load location, directly affecting the moment arm, it can be seen that this parameter has large impacts on the motion and internal stress field. By altering the moment arm over a range of 1.1mm, variations in the reaction force needed to displace the arm 5.95mm spanned 33% of the actual measured force witnessed during physical testing. The displacement predictions showed similar values that coved a range of 46% of the actual measured spring back distance when compared to testing results. With the current fatigue test procedure it would not be difficult to mislocate the implant in relation to the loading anvil by one millimeter. This

round of simulations makes it evident that the implant design is sensitive to the loading location.

4.8. Investigation of Design Modifications

From the tables and figures found in section 3.2.6 and Appendix E it can be seen that the wing geometry plays a key role in defining the localized stress fields of the spinal implant. The simulation New Geometry 1 predicts reduced stresses in the localized area where actual failures occurred in addition to a lower volume of highly stressed elements, but also changes the predicted motion of the wing. It was unclear whether the curved final shape was desired to reduce the surface area in contact with the vertebrae or had some other purpose. This is a valid concern since historically it has been shown that areas of bone that are in contact with metallic implants experience degradation. Also noteworthy is the maximum stress predicted on the failure surface is two percent higher than the original model. These stresses are located in a region that has an increased cross sectional area compared to the location of typical failure and are therefore deemed negligent. The mean stress levels during cyclic motion were also reduced, which would provide increased fatigue lives. While this simulation yielded promising reductions in stress and mean stress levels, the inability to recreate a deformed structure similar to the original design led to the next two simulations.

Simulation New Geometry 2 made a slight correction to the curvature of the wing failure surface, which resulted in a more accurate prediction of motion with respect to the original specimen. While the stress field results did not show as large of an improvement as simulation New Geometry 1 they were an improvement to the original design and the

total volume of highly stressed element was reduced. The overall wing thickness of simulation New Geometry 2 is approximately equivalent to the original sample indicating that the enhanced performance is directly related to the smooth derivative of curvature of the failure surface. The modification of New Geometry 2 impacted the upper surface of the implant wing with higher stress levels. These increases are negligible due to the fact that the increase is on the order of two percent and these stresses will be in compression during the implant cycle life ultimately resulting in meager improvements to fatigue attributes. With this simulation the mean stress levels were again reduced, which will show beneficial fatigue performance results. Figure 4. 5 displays the cross section of the original wing with each of the modified geometries overlaid for comparison. It should be noted that the reduction in local stresses for New Geometry 2 is directly related to the alterations in curvature due to the fact that the cross sectional area is approximately equal to the original design. New Geometry 1 and New Geometry 3 increased the wing thickness in addition to improving the surface curvature resulting in greater reductions in local stress.

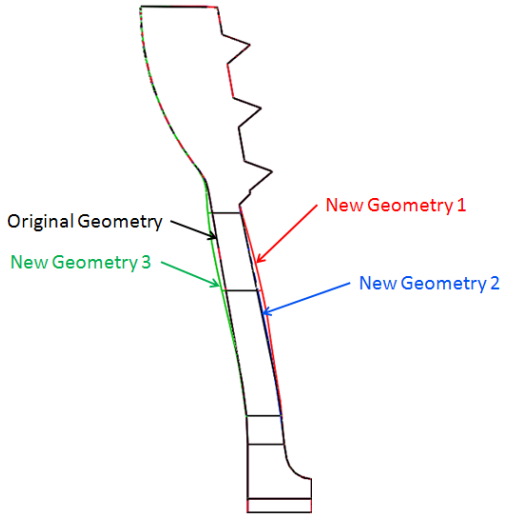

Figure 4. 5 Cross sectional comparison of design modifications

The final simulation, New Geometry 3, yielded results inferior to the simulation New Geometry 2 at the element of interest, but had an overall reduced volume of highly stressed elements. The area of increased stress on the failure surface is larger and the predicted mean stress is higher than the New Geometry 2 simulation. The upper surface stress fields of this simulation and simulation New Geometry 2 are approximately equivalent culminating in little impact to the overall performance of the design. The motion of this simulation closely resembled the dynamics of the original implant and the increased wing thickness may compensate for the predicted increase in stress at the element of interest.

In conclusion, from this round of simulations it is clear that all three geometry modifications reduced the amounts of highly stressed volumes compared to the original. Due to the fact that New Geometry 2 and New Geometry 3 can display these benefits, in addition to duplicating the deformed shape of the original design, they are the clear choices for future prototype testing.

4.9. Life Prediction Modeling

Strain life fatigue behavior is commonly modeled using the four parameter equation 4.2, which is the summation of the Coffin-Manson and Basquin relationships (Saitova, et al. 2009). This equation employees four material based properties, the modulus of elasticity, and number of reversals to determine the strain amplitude. More commonly the strain amplitude is known and the number of cycles is determined using numerical methods.

$$\frac{\Delta\varepsilon}{2} = \varepsilon_a = \frac{\Delta\varepsilon_e}{2} + \frac{\Delta\varepsilon_p}{2} = \frac{\sigma_f'}{E}(2N_f)^b + \varepsilon_f'(2N_f)^c \quad (4.2)$$

This model fails to account for the mean stress effect, but was modified by Morrow to include this parameter as shown in equation 4.3.

$$\frac{\Delta\varepsilon}{2} = \frac{\sigma_f' - \sigma_m}{E}(2N_f)^b + \varepsilon_f'(2N_f)^c \quad (4.3)$$

The data collected in this study was insufficient to calculate the material fatigue parameters for the strain life models, so published values for Ti-6Al-4V (Saitova, et al. 2009) were used in conjunction with the monotonic Ramberg-Osgood variables calculated in section 3.2.1. Due to the relatively close proximity of Ti-6Al-4V material properties to Ti-6Al-7Nb the substituted parameters should be applicable. To apply this model to the Ti-15Mo samples proper values for the four parameters would need to be determined.

In the graphs below the Strain vs. Time and Stress vs. Time for an element located on the failure surface are shown in Figure 4. 6 and Figure 4. 7 Stress vs. Time at element of interest for existing installation process. The dotted line in Figure 4. 7

graphically shows the mean stress witnessed along the failure surface. Figure 4. 8 and Figure 4. 9 display the predicted curves for load vs. life and strain amplitude vs. life respectively. While further testing would be required to validate this predictive model the current physical data available shows promise in forecasting fatigue life spans.

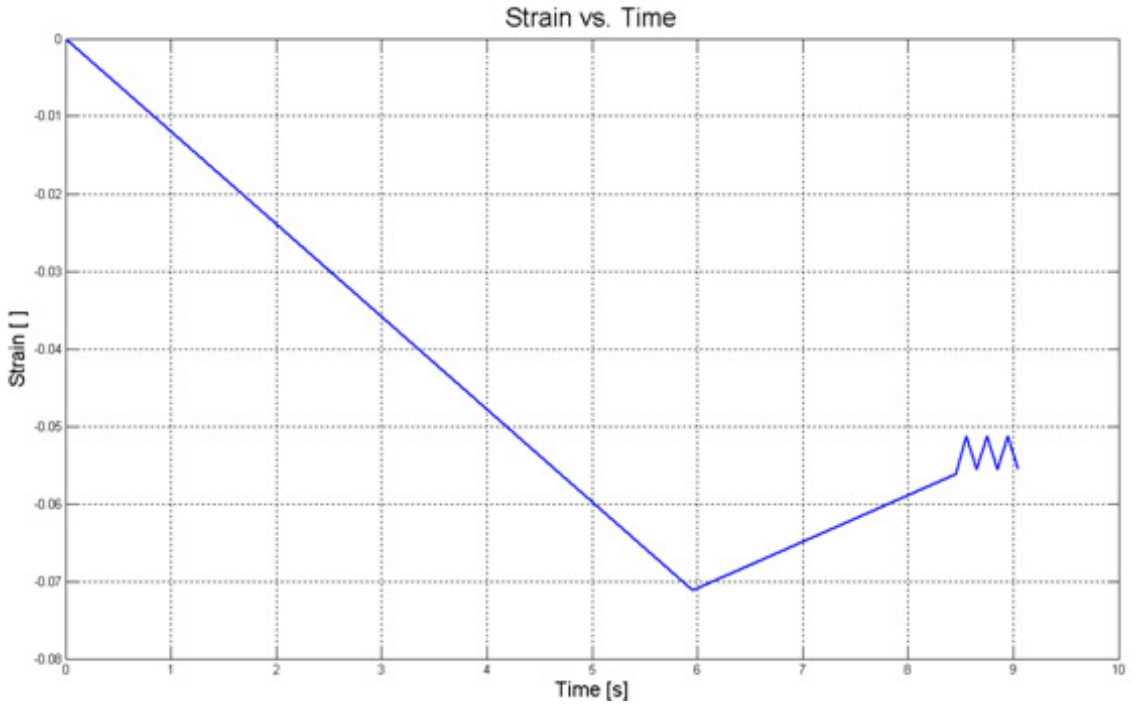

Figure 4. 6 Strain vs. Time at element of interest for existing installation process

Figure 4. 7 Stress vs. Time at element of interest for existing installation process
(mean stress is designated by the dashed line)

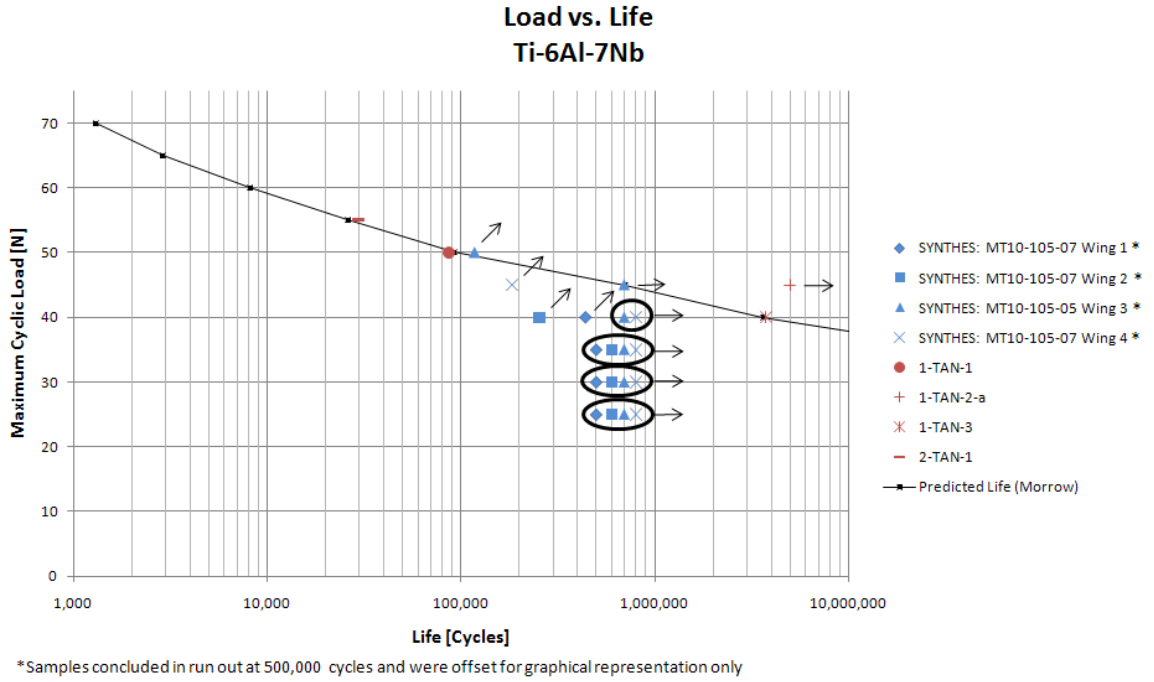

Figure 4. 8 Max cyclic load vs. life for Ti-6Al-7Nb including predicted life (Morrow)

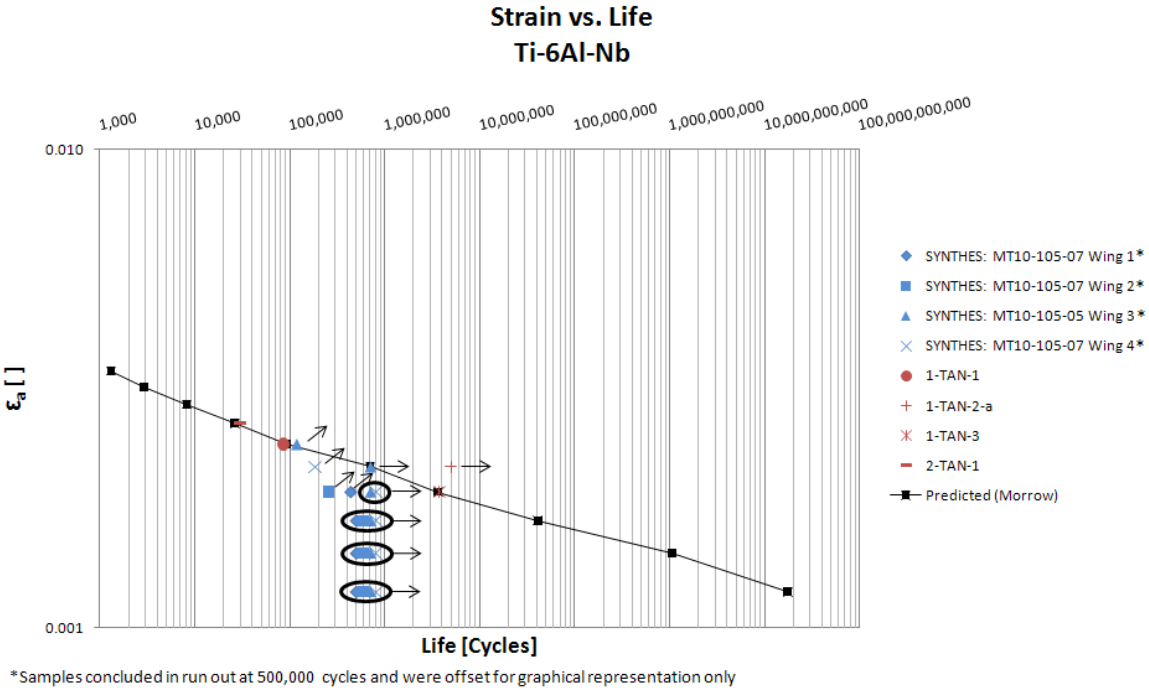

Figure 4. 9 Strain amplitude vs. life for Ti-6Al-7Nb including predicted life (Morrow)

4.10. Improvements and Future Work

Multiple instances of material dependent quantities of interest were presented in this chapter. The effort to develop an elastic-plastic stress strain relation for each of the materials in question would allow more analysis to be conducted computationally before actual hardware is fabricated and tested. After completing both physical and computational experiments in this study without question the physical testing involves greater time and expense. By pushing a larger portion of the design phase into the computational arena an opportunity to reduce cost and develop a superior product is available. Without question the physical testing must at some point be conducted, but fewer iterations using actual hardware will result in monetary savings.

With the proven dependence of loading location any future test should consider modifications to the mounting fixtures. The incorporation of a lead screw design would make it possible to set and repeat the location of the implant wing in relation to the loading anvil more precisely. Having a more consistent moment arm should reduce the fatigue scatter experienced during physical testing. On the fatigue specimens the serrations could also be removed resulting in repeatable cyclic loading points. These two alterations could be used on the computational side to correctly place the load line at a known location, which will in turn improve the predictions of field variables.

After comparing the simulation results running fatigue tests on samples of New Geometry 2 may prove rewarding. There is a potential to see an increased performance without any associated costs.

The final, and likely most beneficial, recommendation would be to consider the potential of manufacturing the implant wings in a similar configuration as to the one described in this study as plastically deformed. Upon installation the wings would be forced apart imparting an overload to the wing area resulting in residual compressive stress on the failure surface. Initial rough estimates forecast that this modification in philosophy would result in the installation process actually improving fatigue life. Assuming the strain magnitudes for this case are equivalent, but opposite in direction, as those calculated in section 4.9, life prediction would be increased by six orders of magnitude. The following figures display the Stain vs. Time, Stress vs. Time, and the predicted life if the installation procedure were altered.

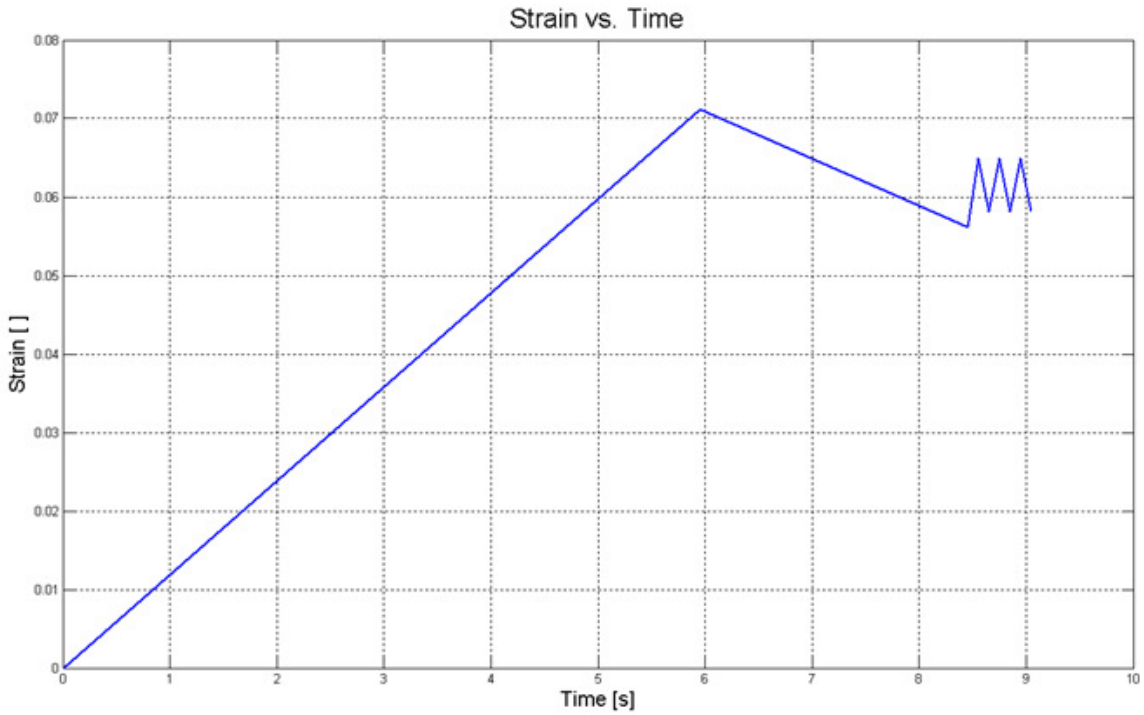

Figure 4. 10 Stain vs. Time at element of interest for modified installation process

Figure 4. 11 Stress vs. Time at element of interest for modified installation process (mean stress is designated by the dashed line)

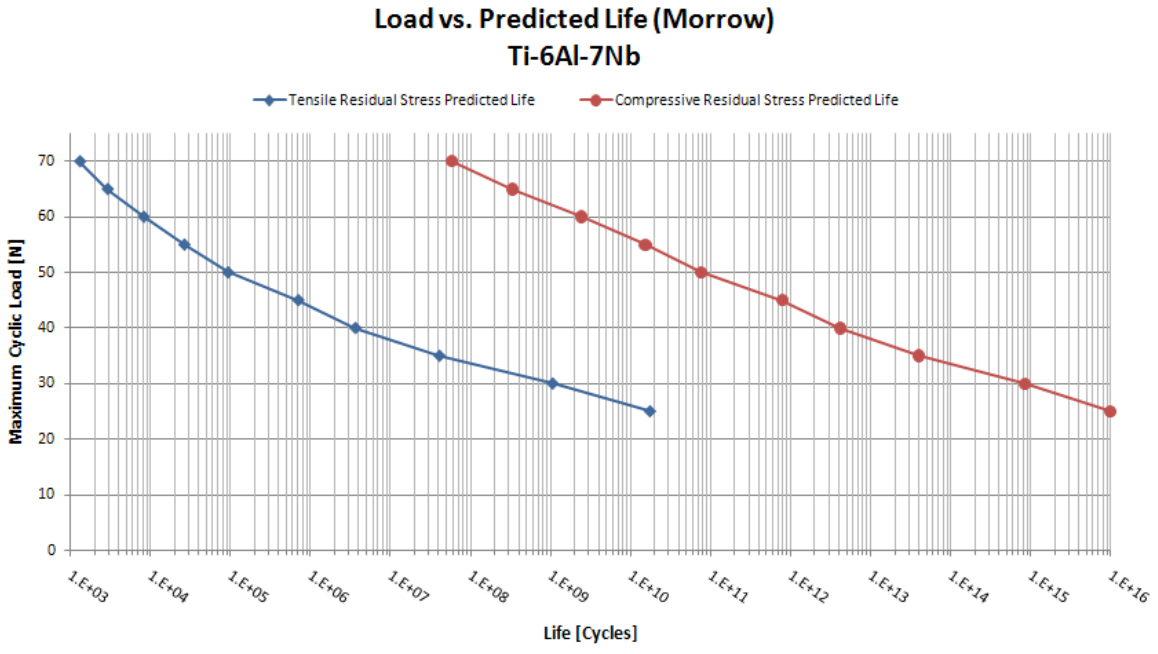

Figure 4. 12 Load vs. predicted life for closed geometry method of manufacture

CHAPTER 5. CONCLUSION

Spinal disc degeneration has been shown to be an increasing issue with large societal and monetary impacts. The potential to provide improvement to the medical devices used to treat the multitudes of people suffering from this aliment are vast. This study chose to evaluate the fatigue behavior of a spinal implant design. The StenoFix implant is dependent on wings being deformed and pressed into the spinal processes surrounding a damaged disc region. The initial installation results in permanent plastic deformation that imparts residual tensile stress which degrades fatigue behavior.

Dedicated test specimens were fabricated from two titanium alloys, Ti-6Al-7Nb and Ti-15Mo, to allow the region of the implant that witnessed the plastic deformation to be mechanically tested. The specimens were initially deformed to a set distance and then allowed to return to equilibrium. Each specimen was cycled in a force controlled manner until failure or run out of 5 million cycles occurred. The physical testing displayed the superior fatigue performance of Ti-6Al-7Nb when compared to Ti-15Mo. Also witnessed by the physical testing was the process of cyclic hardening of both materials during the initial stages of fatigue loading. It was shown that if loading parameters are permitted to be initiated at a reduced level the materials cyclic harden and fatigue performance is increased.

Computational methods were carried out to determine the motion and internal stresses and strains of the implant wing. Simulations were conducted to evaluate the stresses induced during plastic deformation, the effect of varying material property definition values, the effect of modifying the loading point, and three modifications to the

initial geometry. From these studies it can be seen that the stress levels imparted to the implant during plastic deformation are significant, material definition plays a large role in characterizing internal stress fields, varying the load line impacts both motion and field quantity values, and there is possible room for improvement to the original design by altering the geometry. The simulation strain values in addition to parameters from literature were used in conjunction with the Morrow Strain Life model to predict design life.

The concept of developing multiple clamping widths for this implant would be worth investigating. By tailoring the implant to a patient the initial deflection distance could be reduced thereby improving the fatigue performance. Modifying the geometry of the failure surface to match that of simulation New Geometry 2 of New Geometry 3 shows an area for improvement that would need to be validated with mechanical testing. This modification would allow the rate of change of curvature to be continuous and eradicate a stress concentration shown to be centrally located to the initiation of fatigue failures. Further development of material properties used in the computational modeling would provide increased accuracy leading to the enhanced development of hardware before physical testing was to commence. Constricting the operator dependency for specimen load location during physical testing by means of a lead screw fixture design would result in a more accurate and repeatable location of the wing moment arm. This would eliminate a variable proven to have heavy impact on the determination of predicted motion and stress field values. Finally, the concept of altering the manufactured geometry to a configuration where the wings are closed and then pulled

apart during installation shows great promise for increasing fatigue life and is worthy of future investigation.

BIBLIOGRAPHY

ABAQUS. *ABAQUS Analysis User's Manual.* Providence, RI: Simulia, 2010.

Albert, W. A. J. "Uber Treibseile am Harz.Archiv fur Mineralogie, Georgnosie." *Bergbau und Huttenkunde* 10 (1837): 215-234.

Andersson, GB. "Epidemiological features of chronic low back pain." *Lancet* 354 (1999): 581-585.

Apfel, Christian C, et al. "Restoration of disk height through non-surgical spinal decompression is associated with decreased discogenic low back pain: a retrospective cohort study." *BMC Musculoskeletal Disorders* 11, no. 155 (2010).

Arata, J.J., W.A. Kumar, W.A. Curtin, and A. Needleman. "Crack growth in lamellar titanium aluminide." *International Journal of Fracture* 111 (2001): 163-189.

Ashby, Michael F., and David R.H. Jones. *Engineering Materials 1 An Introduction to Properties, Applications and Design.* 3rd Ed. Burlington: Butterworth-Heinemann, 2005.

ASTM E 646. *Tensile Strain Hardening of Metallic Sheet Materials.* West Conshohocken: American Society for Testing and Materials, 1998.

ASTM F 1295. *Standard Specification for Wrought Titanium-6Aluminum-7Niobium Alloy for Surgical Implant Applications.* West Conshohocken: American Society for Testing and Materials, 2005.

ASTM F 1717. *Standard Test Methods for Spinal Implant Constructs in a Vertebrectomy Model.* Philadelphia: American Society for Testing and Materials, 2004.

ASTM F 2066. *Standard Specification for Wrought Titanium-15 Molybdenum Alloy for Surgical Implant Applications.* West Conshohocken: American Society of Testing and Materials, 2007.

Bannantine, Julie A., Jess J. Comer, and James L. Handrock. *FUNDAMENTALS OF METAL FATIGUE ANALYSIS.* Englewood Cliffs: Prentice Hall, 1990.

Barlow, J. "More on Optimal Stress Points-Reduced Integration, Element Distortions and Error Estimation." *International Journal for Numerical Methods in Engineering* 28, no. 7 (1989): 1487-1504.

Barlow, J. "Optimal Stress Locations in Finite Element Models." *International Journal for Numerical Methods in Engineering* 10, no. 2 (1977): 604.

Bicanic, N., and E. Hinton. "Spurious Modes in Two-Dimensional Isoparametric Elements." *International Journal for Numerical Methods in Engineering* 14, no. 10 (1979): 1545-1557.

Chen, Yu-yong, Li-juan XU, Zhi-guang Liu, Fan-tao Kong, and Zi-young Chen. "Microstructures and properties of titanium alloys Ti-Mo for dental use." *Transactions of Nonferrous Metals Society of China* 16 (2006): 824-828.

Cook, Robert D., David S. Malkus, Michael E. Plesha, and Robert J. Witt. *Concepts And Applications Of Finite Element Analysis.* 4th ED. Hoboken: John Wiley & Sons, Inc., 2002.

Dorf, Richard C., and Robert H. Bishop. *Modern Control Systems.* Upper Saddle River: Pearson Prentice Hall, 2008.

Geetha, M., A. K. Singh, R. Asokamani, and A. K. Gogia. "Ti based biomaterials, the ultimate choice for orthopaedic implants - A review." *Progress in Materials Science*, 2009: 397-425.

Leinenbach, Christian, and Dietmar Eifler. "Fatigue and cyclic deformation behaviour of surface-modified titanium alloys in simulated physiological media." *Biomaterials* 27 (2006): 1200-1208.

Liu, W. K., Y. K. Hu, and T. Belytschko. "Multiple Quadrature Underintegrated Finite Elements." *International Journal for Numerical Methods in Engineering* 37, no. 19 (1994): 3263-3289.

Macario, Alex, Charlotte Richmond, Martin Auster, and Joseph V. Pergolizzi. "Treatment of 94 Outpatients With Chronic Discogenic Low Back Pain with the DRX9000: A Retrospective Chart Review." *World Institute of Pain* 8, no. 1 (2008): 11-17.

Mahmoud, A. "Pre-overloading to Extend Fatigue Life of Cast Clasps." *Journal of Dental Research* 86 (2007): 868-872.

MMPDS. *Metallic Materials Properties Development and Standardization.* Washington, D.C.: U.S. Department of Transportation Federal Aviation Administration, 2003.

Norton, Robert L. *MACHINE DESIGN An Integrated Approach.* Third. Upper Saddle River: Pearson Prentice Hall, 2006.

Ramberg, W., and W. R. Osgood. *Description of stress-strain curves by three parameters.* Washington DC: Technical Note No. 902, National Advisory Committee For Aeronautics, 1943.

Saitova, L. R., H. W. Hoppel, M. Goken, I. P. Semenova, and R. Z. Valiev. "Cyclic deformation behavior and fatigue lives of ultrafine-grained Ti-6Al-4V ELI alloy for medical use." *International Journal of Fatigue* 31 (2009): 322-331.

Schijve, J. "Fatigue of Structures and materials in the 20th century and the state of the art." *International Journal of Fatigue* 25 (2003): 679-702.

Schutz, Walter. "A HISTORY OF GATIGUE." *Engineering Fracture Mechanics* 54, no. 2 (1996): 263-300.

Sonsino, C. M. "Fatigue design for powder metallurgy." *Metal Powder Report* 45, no. 11 (1990): 754-764.

Stephens, Ralph I., Ali Fatemi, Robert R. Stephens, and Henry O. Fuchs. *Metal Fatigue in Engineering.* Second. New York: John Wiley & Sons, Inc., 2001.

Taylor, R. L., J. C. Simo, O. C. Zienkiewics, and A. C. H. Chan. "The Patch Test - A Condition for Assessing FEM Convergence." *International Journal for Numerical Methods in Engineering* 22, no. 1 (1986): 39-62.

Tenchev, R. T. "Empirical Way to Improve Stress Accuracy at Stress Concentrations in Finite Element Analysis." *Communications in Numerical Methods in Engineering* 10, no. 7 (1994): 565-576.

Zhang, Yin-gang, Tuan-mao Guo, Xiong Guo, and Shi-xun Wu. "Clinical diagnosis for discogenic low back pain." *International Journal of Biological Sciences* 5, no. 7 (2009): 647-658.

APPENDIX A: TEST FIXTURE DRAWINGS

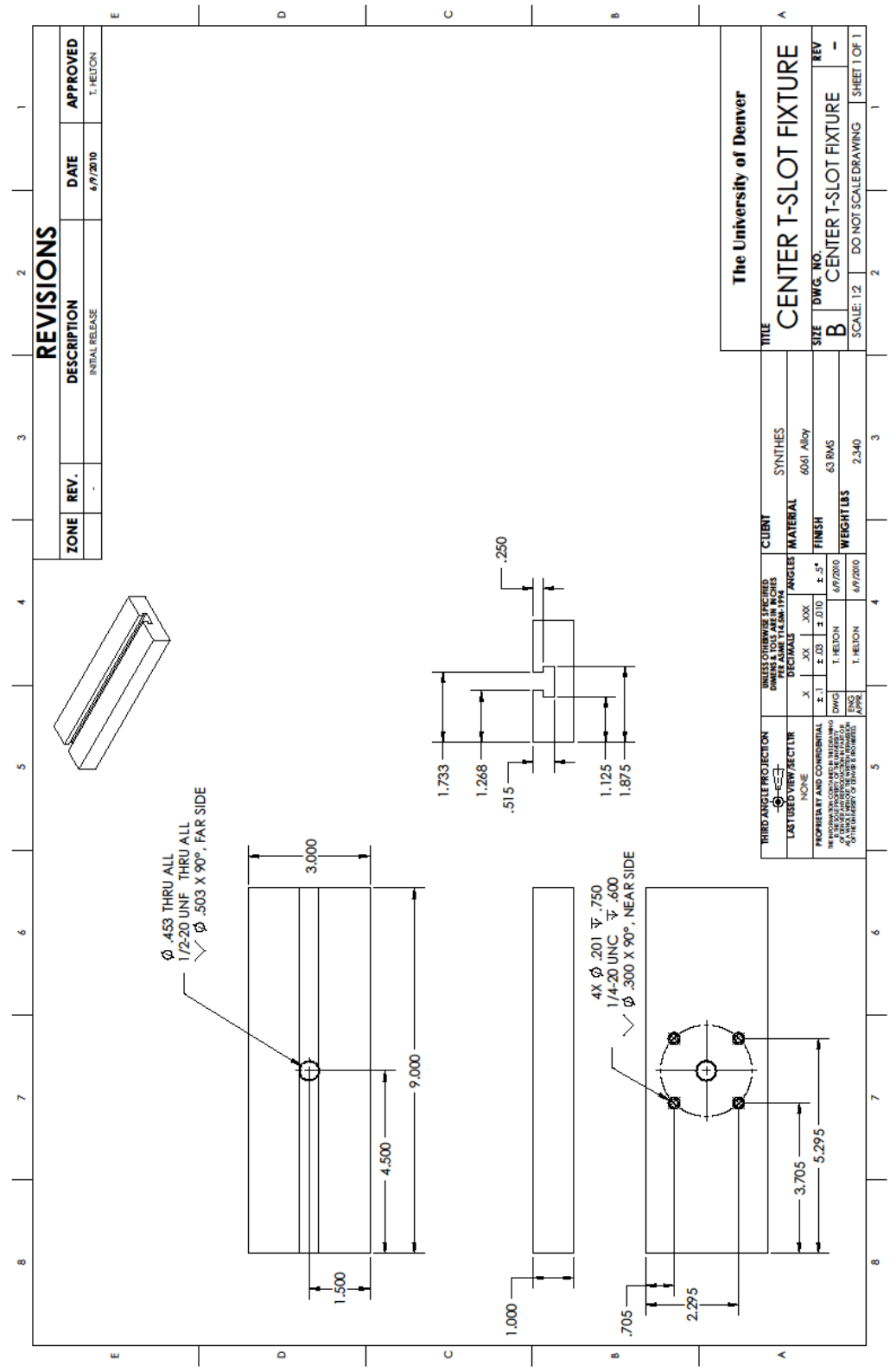

Figure A. 1 Center t-slot fixture drawing

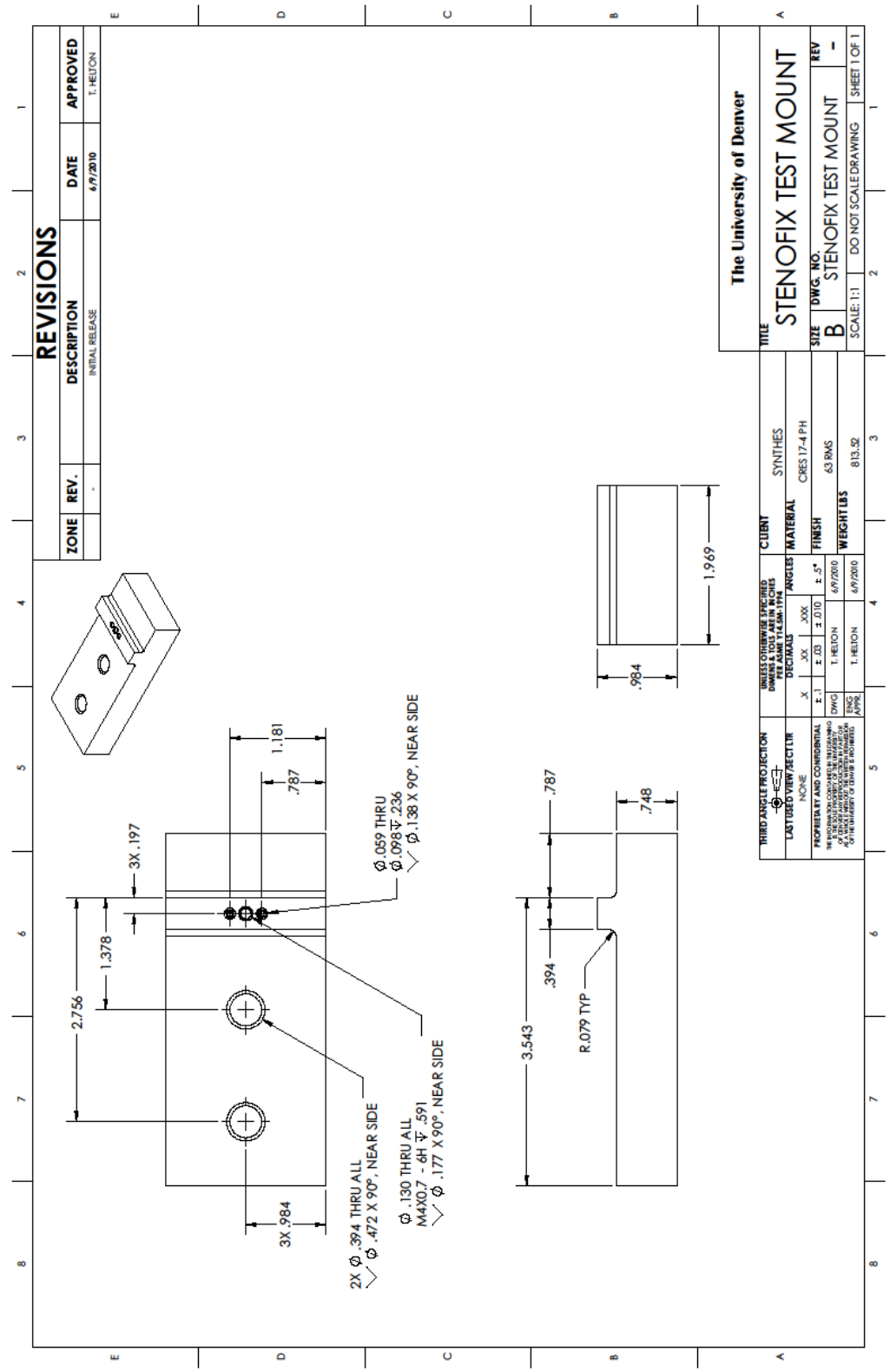

Figure A. 2 StenoFix test mount drawing

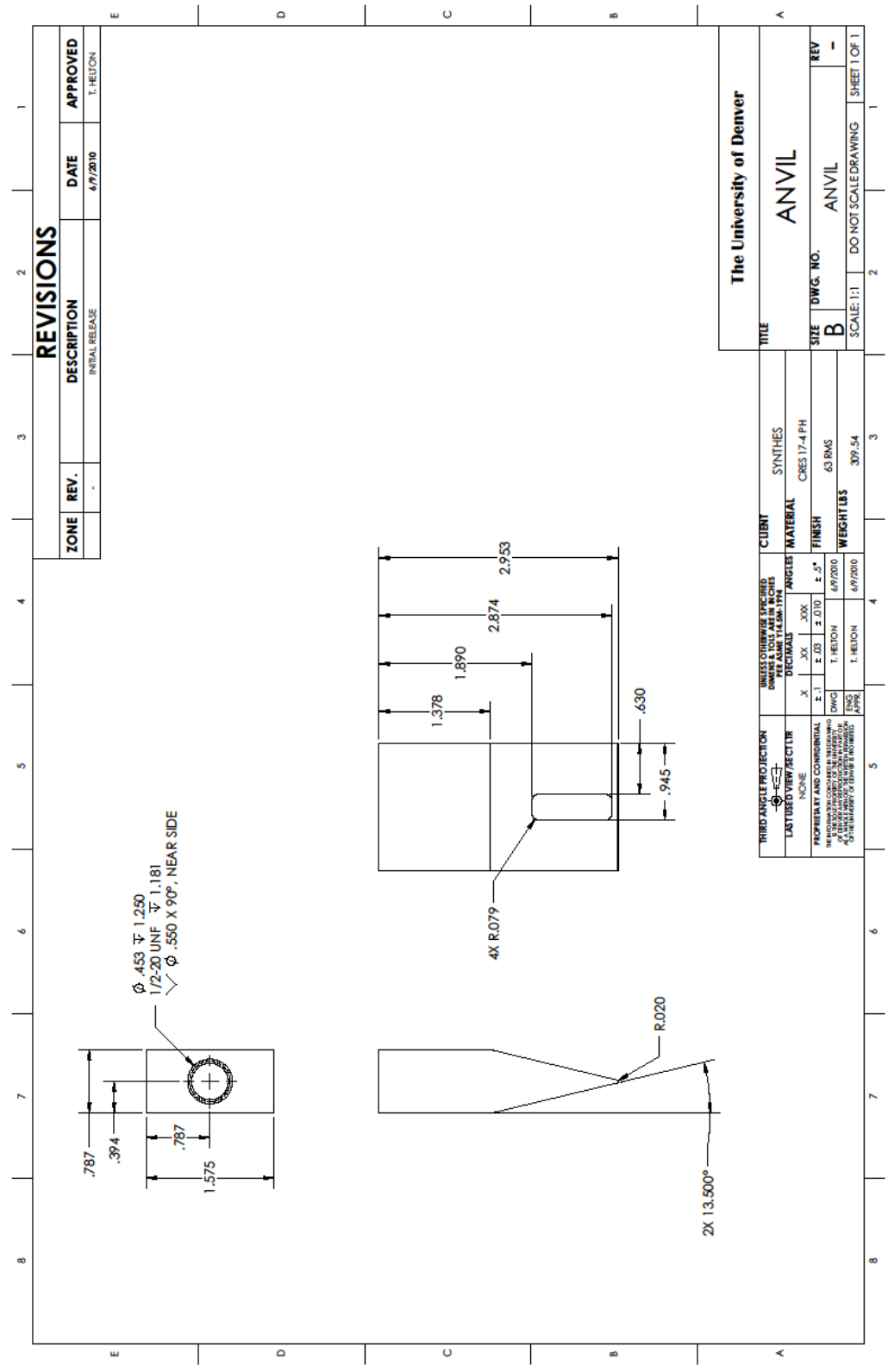

Figure A. 3 Anvil drawing

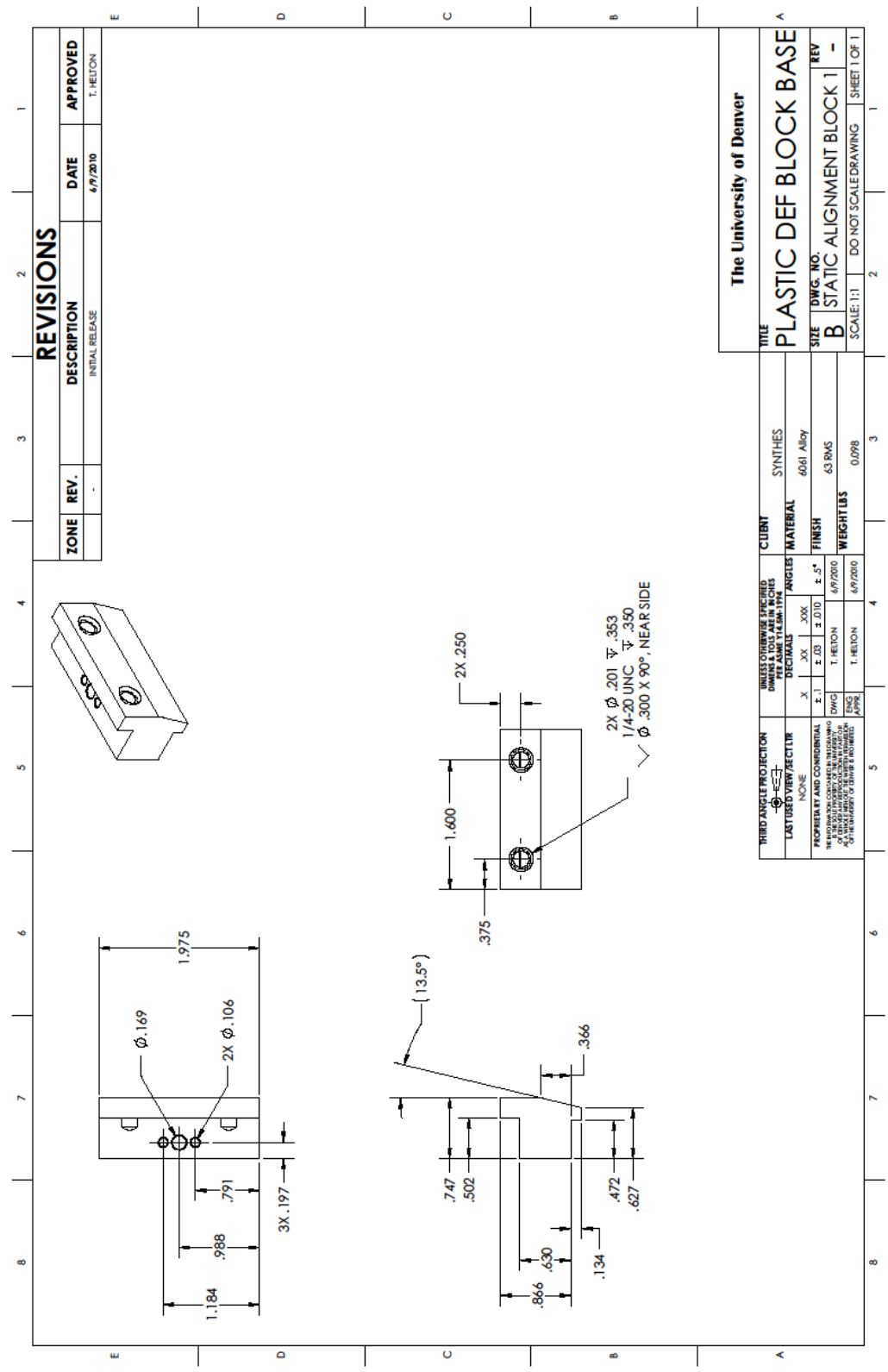

Figure A. 4 Plastic deformation block base drawing

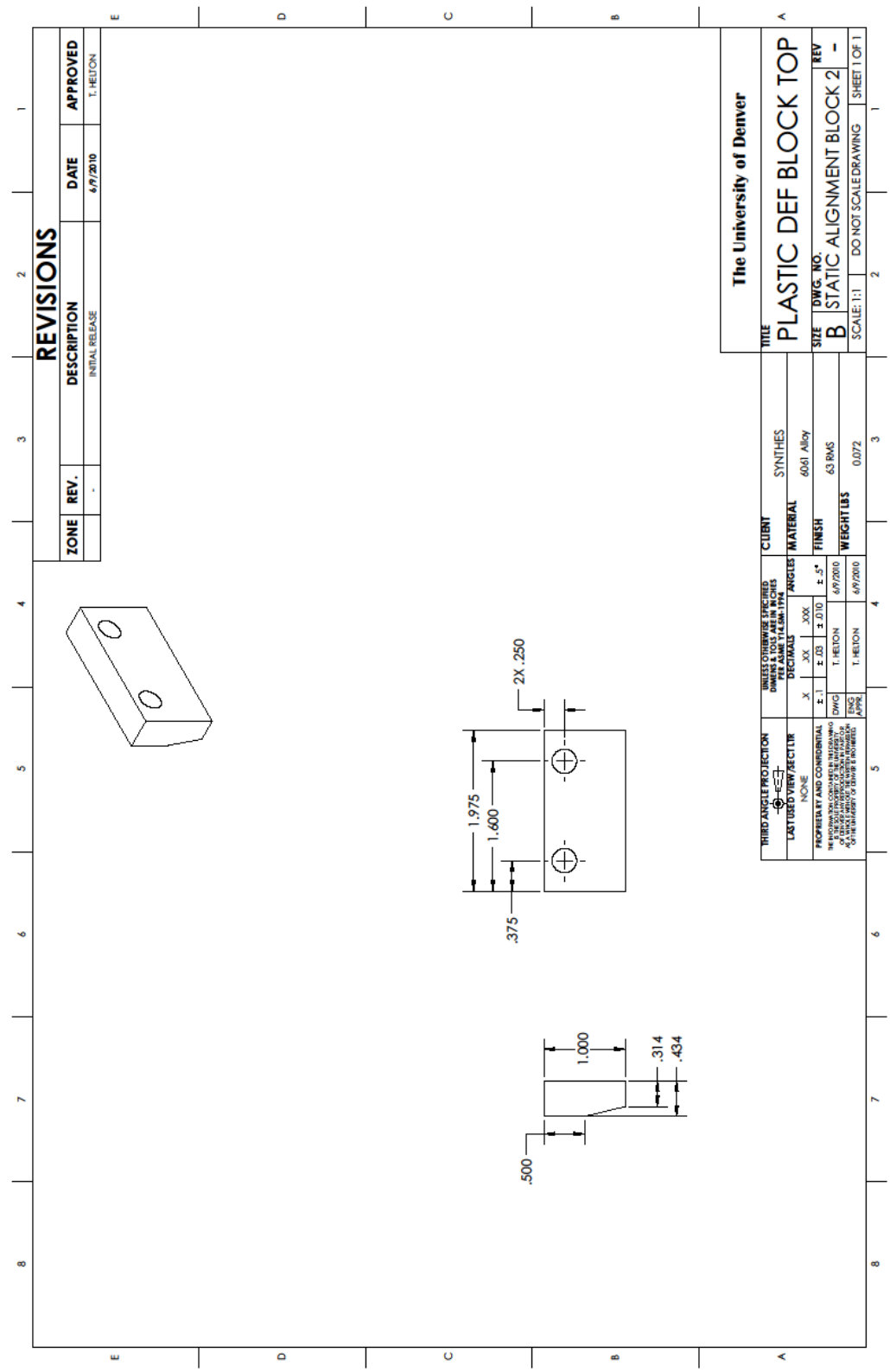

Figure A. 5 Plastic deformation block top drawing

APPENDIX B: SYNTHES TEST LOG

Table B. 1 Synthes plastic deformation force test log Ti-6Al-7Nb specimens

Number	DU Number	Peak Load [N]	Load @ 2% Offset Yield [N]	Load @ Peak Displacement [N]
10-105-07		107.45	91.12	79.81
10-105-07		103.44	87.21	76.16
10-105-07		111.17	92.51	80.02
10-105-07		106.64	89.13	79.59
10-105-08	1-Ti-6Al-7Nb-1	106.18	88.70	76.12
10-105-08	1-Ti-6Al-7Nb-2	110.45	92.25	79.99
10-105-08	1-Ti-6Al-7Nb-3	111.27	93.98	81.98
10-105-08	1-Ti-6Al-7Nb-4	110.19	91.48	80.49
10-105-09	2-Ti-6Al-7Nb-1	103.54	88.09	77.02
10-105-09	2-Ti-6Al-7Nb-2	113.31	94.36	81.69
10-105-09	2-Ti-6Al-7Nb-3	109.29	91.81	80.85
10-105-09	2-Ti-6Al-7Nb-4	110.33	92.73	80.22
Mean		108.60	91.11	79.50
Standard Deviation		3.14	2.32	1.99
Minimum		103.44	87.21	76.12
Maximum		113.31	94.36	81.98

Table B. 2 Plastic deformation displacement test log Ti-6Al-7Nb

Number	DU Number	Displacement @ Peak Load [mm]	Displacement @ 2% Offset Yield [mm]	Deflection @ Return Load Point [mm]
10-105-07		3.423	1.662	3.578
10-105-07		3.391	1.621	3.483
10-105-07		3.522	1.621	3.513
10-105-07		3.451	1.630	3.521
10-105-08	1-Ti-6Al-7Nb-1	3.395	1.614	3.537
10-105-08	1-Ti-6Al-7Nb-2	3.648	1.628	3.548
10-105-08	1-Ti-6Al-7Nb-3	3.507	1.617	3.557
10-105-08	1-Ti-6Al-7Nb-4	3.351	1.591	3.524
10-105-09	2-Ti-6Al-7Nb-1	3.429	1.679	3.536
10-105-09	2-Ti-6Al-7Nb-2	3.518	1.607	3.567
10-105-09	2-Ti-6Al-7Nb-3	3.311	1.611	3.536
10-105-09	2-Ti-6Al-7Nb-4	3.348	1.647	3.533
Mean		3.441	1.627	3.536
Standard Deviation		0.095	0.025	0.025
Minimum		3.311	1.591	3.483
Maximum		3.648	1.679	3.578

Table B. 3 Plastic deformation force test log Ti-16Mo

Number	DU Number	Peak Load [N]	Load @ 2% Offset Yield [N]	Load @ Peak Displacement [N]
10-105-10		120.49	103.52	82.76
10-105-10		119.66	101.89	84.87
10-105-10		112.32	96.01	80.72
10-105-10		108.67	94.45	78.26
10-105-11	1-Ti-15Mo-1	111.60	95.28	81.70
10-105-11	1-Ti-15Mo-2	113.45	99.24	79.63
10-105-11	1-Ti-15Mo-3	122.19	104.14	85.47
10-105-11	1-Ti-15Mo-4	115.74	99.44	81.96
10-105-12	2-Ti-15Mo-1	118.76	102.01	84.44
10-105-12	2-Ti-15Mo-2	118.83	101.80	84.94
10-105-12	2-Ti-15Mo-3	114.25	99.10	82.24
10-105-12	2-Ti-15Mo-4	112.56	97.22	79.98
Mean		115.71	99.51	82.25
Standard Deviation		4.20	3.25	2.34
Minimum		108.67	94.45	78.26
Maximum		122.19	104.14	85.47

Table B. 4 Plastic deformation displacement test log Ti-6Al-7Nb

Number	DU Number	Displacement @ Peak Load [mm]	Displacement @ 2% Offset Yield [mm]	Deflection @ Return Load Point [mm]
10-105-10		3.162	1.871	3.191
10-105-10		3.327	1.906	3.076
10-105-10		3.268	1.828	3.374
10-105-10		3.376	1.856	3.352
10-105-11	1-Ti-15Mo-1	3.228	1.788	3.356
10-105-11	1-Ti-15Mo-2	3.115	1.945	3.242
10-105-11	1-Ti-15Mo-3	3.317	1.877	3.126
10-105-11	1-Ti-15Mo-4	3.267	1.896	3.187
10-105-12	2-Ti-15Mo-1	3.373	1.902	3.226
10-105-12	2-Ti-15Mo-2	3.244	1.893	3.127
10-105-12	2-Ti-15Mo-3	3.234	1.844	3.347
10-105-12	2-Ti-15Mo-4	3.198	1.858	3.273
Mean		3.259	1.872	3.240
Standard Deviation		0.080	0.041	0.102
Minimum		3.115	1.788	3.076
Maximum		3.376	1.945	3.374

Table B. 5 Fatigue test log sample MT10-105-07

Number	Material	Wing	Load [N]	Completed Cycles
MT10-105-07	Ti-6Al-7Nb	1	25	500,000
			30	500,000
			35	500,000
			40	440,000
		2	25	500,000
			30	500,000
			35	500,000
			40	254,339
		3	25	500,000
			30	500,000
			35	500,000
			40	500,000
			45	500,000
			50	117,685
		4	25	500,000
			30	500,000
			35	500,000
			40	500,000
			45	183,846

Table B. 6 Fatigue test log sample MT10-105-10

Number	Material	Wing	Load [N]	Completed Cycles
MT10-105-10	Ti-15Mo	1	25	500,000
			30	500,000
			35	500,000
			40	500,000
			45	500,000
			50	500,000
			55	44,724
		2	25	500,000
			30	500,000
			35	500,000
			40	500,000
			45	500,000
			50	40,136
		4	25	500,000
			30	500,000
			35	500,000
			40	500,000
			45	11,486

Table B. 7 Fatigue test log sample MT10-105-11

Number	Material	Wing	Load [N]	Completed Cycles
MT10-105-11	Ti-15Mo	1	25	500,000
			30	102,655

APPENDIX C: DU TEST LOG

Table C. 1 Fatigue test log sample 1-Ti-6Al-7Nb

Number	Material	Wing	Received Condition	Load [N]	Completed Cycles
1-TAN-1	Ti-6Al-7Nb	1	Deformed		N/A
				50	86,318
1-TAN-2		2	Deformed		N/A
				45	5,000,000
				50	
1-TAN-3		3	Deformed		N/A
				40	3,758,160

Table C. 2 Fatigue test log sample 2-Ti-6Al-7Nb

Number	Material	Wing	Received Condition	Load [N]	Completed Cycles
2-TAN-1	Ti-6Al-7Nb	1	Deformed		N/A
				55	29,616

Table C. 3 Fatigue test log sample 1-Ti-15Mo

Number	Material	Wing	Received Condition	Load [N]	Completed Cycles
1-TiMo-1	Ti-15Mo	1	Deformed		N/A
				25	500,000
				30	102,655
1-TiMo-2		2	Deformed		N/A
				45	37,210
1-TiMo-3		3	Deformed		N/A
				45	39,782
1-TiMo-4		4	Deformed		N/A
				40	114,234

Table C. 4 Fatigue test log sample 2-Ti-15Mo

Number	Material	Wing	Received Condition	Load [N]	Completed Cycles
2-TiMo-2	Ti-15Mo	2	Deformed		N/A
				50	23,323
2-TiMo-3		3	Deformed		N/A
				35	2,265,003
				40	5,000,000
				45	5,000,000
				50	5,000,000
				55	29,293

Table C. 5 Fatigue test log sample 3-Ti-15Mo

Number	Material	Wing	Received Condition	Load [N]	Completed Cycles
3-TiMo-2	Ti-15Mo	2	Deformed		N/A
				50	27,910

APPENDIX D: STIFFNESS TABLES

Table D. 1 Stiffness tables for sample 1-Ti-6Al-7Nb-1

Cycle	Stiffness
1	80.730
10	81.872
100	81.482
1000	81.248
2000	81.643
3000	81.627
4000	78.961
5000	77.859
6000	78.019
7000	78.002
8000	77.960

Cycle	Stiffness
9000	77.865
10000	77.841
20000	77.583
30000	77.598
40000	77.535
50000	77.512
60000	77.223
70000	76.126
80000	72.953

Table D. 2 Stiffness tables for sample 1-Ti-6Al-7Nb-2-a

Cycle	Stiffness
1	79.244
10	77.830
100	80.240
1000	80.421
2000	80.505
3000	80.545
4000	80.557
5000	80.572
6000	80.600
7000	80.636
8000	80.639

Cycle	Stiffness
9000	80.653
10000	80.675
20000	80.687
30000	80.723
40000	80.786
50000	80.713
60000	80.746
70000	80.820
80000	80.818
90000	80.806
100000	80.878

Cycle	Stiffness
150000	80.910
200000	80.902
250000	80.828
500000	80.684
750000	80.739
1000000	80.650
1250000	80.611
1500000	80.635
1750000	80.435
2000000	80.599
2250000	80.505

Cycle	Stiffness
2500000	80.580
2750000	80.504
3000000	80.415
3250000	80.500
3500000	80.389
3750000	80.478
4000000	80.005
4250000	80.037
4500000	80.047
4750000	79.934
5000000	80.074

Table D. 3 Stiffness tables for sample 1-Ti-6Al-7Nb-3

Cycle	Stiffness
1	83.577
10	87.482
100	86.778
1000	93.900
2000	93.642
3000	93.431
4000	93.283
5000	93.255
6000	93.150
7000	93.102
8000	93.054

Cycle	Stiffness
9000	92.975
10000	92.999
20000	92.653
30000	92.626
40000	92.468
50000	92.499
60000	92.415
70000	92.460
80000	92.407
90000	92.350
100000	92.365

Cycle	Stiffness
150000	92.222
200000	92.279
250000	92.226
500000	91.871
750000	91.749
1000000	91.743
1250000	91.518
1500000	91.520
1750000	91.349
2000000	91.419
2250000	91.342

Cycle	Stiffness
2500000	91.342
2750000	91.298
3000000	91.236
3250000	91.370
3500000	91.315
3750000	84.494

Table D. 4 Stiffness tables for sample 2-Ti-6Al-7Nb-1

Cycle	Stiffness
1	75.475
10	78.042
100	76.884
1000	77.117
2000	77.203
3000	77.264
4000	77.310
5000	77.429
6000	77.371
7000	77.469
8000	77.499

Cycle	Stiffness
9000	77.503
10000	77.514
20000	77.436

Table D. 5 Stiffness tables for sample 1-Ti-15Mo-2

Cycle	Stiffness
1	73.420
10	73.967
100	73.996
1000	70.584
2000	70.402
3000	70.283
4000	70.223
5000	70.264
6000	70.226
7000	70.233
8000	70.186

Cycle	Stiffness
9000	70.184
10000	70.142
20000	69.904
30000	67.092

Table D. 6 Stiffness tables for sample 1-Ti-15Mo-3

Cycle	Stiffness
1	72.487
10	74.748
100	74.920
1000	73.450
2000	73.368
3000	73.310
4000	73.243
5000	73.182
6000	73.145
7000	73.118
8000	73.110

Cycle	Stiffness
9000	73.057
10000	73.064
20000	72.828
30000	70.758

Table D. 7 Stiffness tables for sample 1-Ti-15Mo-4

Cycle	Stiffness
1	78.309
10	78.013
100	78.344
1000	78.115
2000	77.543
3000	77.145
4000	74.161
5000	74.183
6000	74.055
7000	74.160
8000	74.134

Cycle	Stiffness
9000	74.052
10000	74.044
20000	74.988
30000	74.568
40000	75.161
50000	75.474
60000	76.519
70000	78.022
80000	77.848
90000	77.551
100000	75.793

Table D. 8 Stiffness tables for sample 2-Ti-15Mo-2

Cycle	Stiffness
1	69.293
10	72.667
100	72.542
1000	70.592
2000	69.946
3000	69.895
4000	69.931
5000	69.857
6000	69.839
7000	69.825
8000	69.808

Cycle	Stiffness
9000	69.759
10000	69.761
20000	64.850

Table D. 9 Stiffness tables for sample 2-Ti-15Mo-3-a

Cycle	Stiffness
1	78.094
10	78.565
100	78.475
1000	79.369
2000	79.795
3000	79.805
4000	79.693
5000	80.446
6000	81.488
7000	82.818
8000	83.789

Cycle	Stiffness
9000	84.072
10000	84.196
20000	84.906
30000	85.046
40000	84.940
50000	84.999
60000	85.021
70000	84.998
80000	85.014
90000	84.958
100000	85.039

Cycle	Stiffness
150000	86.413
200000	86.421
250000	86.576
500000	86.309
750000	86.186
1000000	86.721
1250000	86.722
1500000	86.580
1750000	86.616
2000000	86.744
2250000	87.153

Table D. 10 Stiffness tables for sample 2-Ti-15Mo-3-b

Cycle	Stiffness
1	78.697
10	75.841
100	77.786
1000	76.932
2000	76.970
3000	77.259
4000	77.173
5000	77.127
6000	77.103
7000	77.126
8000	77.048

Cycle	Stiffness
9000	77.140
10000	77.293
20000	77.245
30000	76.387
40000	76.620
50000	76.812
60000	76.892
70000	76.656
80000	76.830
90000	76.599
100000	76.733

Cycle	Stiffness
150000	76.684
200000	76.330
250000	76.114
500000	76.701
750000	76.858
1000000	76.804
1250000	76.936
1500000	76.854
1750000	76.725
2000000	76.743
2250000	76.427

Cycle	Stiffness
2500000	76.781
2750000	76.586
3000000	77.044
3250000	76.361
3500000	76.578
3750000	76.803
4000000	76.787
4250000	77.256
4500000	77.101
4750000	77.021
5000000	77.101

Table D. 11 Stiffness tables for sample 2-Ti-15Mo-3-c

Cycle	Stiffness	Cycle	Stiffness	Cycle	Stiffness	Cycle	Stiffness
1	77.679	9000	77.341	150000	77.365	2500000	76.299
10	78.705	10000	77.326	200000	77.346	2750000	76.347
100	78.347	20000	77.352	250000	77.324	3000000	76.111
1000	77.596	30000	77.308	500000	77.339	3250000	76.414
2000	77.766	40000	77.204	750000	77.033	3500000	76.343
3000	77.320	50000	77.247	1000000	76.546	3750000	76.094
4000	77.344	60000	77.159	1250000	76.632	4000000	76.206
5000	77.334	70000	77.290	1500000	76.624	4250000	75.986
6000	77.174	80000	77.045	1750000	76.659	4500000	76.204
7000	77.189	90000	77.109	2000000	76.493	4750000	75.918
8000	77.197	100000	77.228	2250000	76.363	5000000	75.979

Table D. 12 Stiffness tables for sample 2-Ti-15Mo-3-d

Cycle	Stiffness	Cycle	Stiffness	Cycle	Stiffness	Cycle	Stiffness
1	76.616	9000	74.441	150000	73.590	2500000	73.524
10	73.893	10000	74.095	200000	73.428	2750000	73.384
100	74.330	20000	74.341	250000	73.342	3000000	73.606
1000	74.149	30000	74.965	500000	73.513	3250000	73.515
2000	73.814	40000	74.459	750000	73.522	3500000	73.385
3000	73.614	50000	74.545	1000000	73.633	3750000	73.281
4000	72.889	60000	74.216	1250000	73.608	4000000	73.380
5000	73.342	70000	74.301	1500000	73.631	4250000	73.567
6000	73.485	80000	73.918	1750000	73.600	4500000	73.407
7000	73.864	90000	73.832	2000000	73.586	4750000	73.482
8000	73.782	100000	73.669	2250000	73.559	5000000	73.549

Table D. 13 Stiffness tables for sample 2-Ti-15Mo-3-e

Cycle	Stiffness
1	77.841
10	73.602
100	73.922
1000	74.500
2000	74.276
3000	74.354
4000	74.273
5000	74.088
6000	74.454
7000	74.210
8000	74.248

Cycle	Stiffness
9000	74.149
10000	74.176
20000	73.692

Table D. 14 Stiffness tables for sample 3-Ti-15Mo-2

Cycle	Stiffness
1	69.702
10	75.747
100	75.685
1000	72.720
2000	72.708
3000	72.649
4000	72.606
5000	72.618
6000	72.589
7000	72.575
8000	72.539

Cycle	Stiffness
9000	72.521
10000	72.503
20000	70.510

APPENDIX E: COMPUTATIONAL STRESS AND STRAIN RESULTS

Table E. 1 Predicted stress results for material property variation simulations

Simulation MATERIAL PROPERTY VARIATION	σ_{min} [MPa]	σ_{max} [MPa]	Mean Stress [MPa]
-10% Sinusoidal 5.0 - 50 [N]	628.70	1031.0	829.9
Nominal Sinusoidal 5.0 - 50 [N]	637.10	1093.0	865.1
+10% Sinusoidal 5.0 - 50 [N]	593.40	1092.0	842.7

Table E. 2 Predicted strain results for material property variation simulations

Simulation MATERIAL PROPERTY VARIATION	ε_{min} [ ]	ε_{max} [ ]	ε_a [ ]
-10% Sinusoidal 5.0 - 50 [N]	-6.6476E-02	-6.2635E-02	1.9205E-03
Nominal Sinusoidal 5.0 - 50 [N]	-6.1681E-02	-5.7323E-02	2.1790E-03
+10% Sinusoidal 5.0 - 50 [N]	-5.6695E-02	-5.1950E-02	2.3725E-03

Table E. 3 Predicted stress results for load line variation simulations

Simulation LOAD LINE VARIATION	σ_{min} [MPa]	σ_{max} [MPa]	Mean Stress [MPa]
-1.0 [mm] Sinusoidal 5.0 - 50 [N]	628.70	1031.0	829.9
-0.5 [mm] Sinusoidal 5.0 - 50 [N]	637.10	1093.0	865.1
-0.1 [mm] Sinusoidal 5.0 - 50 [N]	593.40	1092.0	842.7
+0.1 [mm] Sinusoidal 5.0 - 50 [N]	570.90	1089.0	830.0

Table E. 4 Predicted strain results for load line variation simulations

Simulation LOAD LINE VARIATION	ε_{min} [ ]	ε_{max} [ ]	ε_a [ ]
-1.0 [mm] Sinusoidal 5.0 - 50 [N]	-6.6476E-02	-6.2635E-02	1.9205E-03
-0.5 [mm] Sinusoidal 5.0 - 50 [N]	-6.1681E-02	-5.7323E-02	2.1790E-03
-0.1 [mm] Sinusoidal 5.0 - 50 [N]	-5.6695E-02	-5.1950E-02	2.3725E-03
+0.1 [mm] Sinusoidal 5.0 - 50 [N]	-5.4147E-02	-4.9216E-02	2.4655E-03

Table E. 5 Predicted stress results for force control simulations

Simulation	σ_{min}	σ_{max}	Mean Stress
FORCE CONTROL	**[MPa]**	**[MPa]**	**[MPa]**
Sinusoidal 5.0 - 50 [N]	580.50	1090.0	835.3

Table E. 6 Predicted strain results for force control simulations

Simulation	ε_{min}	ε_{max}	ε_a
FORCE CONTROL	**[ ]**	**[ ]**	**[ ]**
Sinusoidal 5.0 - 50 [N]	-5.4686E-02	-4.9838E-02	2.4240E-03

Table E. 7 Predicted stress results for original geometry simulations

Simulation	σ_{min}	σ_{max}	Mean Stress
ORIGINAL GEOMETRY	**[MPa]**	**[MPa]**	**[MPa]**
Sinusoidal 2.5 - 25 [N]	601.10	847.3	724.2
Sinusoidal 3.0 - 30 [N]	606.80	904.1	755.5
Sinusoidal 3.5 - 35 [N]	613.20	962.1	787.7
Sinusoidal 4.0 - 40 [N]	620.50	1022.0	821.3
Sinusoidal 4.5 - 45 [N]	628.50	1083.0	855.8
Sinusoidal 5.0 - 50 [N]	582.10	1091.0	836.6
Sinusoidal 5.5 - 55 [N]	527.30	1091.0	809.2
Sinusoidal 6.0 - 60 [N]	472.50	1092.0	782.3
Sinusoidal 6.5 - 65 [N]	417.10	1093.0	755.1
Sinusoidal 7.0 - 70 [N]	360.80	1094.0	727.4

Table E. 8 Predicted strain results for original geometry simulations

Simulation ORIGINAL GEOMETRY	ε_{min} [ ]	ε_{max} [ ]	ε_{a} [ ]
Sinusoidal 2.5 - 25 [N]	-5.5921E-02	-5.3547E-02	1.1870E-03
Sinusoidal 3.0 - 30 [N]	-5.5866E-02	-5.3007E-02	1.4295E-03
Sinusoidal 3.5 - 35 [N]	-5.5804E-02	-5.2458E-02	1.6730E-03
Sinusoidal 4.0 - 40 [N]	-5.5735E-02	-5.1892E-02	1.9215E-03
Sinusoidal 4.5 - 45 [N]	-5.5661E-02	-5.1322E-02	2.1695E-03
Sinusoidal 5.0 - 50 [N]	-5.5422E-02	-5.0584E-02	2.4190E-03
Sinusoidal 5.5 - 55 [N]	-5.5185E-02	-4.9838E-02	2.6735E-03
Sinusoidal 6.0 - 60 [N]	-5.4890E-02	-4.9036E-02	2.9270E-03
Sinusoidal 6.5 - 65 [N]	-5.4530E-02	-4.8164E-02	3.1830E-03
Sinusoidal 7.0 - 70 [N]	-5.4109E-02	-4.7227E-02	3.4410E-03

Table E. 9 Predicted stress results for no plastic deformation simulations

Simulation NO PLASTIC DEFORMATION	σ_{min} [MPa]	σ_{max} [MPa]	Mean Stress [MPa]
Sinusoidal 2.5 - 25 [N]	28.22	281.7	155.0
Sinusoidal 3.0 - 30 [N]	33.81	337.3	185.6
Sinusoidal 3.5 - 35 [N]	39.39	392.7	216.0
Sinusoidal 4.0 - 40 [N]	45.01	448.4	246.7
Sinusoidal 4.5 - 45 [N]	50.57	503.4	277.0
Sinusoidal 5.0 - 50 [N]	56.13	558.2	307.2
Sinusoidal 5.5 - 55 [N]	61.73	613.3	337.5
Sinusoidal 6.0 - 60 [N]	67.27	667.6	367.4
Sinusoidal 6.5 - 65 [N]	72.85	721.7	397.3
Sinusoidal 7.0 - 70 [N]	80.28	777.4	428.8

Table E. 10 Predicted strain results for no plastic deformation simulations

Simulation NO PLASTIC DEFORMATION	ε_{min} [ ]	ε_{max} [ ]	ε_{a} [ ]
Sinusoidal 2.5 - 25 [N]	2.6152E-04	2.6111E-03	1.1748E-03
Sinusoidal 3.0 - 30 [N]	3.1330E-04	3.1263E-03	1.4065E-03
Sinusoidal 3.5 - 35 [N]	3.6497E-04	3.6397E-03	1.6374E-03
Sinusoidal 4.0 - 40 [N]	4.1708E-04	4.1565E-03	1.8697E-03
Sinusoidal 4.5 - 45 [N]	4.6854E-04	4.6659E-03	2.0987E-03
Sinusoidal 5.0 - 50 [N]	5.2006E-04	5.1739E-03	2.3269E-03
Sinusoidal 5.5 - 55 [N]	5.7193E-04	5.6846E-03	2.5563E-03
Sinusoidal 6.0 - 60 [N]	6.2317E-04	6.1877E-03	2.7823E-03
Sinusoidal 6.5 - 65 [N]	6.7488E-04	6.6890E-03	3.0071E-03
Sinusoidal 7.0 - 70 [N]	7.4340E-04	7.2043E-03	3.2305E-03

Table E. 11 Predicted stress results for new geometry 1 simulations

Simulation NEW GEOMETRY 1	σ_{min} [MPa]	σ_{max} [MPa]	Mean Stress [MPa]
Sinusoidal 2.5 - 25 [N]	444.40	646.9	545.7
Sinusoidal 3.0 - 30 [N]	448.80	693.0	570.9
Sinusoidal 3.5 - 35 [N]	453.40	739.7	596.6
Sinusoidal 4.0 - 40 [N]	458.40	787.4	622.9
Sinusoidal 4.5 - 45 [N]	463.40	835.0	649.2
Sinusoidal 5.0 - 50 [N]	468.50	882.7	675.6
Sinusoidal 5.5 - 55 [N]	474.00	931.5	702.8
Sinusoidal 6.0 - 60 [N]	480.30	980.6	730.5
Sinusoidal 6.5 - 65 [N]	484.50	1027.0	755.8
Sinusoidal 7.0 - 70 [N]	460.10	1048.0	754.1

Table E. 12 Predicted strain results for new geometry 1 simulations

Simulation NEW GEOMETRY 1	ε_{min} [ ]	ε_{max} [ ]	ε_{a} [ ]
Sinusoidal 2.5 - 25 [N]	-2.8777E-02	-2.6833E-02	9.7200E-04
Sinusoidal 3.0 - 30 [N]	-2.8734E-02	-2.6396E-02	1.1690E-03
Sinusoidal 3.5 - 35 [N]	-2.8690E-02	-2.5956E-02	1.3670E-03
Sinusoidal 4.0 - 40 [N]	-2.8644E-02	-2.5507E-02	1.5685E-03
Sinusoidal 4.5 - 45 [N]	-2.8600E+00	-2.5063E-02	1.4175E+00
Sinusoidal 5.0 - 50 [N]	-2.8651E-02	-2.4621E-02	2.0150E-03
Sinusoidal 5.5 - 55 [N]	-2.8521E-02	-2.4172E-02	2.1745E-03
Sinusoidal 6.0 - 60 [N]	-2.8478E-02	-2.3721E-02	2.3785E-03
Sinusoidal 6.5 - 65 [N]	-2.8461E-02	-2.3295E-02	2.5830E-03
Sinusoidal 7.0 - 70 [N]	-2.8242E-02	-2.2630E-02	2.8060E-03

Table E. 13 Predicted stress results for new geometry 2 simulations

Simulation NEW GEOMETRY 2	σ_{min} [MPa]	σ_{max} [MPa]	Mean Stress [MPa]
Sinusoidal 2.5 - 25 [N]	562.80	802.2	682.5
Sinusoidal 3.0 - 30 [N]	568.20	857.1	712.7
Sinusoidal 3.5 - 35 [N]	574.20	913.1	743.7
Sinusoidal 4.0 - 40 [N]	581.00	971.0	776.0
Sinusoidal 4.5 - 45 [N]	586.80	1028.0	807.4
Sinusoidal 5.0 - 50 [N]	586.20	1078.0	832.1
Sinusoidal 5.5 - 55 [N]	536.00	1081.0	808.5
Sinusoidal 6.0 - 60 [N]	483.00	1082.0	782.5
Sinusoidal 6.5 - 65 [N]	429.50	1083.0	756.3
Sinusoidal 7.0 - 70 [N]	375.40	1084.0	729.7

Table E. 14 Predicted strain results for new geometry 2 simulations

Simulation NEW GEOMETRY 2	ε_{min} [ ]	ε_{max} [ ]	ε_{a} [ ]
Sinusoidal 2.5 - 25 [N]	-4.7371E-02	-4.5068E-02	1.1515E-03
Sinusoidal 3.0 - 30 [N]	-4.7319E-02	-4.4547E-02	1.3860E-03
Sinusoidal 3.5 - 35 [N]	-4.7262E-02	-4.4018E-02	1.6220E-03
Sinusoidal 4.0 - 40 [N]	-4.7198E-02	-4.3472E-02	1.8630E-03
Sinusoidal 4.5 - 45 [N]	-4.7146E-02	-4.2941E-02	2.1025E-03
Sinusoidal 5.0 - 50 [N]	-4.7173E-02	-4.2486E-02	2.3435E-03
Sinusoidal 5.5 - 55 [N]	-4.6844E-02	-4.1666E-02	2.5890E-03
Sinusoidal 6.0 - 60 [N]	-4.6575E-02	-4.0907E-02	2.8340E-03
Sinusoidal 6.5 - 65 [N]	-4.6256E-02	-4.0095E-02	3.0805E-03
Sinusoidal 7.0 - 70 [N]	-4.5880E-02	-3.9222E-02	3.3290E-03

Table E. 15 Predicted stress results for new geometry 3 simulations

Simulation NEW GEOMETRY 3	σ_{min} [MPa]	σ_{max} [MPa]	Mean Stress [MPa]
Sinusoidal 2.5 - 25 [N]	634.40	865.0	749.7
Sinusoidal 3.0 - 30 [N]	639.60	918.3	779.0
Sinusoidal 3.5 - 35 [N]	645.30	972.8	809.1
Sinusoidal 4.0 - 40 [N]	652.00	1029.0	840.5
Sinusoidal 4.5 - 45 [N]	657.10	1084.0	870.6
Sinusoidal 5.0 - 50 [N]	622.20	1100.0	861.1
Sinusoidal 5.5 - 55 [N]	569.60	1101.0	835.3
Sinusoidal 6.0 - 60 [N]	517.10	1102.0	809.6
Sinusoidal 6.5 - 65 [N]	464.00	1103.0	783.5
Sinusoidal 7.0 - 70 [N]	409.80	1103.0	756.4

Table E. 16 Predicted strain results for new geometry 3 simulations

Simulation NEW GEOMETRY 3	ε_{min} [ ]	ε_{max} [ ]	ε_a [ ]
Sinusoidal 2.5 - 25 [N]	-6.4237E-02	-6.1934E-02	1.1515E-03
Sinusoidal 3.0 - 30 [N]	-6.4185E-02	-6.1414E-02	1.3855E-03
Sinusoidal 3.5 - 35 [N]	-6.4129E-02	-6.0886E-02	1.6215E-03
Sinusoidal 4.0 - 40 [N]	-6.4064E-02	-6.0342E-02	1.8610E-03
Sinusoidal 4.5 - 45 [N]	-6.4019E-02	-5.9821E-02	2.0990E-03
Sinusoidal 5.0 - 50 [N]	-6.3804E-02	-5.9127E-02	2.3385E-03
Sinusoidal 5.5 - 55 [N]	-6.3522E-02	-5.8358E-02	2.5820E-03
Sinusoidal 6.0 - 60 [N]	-6.3227E-02	-5.7578E-02	2.8245E-03
Sinusoidal 6.5 - 65 [N]	-6.2876E-02	-5.6738E-02	3.0690E-03
Sinusoidal 7.0 - 70 [N]	-6.2455E-02	-5.5824E-02	3.3155E-03

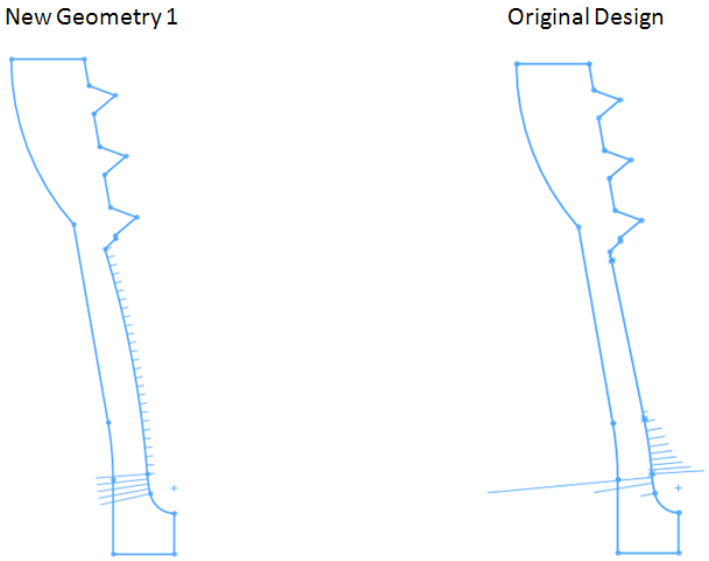

Figure E. 1 Curvature comb comparison New Geom. 1 – Original Design

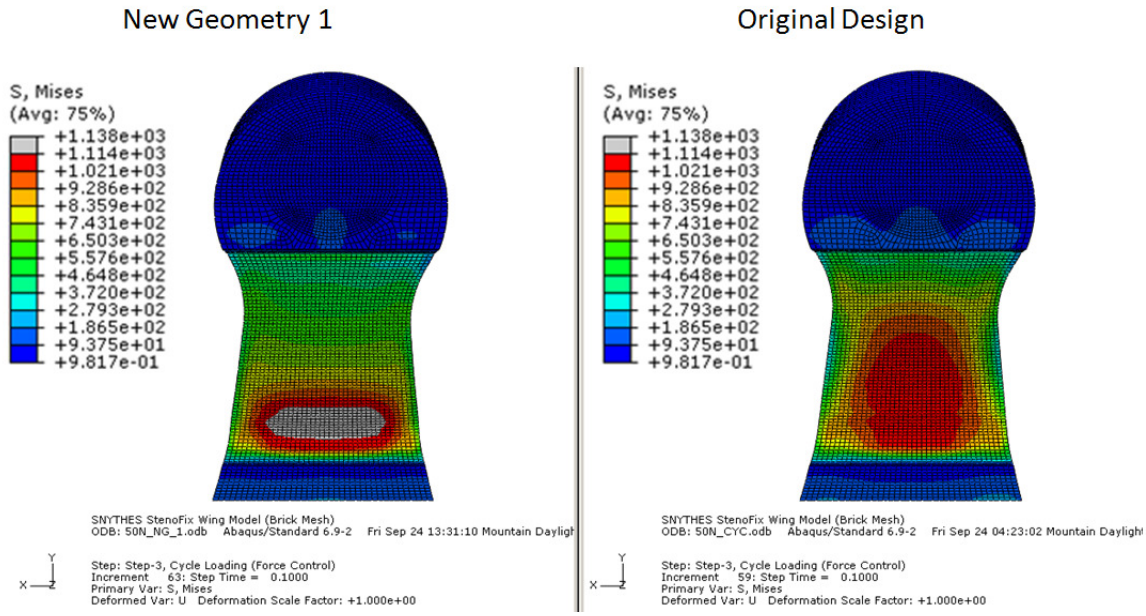

Figure E. 2 Back view stress field comparison New Geom. 1 – Original Design

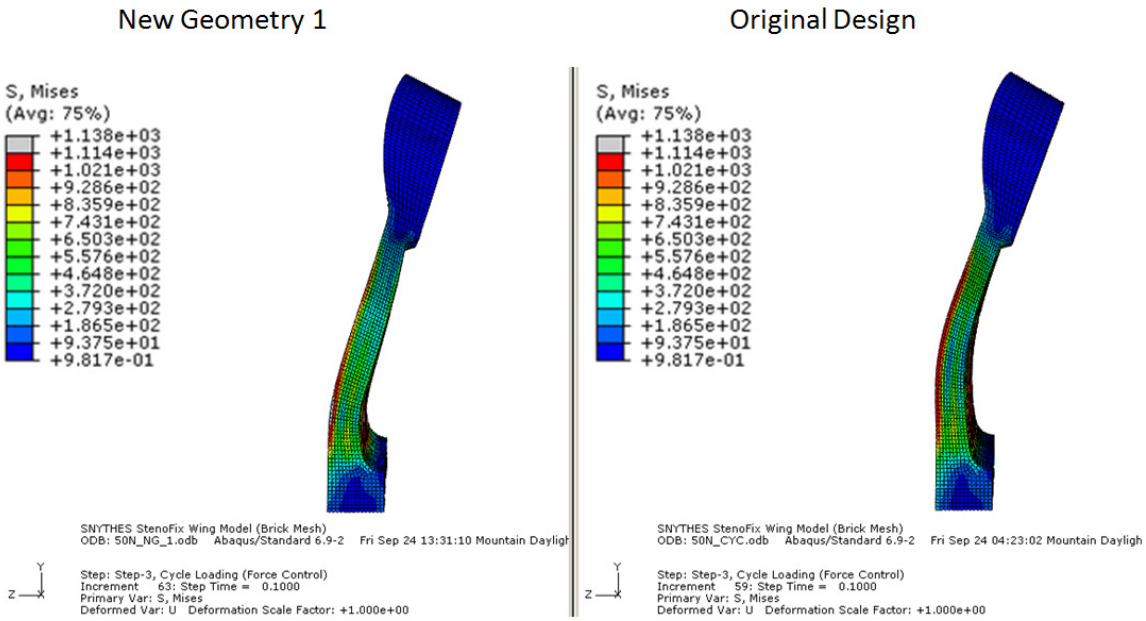

Figure E. 3 Right view stress field comparison New Geom. 1 – Original Design

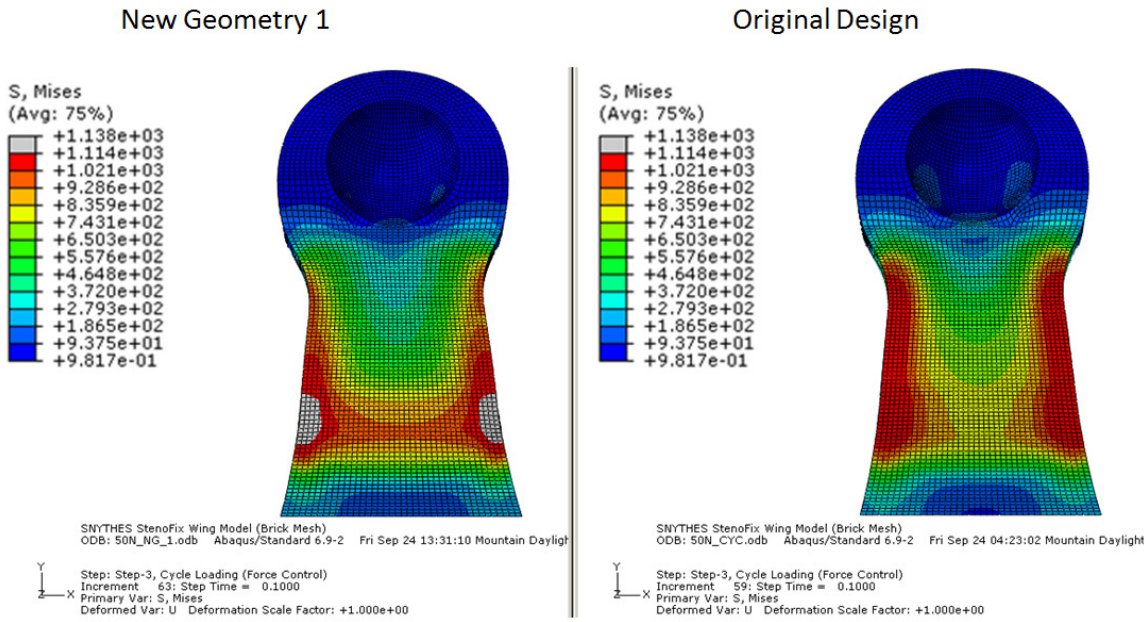

Figure E. 4 Front view stress field comparison New Geom. 1 – Original Design

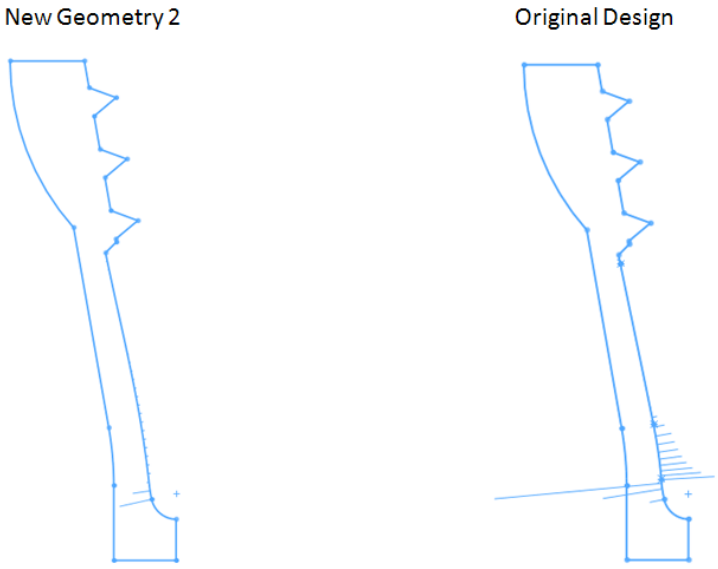

Figure E. 5 Curvature comb comparison New Geom. 2 – Original Design

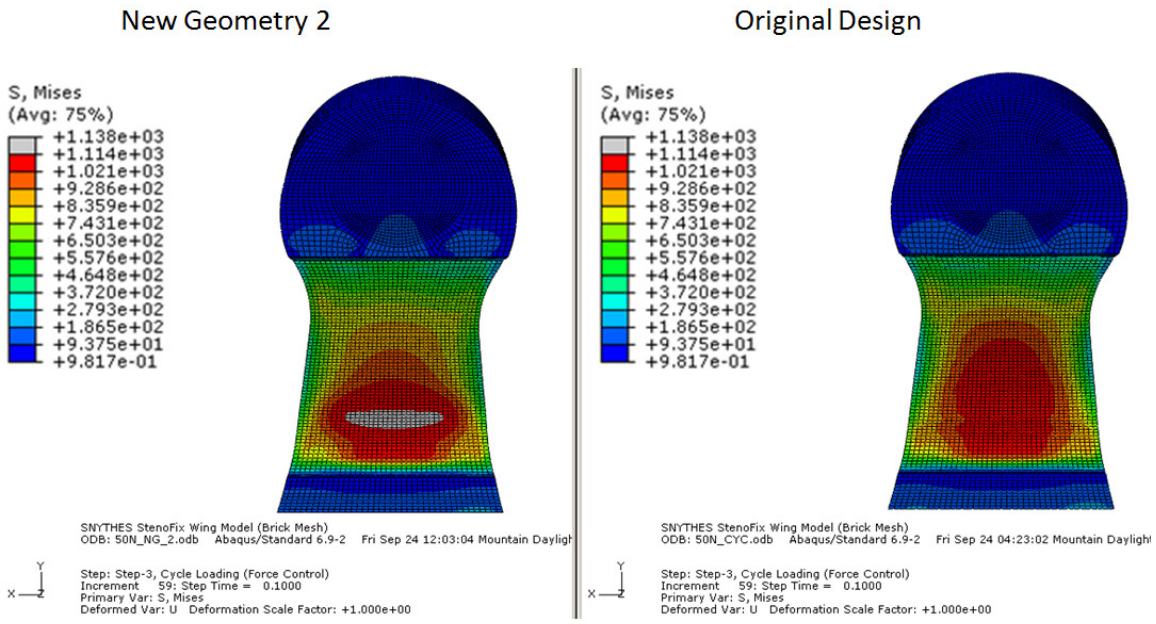

Figure E. 6 Back view stress field comparison New Geom. 2 – Original Design

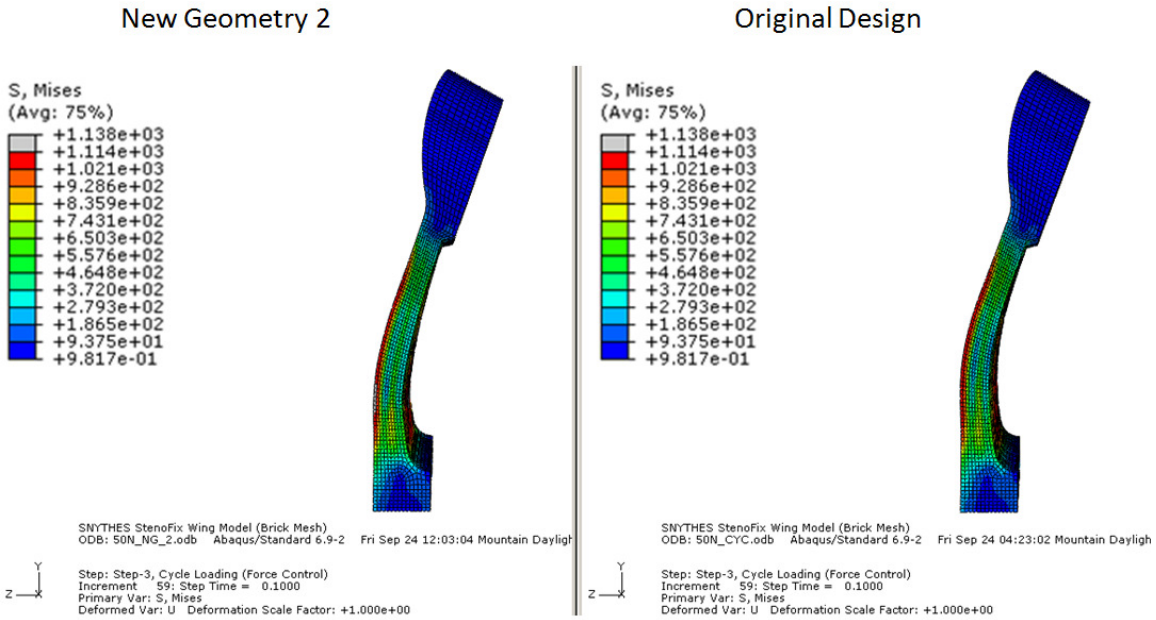

Figure E. 7 Right view stress field comparison New Geom. 2 – Original Design

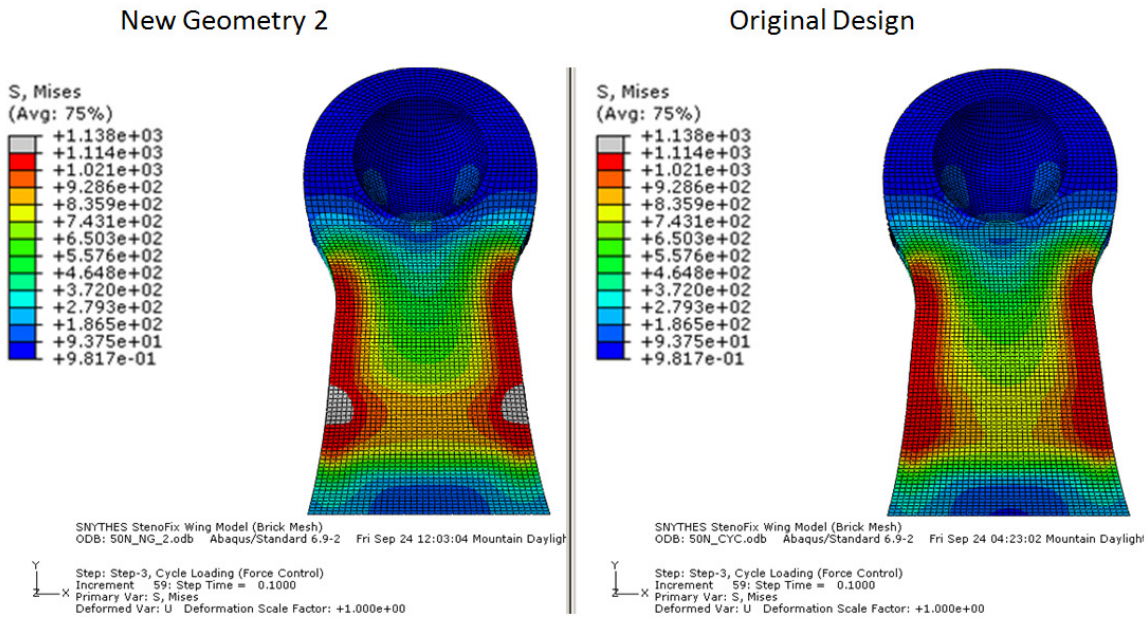

Figure E. 8 Front view stress field comparison New Geom. 2 – Original Design

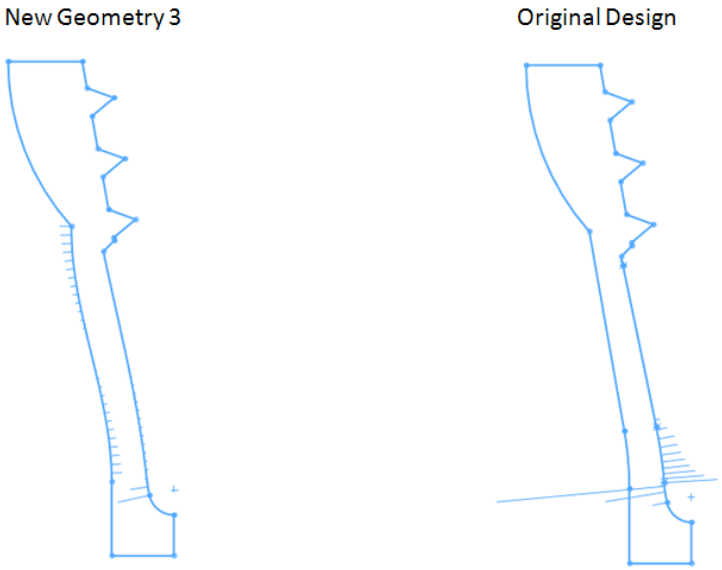

Figure E. 9 Curvature comb comparison New Geom. 3 – Original Design

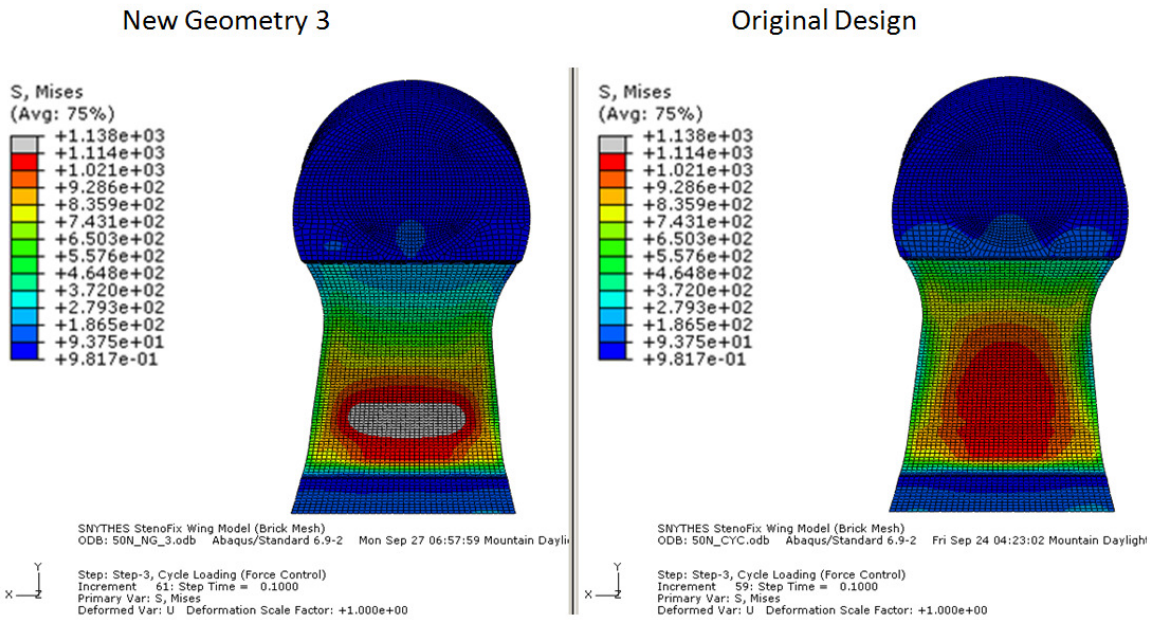

Figure E. 10 Back view stress field comparison New Geom. 3 – Original Design

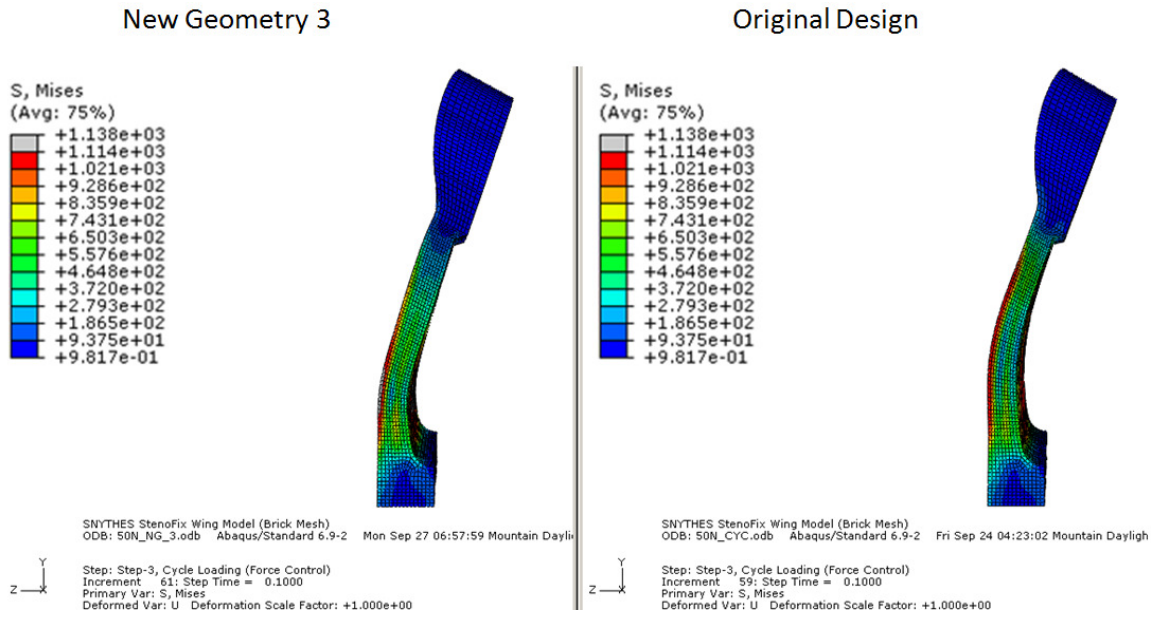

Figure E. 11 Right view stress field comparison New Geom. 3 – Original Design

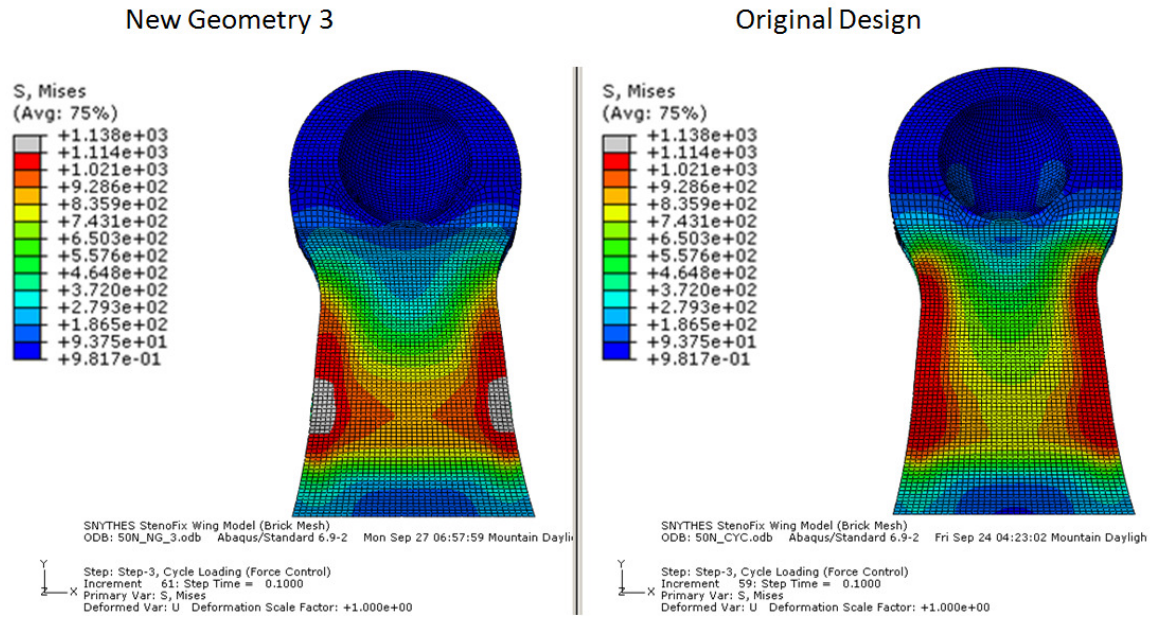

Figure E. 12 Front view stress field comparison New Geom. 3 – Original Design

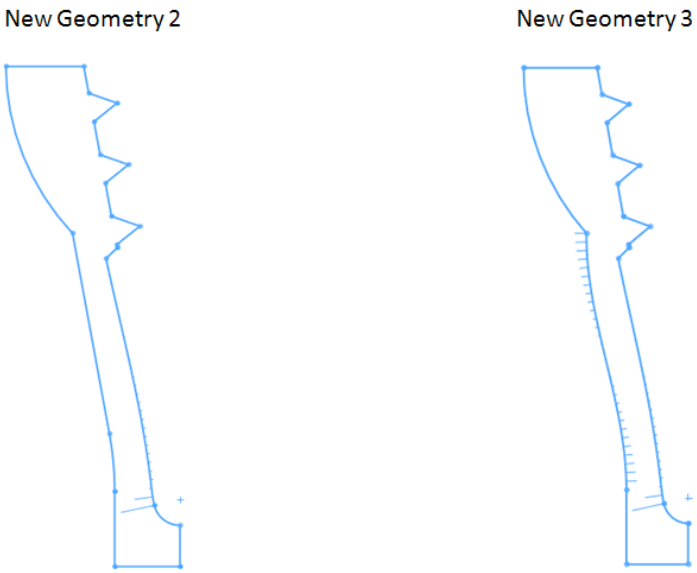

Figure E. 13 Curvature comb comparison New Geom. 2 – New Geom.3

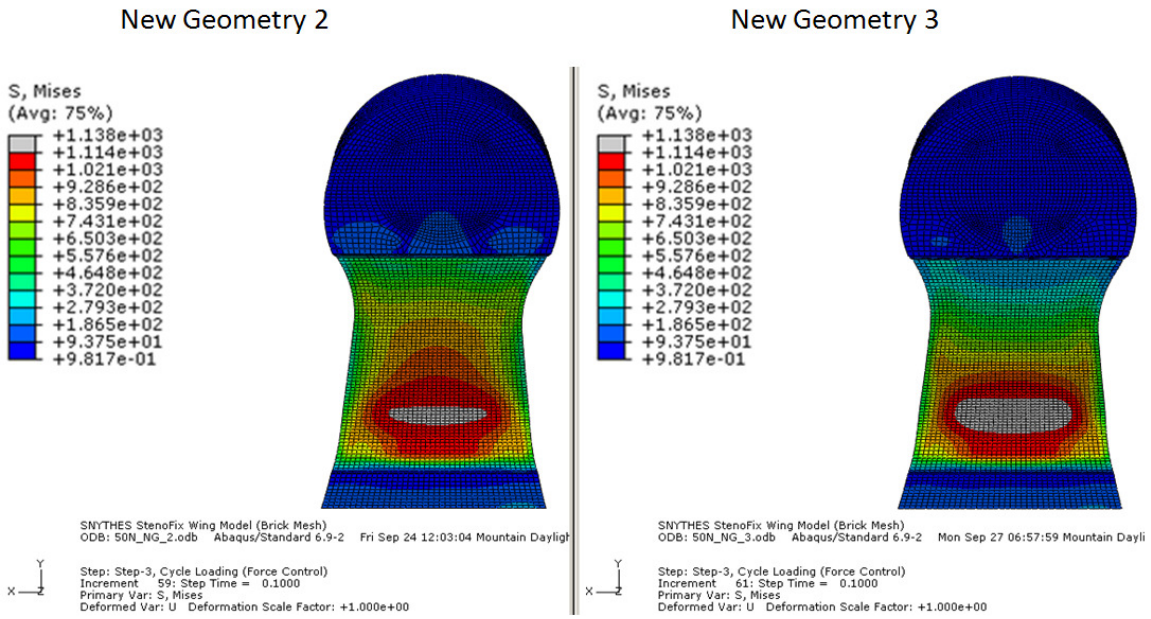

Figure E. 14 Back view stress field comparison New Geom. 2 – New Geom. 3

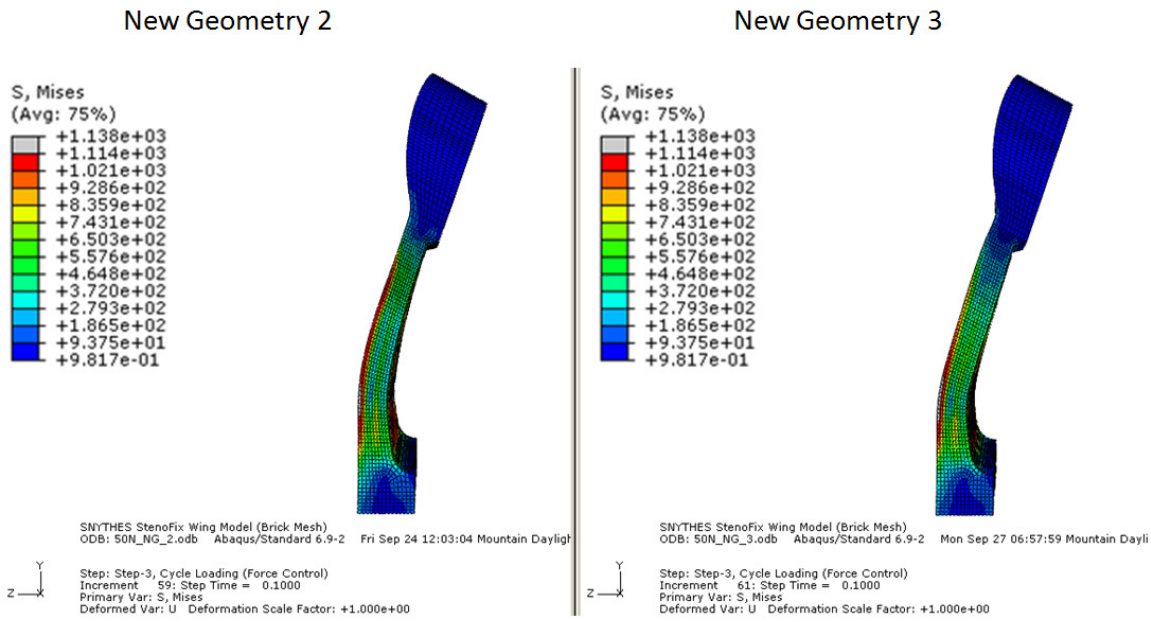

Figure E. 15 Right view stress field comparison New Geom. 2 – New Geom. 3

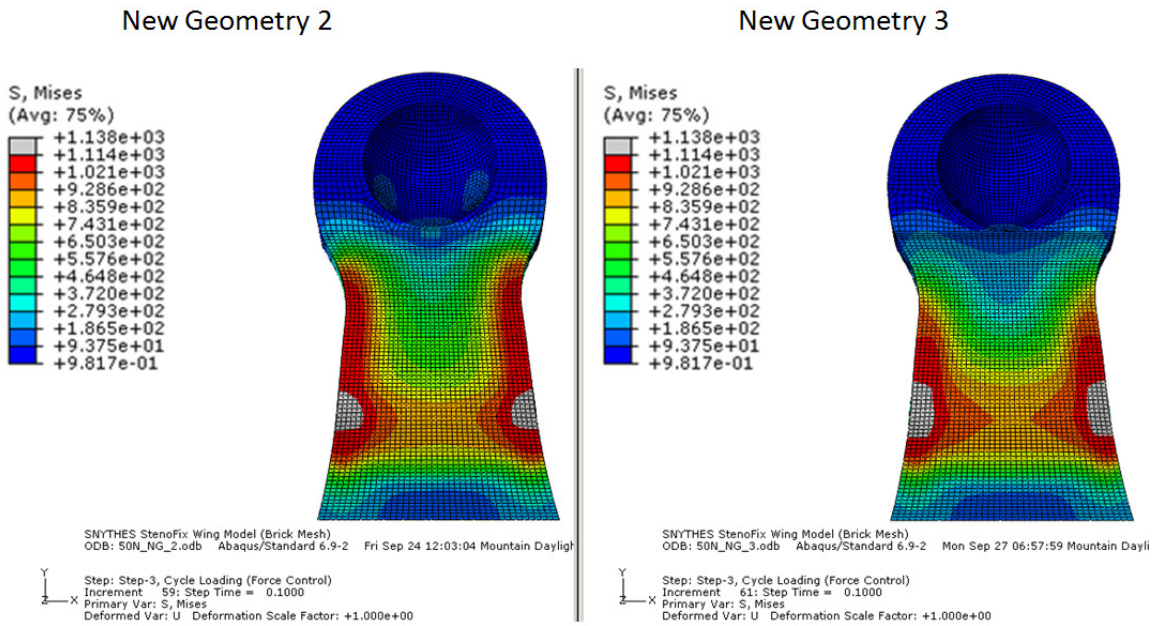

Figure E. 16 Front view stress field comparison New Geom. 2 – New Geom. 3